



5-2006

Spectroscopic Investigations in Chiral Crystalline and Solution Phases

Andrew Thomas Fischer
University of Tennessee - Knoxville

Recommended Citation

Fischer, Andrew Thomas, "Spectroscopic Investigations in Chiral Crystalline and Solution Phases. " PhD diss., University of Tennessee, 2006.
https://trace.tennessee.edu/utk_graddiss/1664

This Dissertation is brought to you for free and open access by the Graduate School at Trace: Tennessee Research and Creative Exchange. It has been accepted for inclusion in Doctoral Dissertations by an authorized administrator of Trace: Tennessee Research and Creative Exchange. For more information, please contact trace@utk.edu.

To the Graduate Council:

I am submitting herewith a dissertation written by Andrew Thomas Fischer entitled "Spectroscopic Investigations in Chiral Crystalline and Solution Phases." I have examined the final electronic copy of this dissertation for form and content and recommend that it be accepted in partial fulfillment of the requirements for the degree of Doctor of Philosophy, with a major in Chemistry.

Robert N. Compton, Major Professor

We have read this dissertation and recommend its acceptance:

Richard Pagni, George K. Schweitzer, Joseph Macek, Robert J. Hinde

Accepted for the Council:

Dixie L. Thompson

Vice Provost and Dean of the Graduate School

(Original signatures are on file with official student records.)

To the Graduate Council:

I am submitting herewith a dissertation written by Andrew Thomas Fischer entitled “Spectroscopic Investigations in Chiral Crystalline and Solution Phases.” I have examined the final electronic copy of this dissertation for form and content and recommend that it be accepted in partial fulfillment of the requirements for the degree of Doctor of Philosophy, with a major in Chemistry.

Robert N. Compton
Major Professor

We have read this dissertation and recommend its acceptance:

Richard Pagni

George K. Schweitzer

Joseph Macek

Robert J. Hinde

Accepted for the Council:

Anne Mayhew
Vice Chancellor and Dean of
Graduate Studies

(Original signatures are on file with official student records)

Spectroscopic Investigations in Chiral Crystalline and Solution Phases

A Dissertation
Presented for the
Doctor of Philosophy
Degree
The University of Tennessee, Knoxville

Andrew Thomas Fischer

May 2006

Dedication

This dissertation is dedicated to my parents, Steven K. Fischer and Kathleen N. Fischer, for instilling the value of education in me at a young age. I would not have made anywhere near this far without their guidance at a young age. I also want to dedicate this to my wife, Rebecca S. Fischer, for her support and patience through the years of graduate school. Too many times have I been lost in thought about experiments, and each time she was been patient with me. Last, but not least, this dissertation is dedicated to all of the graduate students who have helped me: Nathan Hammer, Rodney Sullivan, Wes Robertson, Jeff Steill, Watheq al-Basheer, and many others. Thank you for your help through all of this.

Acknowledgements

“Unless human reasoning is valid, no science can be true.” --C.S. Lewis, Miracles

I want to first acknowledge Jesus Christ for giving me the strength and helping me to make it this far in school. He has saved my life, and I hope and pray that everyday I am able to give my life up for service to others. Anybody who really knows me knows that it is not me that has made it here. I acknowledge that with this degree comes a responsibility.

I want to thank Dr. Robert Compton for taking me into his group many years ago; a graduate student is an investment, and I thank him for investing in me. He has helped me become a critical thinker where there was none to begin with, and he has helped me see the vast expanse of science. I want to also thank him for the many critical conversations regarding my work; they have only strengthened me as a scientist. If my scientific career is only a fraction of what he has produced, I will have made many scientific contributions.

I want to thank Dr. Richard Pagni for working with me also. Dr. Pagni has provided many insightful ideas, and he has listened to many of my own and persevered through much of my work. Likewise, Dr. Pagni has read and reread much of my work. His patience and willingness to help teach me have also brought me to where I am.

Dr. Schweitzer has been a teacher of mine in more than a few classes, and he too has shown me the value in thinking critically. Dr. Schweitzer has always demanded excellence from me (though rarely he got it I am sure), and my standards have been raised.

I would also like to thank Dr. Hinde. The main reason that I am now in physical chemistry is the undergraduate quantum class from Dr. Hinde. His teaching style has been the most conducive for me to learn, and he has always been able to answer my questions. I want to thank him for teaching me, and I would like to acknowledge him as

the professor that first broke through and got me to start breaking problems down to their simplest bases.

Abstract

Chirality is an interesting phenomenon that is not completely understood, and the present work broadens the present body of knowledge using various methods. Crystallization experiments of glycine have confirmed the previously reported phenomenon of nonphotochemical laser induced nucleation (NPLIN), and experiments utilizing a geometry with focused lasers may also display NPLIN, though the results indicate that new factors such as pH of the irradiated solution may affect the crystallizing process. Sodium bromate, NaBrO_3 , may also crystallize via NPLIN, though the results are not as conclusive as the glycine experiments. For both glycine and sodium bromate, sound waves produced micron sized crystals of high quality.

The optical rotatory dispersion (ORD) curve of sodium chlorate and sodium bromate was recorded, and good agreement was found with previous literature. Laser light with a sufficient intensity gave rise to non-linear effects (NL-ORD) in the optical rotation. The NL-ORD was composed of a main contribution from ν_1 , but multi-photon contributions, $n\nu_1$, affected the optical rotation.

The compressibility of racemic and enantiomerically pure α -methylbenzylamine was measured using a novel apparatus, and low frequency intermolecular vibrations measured via Raman spectroscopy gave good agreement with the magnitude of the compressibility. The compressibility of the enantiomerically pure α -methylbenzylamine was slightly higher than the racemic solution.

The ORD of (*S*)-(α)-methylbenzylamine was recorded in a series of 39 solvents with widely ranging solvent properties. Calculations of the optical rotation via Gaussian03 were insufficient in describing the solvent effect upon the optical rotation. A good correlation of the optical rotation and the Kamlet-Taft parameters (α , β , π^*) was established, and good agreement was found between the predicted model and the experimental results.

Spectroscopic characterization of α -methylbenzylamine over the entire mole fraction concentration range in five distinct solvents (cyclohexane, toluene, nitrobenzene, DMSO, and methanol) via FTIR and NMR helped illuminate mitigating factors affecting the optical rotation. The nitrogen site was the only contributor that dominantly affected the optical rotation in the selected solvents.

Table of Contents

Chapter	Page
I. Chirality and Chiral Discrimination	1
II. Fundamentals of Nucleation and Crystallization	8
Introduction	8
Primary Nucleation: Thermodynamics and Kinetics	8
Heterogeneous Nucleation	12
Secondary Nucleation	14
III. Nonphotochemical Laser Induced Nucleation of Glycine	17
Introduction	17
Experimental	22
Results and Discussion	25
Conclusion	32
IV. Nonphotochemical Laser Induced Nucleation of Sodium Bromate	34
Introduction	34
Experimental	38
Results and Discussion	41
Conclusion	52
V. Linear and Non-linear Optical Rotation in Sodium Chlorate and Sodium Bromate	53
Introduction	53
Experimental	63
Results and Discussion	65
Conclusion	74

VI. Speed of Sound in Racemic and Optically Pure α -Methylbenzylamine	76
Introduction	76
Experimental	83
Results and Discussion	85
Conclusion	92
VII. Solvent Effects on the Optical Rotation of (<i>S</i>)- α -Methylbenzylamine	93
Introduction	93
Experimental	98
Results and Discussion	99
Conclusion	115
VIII. Mole Fraction Studies of α -Methylbenzylamine using FTIR and NMR with Applications to Optical Rotations Results	116
Introduction	116
Experimental	122
Results and Discussion	123
Conclusions	149
IX. Conclusions	150
References	153
Vita	163

List of Tables

Table	Page
Chapter III.	
1. Results for the compilation of glycine crystallization experiments.	27
Chapter IV.	
1. Results for linearly polarized light irradiated sodium bromate.	42
2. Results for the right circularly polarized light irradiated sodium bromate.	45
3. Results for the sound generated sodium bromate crystals.	47
4. Results for the control and Petri dish experiments for sodium bromate.	47
Chapter V.	
1. Results for linear optical rotatory dispersion curve for sodium chlorate and sodium bromate crystals.	66
2. (a) Results for the power dependent optical rotations of NaClO_3 at 532 nm. Units of results are degrees/mm. (b) Results for power dependent optical rotations of sodium bromate at 532 nm.	68
3. (a) Results for power dependent optical rotations of NaClO_3 at 355 nm. Units of results are degrees/mm. (b) Results for power dependent optical rotations for NaBrO_3 at 355 nm.	69
Chapter VI.	
1. Results for the individual speed of sound experiments; values are tabulated for both the racemic and (<i>S</i>)-(-)- α -methylbenzylamine.	86

Chapter VII.

1. List of excluded solvents during statistical analysis for each experimental wavelength and calculated values. 100
2. Results of calculation of specific rotation at 589 nm with PCM solvation in acetonitrile with various methods and basis sets. 101
3. Tabulated infinite dilution optical rotations for all wavelengths. 102
4. Results for calculated specific rotation at 589 nm (B3LYP aug-cc-pVDZ PCM calculation) for all solvents. 104
5. Results for coefficients for each experimental wavelength and calculated rotation at 589 nm. 111
6. Experimental intrinsic and calculated specific rotations at 589 nm for solvents with $\epsilon < 3$ and dipole moment, μ (D), < 1 . 114

Chapter VIII.

1. Summary of results for asymmetric NH stretch, $\delta(\text{NH}_2)$, and optical rotation at 436 nm for all solvents. 124
2. Results for FTIR experiments and calculations of MBA. 125
3. Tabulated results for Mulliken charges in solvated systems. 134
4. Results of the infinite dilution analysis for FTIR and NMR experiments. 146
5. Results of multiple variable linear regression analysis for infinite dilution values for FTIR and NMR experiments. 147

List of Figures

Figure	Page
Chapter I.	
1. Example of chiral carbon center.	2
2. Example of a helical arrangement of atoms.	3
3. Depiction of linearly polarized light.	5
4. Depiction of circularly polarized light.	6
5. Schematic of apparatus for measuring optical rotation.	7
Chapter II.	
1. Crystallization angle relating contact of crystalline phase, impurity phase, and solutions phase.	13
Chapter III.	
1. Molecular structure of glycine.	18
2. Fractional composition of glycine as a function of pH.	19
3. Experimental schematic for repeating experiments by Garetz et al.	23
4. Schematic diagram for apparatus to focus polarized light into solution.	24
5. Experimental geometry for the sound wave nucleation experiments.	26
6. pH of glycine solutions (concentrations vary) irradiated with focused (or unfocused) 700 mW 1064 nm light as a function of time.	29
7. Results from irradiating glycine solutions (varying solution sizes) with 700 mW 1064 radiation.	30
Chapter IV.	
1. Experimental setup for the irradiation of the sodium bromate solutions.	40

2. Comparison of the results for the linearly polarized light experiments for sodium bromate. 44
3. Comparison of the results for the right circularly polarized light experiments for sodium bromate. 46
4. Comparison of the results for the sound and Petri dish experiments for sodium bromate. 48

Chapter V.

1. Schematic diagram for optical rotation measurements. 64
2. Graphical depiction of experimental results for one-photon ORD of sodium chlorate and sodium bromate and predicted (Eq. 54 and 55) values. 67
3. Graphical interpretation for the non-linear optical rotation. 71
4. Contribution of ρ_{266} from the data from table 2(a) is plotted versus the logarithm of the intensity for data from sodium chlorate at 532 nm. 73

Chapter VI.

1. Flat view of (*S*)- α -methylbenzylamine. 79
2. Proposed structure for the (*R*)-(+)- α -phenylethylammonium (*S*)-(+)-mandelate ion pair as produced by Zingg et al.⁹⁸. 81
3. Proposed structure for the (*R*)-(+)- α -phenylethylammonium (*R*)-(+)-mandelate ion pair as produced by Zingg et al.⁹⁸. 81
4. Experimental apparatus used to determine the speed of sound in liquids. 84
5. Typical spectra of the speed of sound profile in MBA. 87
6. Typical spectrum of nearly overlapping detection He:Ne and sound generating Nd:YAG beams. 88

7. Room temperature low frequency Raman spectrum of (<i>S</i>)- and racemic MBA.	89
--	----

Chapter VII.

1. Structure of (<i>R</i>)-(+)- α -methylbenzylamine and (<i>S</i>)-(-)- α -methylbenzylamine respectively.	94
2. Plot of intrinsic rotation at 589 nm vs. Onsager function.	106
3. Plot of intrinsic rotation at 589 nm vs. dipole moment.	107
4. Plot of intrinsic rotation at 589 nm vs. $E_T(30)$ values.	108
5. Plot of intrinsic rotation at 589 nm versus polarizability calculated from Clausius-Mossotti equation.	109

Chapter VIII.

1. Illustration of electron movement from methyl groups of DMSO to stabilize hydrogen bond with methanol.	119
2. Results from LaPlanche et al. ¹⁷⁴ for NH proton of <i>N</i> -isopropylacetamide in inert solvents.	121
3. Results for the ^1H NMR experiments for MBA and cyclohexane.	126
4. Results for the ^1H NMR experiments for MBA and toluene.	127
5. Results for the ^1H NMR experiments for MBA and nitrobenzene.	128
6. Results for the ^1H NMR experiments for MBA and methanol.	129
7. Results for the ^1H NMR experiments for MBA and DMSO.	130
8. Observed optical rotation at 436 nm with respect to mole fraction MBA for various solvents.	131
9. Specific rotation at 436 nm for MBA with respect to mole fraction for various solvents.	132
10. Scheme of the proposed electrostatic interaction between MBA and DMSO.	139

11. Optimized structure for MBA^+ in methanol.	141
12. Optimized structure for MBA dimer in methanol.	142
13. Optimized MBA and methanol in methanol.	144

Chapter I.

Chirality and Chiral Discrimination

Two objects are said to be chiral if their mirror images are non-superimposable upon one another. Chirality is most often seen in molecules with a specific chiral center where different substituents are bonded, most notably a carbon atom bonded to four different substituents; an example is shown in Figure 1. Chirality is not restricted to such examples, however. Chirality can also be the result of the spatial arrangement of an entire molecule or collection of molecules in a system, with examples being the twisting of helices or arrangement of molecules in a crystal lattice, with an example shown in Figure 2.

There are two distinct types of interactions in chiral species: enantiomeric and diastereomeric. Enantiomeric interactions occur when molecules (or systems) with the same chirality interact with one another while diastereomeric interactions occur when molecules with opposite handedness interact. Chiral discrimination is defined as an interaction energy difference for like handed and differing handed systems and differs in magnitude depending upon the phase of the interaction. Estimations of the enantiomeric interactions in the solid phase (kJ/mol) increase greatly when compared to the solution phase (J/mol)¹.

Recognizing and investigating the discrimination between diastereomers, (+)-A (+)-B and (-)-A (+)-B, has generally been accepted as considerably easier than investigating like and unlike enantiomeric interactions. The most commonly accepted model for diastereomeric discrimination² is the 'lock and key' model for enzyme-substrate interaction proposed by Fischer³. The 'lock and key' model postulates that a more compact fit is sterically allowed between the two chiral species in one of the diastereomeric interaction than the opposing diastereomeric interactions. Beyond energetic differences between configurations of enantiomers, chiral molecules have inherent chiroptical properties. Chiral molecules possess the ability to rotate plane polarized light (optical rotation) and preferentially absorb either left or right handed

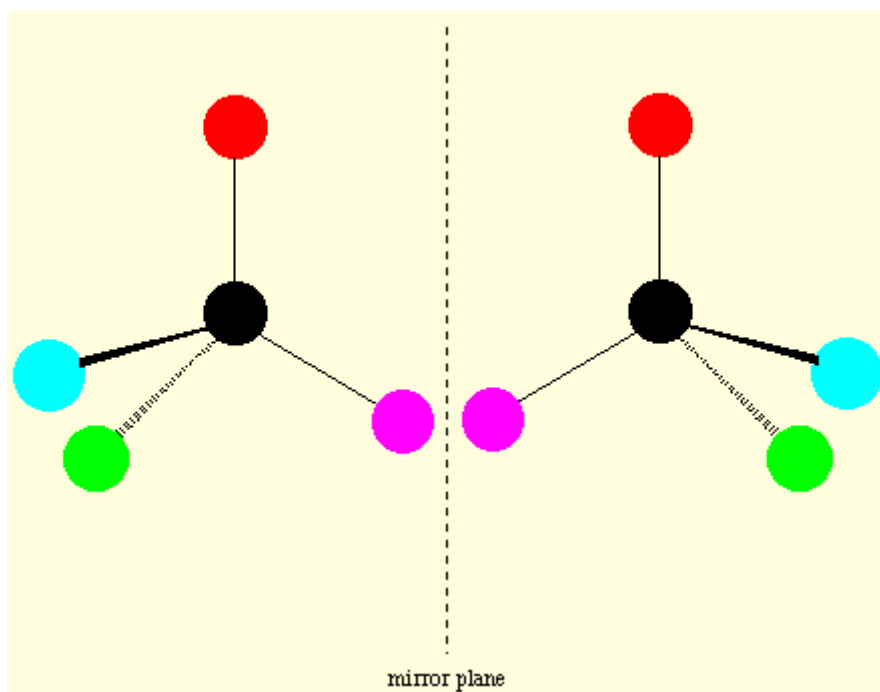


Figure 1. Example of chiral carbon center. Four different substituents are bonded to the chiral carbon, and as seen, the mirror images are not superimposable.

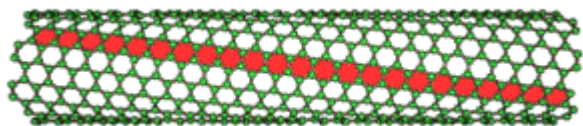


Figure 2. Example of a helical arrangement of atoms. Shown above is a chiral nanotube that possesses a right handed helical arrangement of carbon atoms.

circularly polarized light (circular dichroism). The theory underlying optical rotation will be examined in later chapters.

Similar to atomic and molecular chirality, photons are chiral. Figures 3 and 4 show linearly and right circularly polarized light, respectively (left circularly polarized light would be the opposite helical motion). A fixed orientation of the electric vector of the electromagnetic field in space is the necessary condition for linearly polarized light; as seen in Figure 3, the orientation of the electric vector can give rise to either horizontal or vertical polarization. Circular polarization arises when the orientation of the electric field is not restricted to a plane, and varies with time. Figure 4 shows a depiction of right circularly polarized light. The experimental geometry for measuring the optical rotation of a sample is seen in Figure 5; briefly, incident light is plane polarized before passing through a sample. If the sample is enantiomerically pure (or enantiomerically enriched), the plane of polarization will be rotated by an angle, θ , after a distance l . The technique of optical rotatory dispersion (wavelength dependence of optical rotation) will be explored in more detail throughout the present research.

Within this dissertation, both chiral crystalline and liquid chiral phases will be studied. Experiments will range from using chiral photons (circularly polarized light) to induce chirality in crystallizing solutions to probing the packing of molecules in solution phase to non-linear chiroptical effects. Through these experiments, a more comprehensive view of chirality will hopefully be attained.

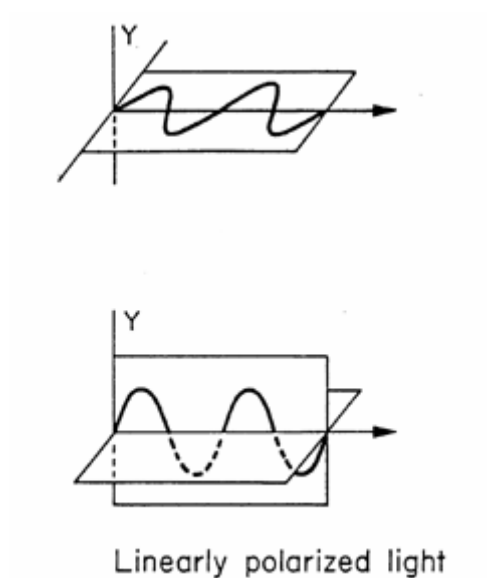


Figure 3. Depiction of linearly polarized light. The polarization can be either horizontal or vertical. Linearly polarized light can also be thought of as equal magnitudes of in-phase left and right circularly polarized light. The oscillation of the electric field is highlighted by the line in one plane.

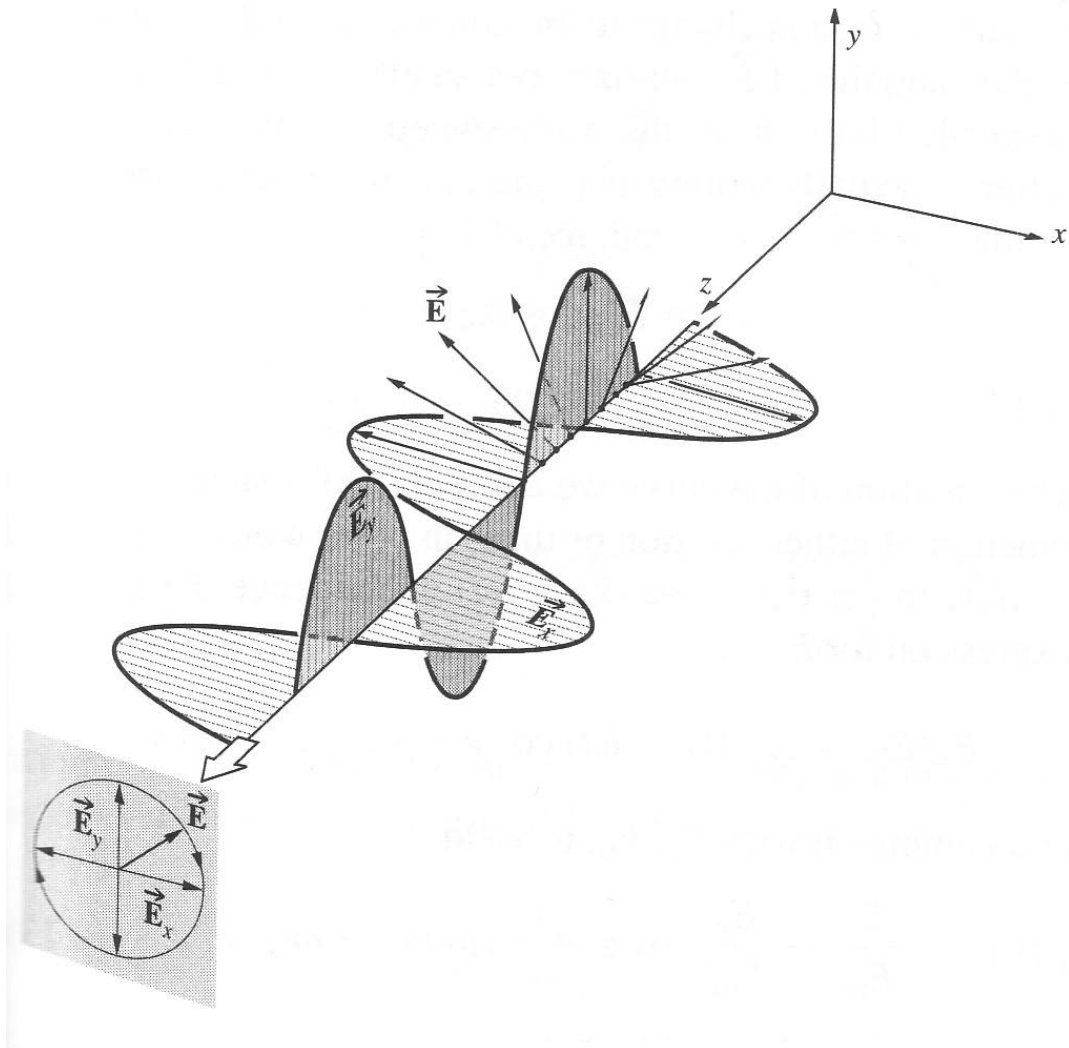


Figure 4. Depiction of circularly polarized light. The electric vector of the EM field describes a helical motion in space. The direction of propagation remains constant, but the direction of the sinusoidal electric and magnetic fields are seen to rotate through space.

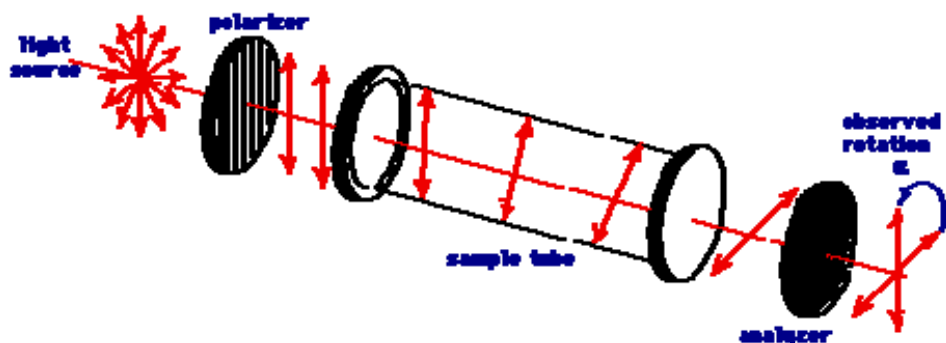


Figure 5. Schematic of apparatus for measuring optical rotation. Incident light is initially polarized before passing through sample. After passing through the sample, the plane of polarization has been rotated by an angle, θ .

Chapter II.

Fundamentals of Nucleation and Crystallization

Introduction

Crystallization is the result of the ordered growth of a species into an extended structure. In solution, a high concentration of solute by itself is insufficient to cause crystallization. In order for a crystal to grow, a cluster must form and continue to grow in an ordered fashion to result in a crystal. Early studies^{4,5} showed that mechanical perturbations, such as agitation, mechanical shock, and pressure gradients, can cause supersaturated solutions (where the concentration in solution is greater than the saturation point) to crystallize. Khaamskii⁶ has reviewed crystallization due to external sources, such as electromagnetic effects. Crystallization is normally thought to proceed via two possible mechanisms: primary or secondary nucleation. In the case of primary nucleation, nucleation phenomena are divided into either spontaneous (homogenous) or induced (heterogeneous) nucleation.

Primary Nucleation: Thermodynamics and Kinetics

The basic principle underlying crystallization is a thermodynamic imbalance between the liquid phase and a solid, cluster-like, phase. The thermodynamic quantity that drives the crystallization process is the chemical potential, μ , for each phase. In all phase transitions, the thermodynamic push comes from the difference in μ between the two phases, i.e.

$$\Delta\mu = \mu_1 - \mu_2 \quad \text{Eq. 1}$$

where the chemical potential is defined as

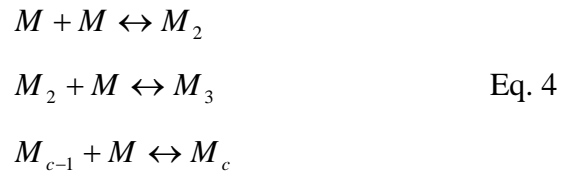
$$\mu = \mu_0 + RT \ln(S) \quad \text{Eq. 2}$$

where μ_0 is the standard potential, R is the gas constant, and T is the temperature. S is the supersaturation parameter defined as

$$S = \frac{c}{c_0} \quad \text{Eq. 3}$$

where c is the concentration of the solution and c_0 is the saturation level of the solution. The supersaturation of a solution can be more accurately described by the ratio of the activities of the solution, but the ratio of the concentrations is often used as a valid approximation. The need for the use of energy, i.e. chemical potential, stems from the need to form and separate the interface, i.e. the new crystal, from the solution^{7,8}. As will be shown later, a more descriptive theory for crystallization requires assumptions based upon the mechanism and shape formation of the crystal.

If the homogeneous formation of a crystal were the result of multiple bimolecular collisions, the following scheme would adequately describe the successive addition of molecules to the cluster:



where for each addition, it is as likely to proceed in the reverse direction, i.e. losing the recently added molecule, as it is to undergo another successful addition. In the above scheme, M_c represents the critically sized cluster, which is defined as the cluster that, upon further additions, would proceed to crystal nucleation. Smaller nuclei can easily form by the above scheme, but as seen through the possibility to proceed backwards and lose a molecule from the cluster, many pre-critical nuclei may form before the successful formation of the critically sized cluster due to instability of the pre-critical clusters.

The exact shape of the cluster is unknown due to the small size of the cluster. As will be mentioned later, several theories predict that the cluster exhibits the same morphology of the crystal it will grow into, and other theories predict that the cluster will rearrange into the morphology that will minimize the energy of the small cluster in

solution. Neither theory has been proven. Hoare and McInnes⁹ have reviewed previous work on the structure and morphology of small molecular clusters.

The classical theory of nucleation stems from the works of many scientists^{10, 11, 12} on the condensation of vapor to a liquid. This formalism was adopted to describe the transition from an aqueous cluster to crystals. If one assumes that the cluster is growing into a sphere with radius 'r', the excess free energy, ΔG , between the solute particle and the solute in solution (which would then give the driving force towards becoming a solute particle) is equivalent to the sum of the free energy change of the surface, ΔG_s , and the free energy change of the volume of the cluster, ΔG_v . The excess free energy is given by

$$\begin{aligned}\Delta G &= \Delta G_s + \Delta G_v \\ &= 4\pi r^2 \gamma + \frac{4}{3}\pi r^3 \Delta G_v\end{aligned}\quad \text{Eq. 5}$$

where ΔG_v is the free energy change per unit volume and γ is the interfacial tension. The two terms on the right side of Eq. 5 are of opposite sign and depend differently upon r, therefore the excess free energy of the crystallization goes through a maximum as a function of r. The maximum value for the excess free energy, in terms of the radius of the critically sized nucleus, r_c , is given by

$$\Delta G_{crit} = \frac{16\pi\gamma^3}{3(\Delta G_v)^2} = \frac{4\gamma\pi r_c^2}{3}\quad \text{Eq. 6}$$

Any changes in the size of the nucleus should result in an overall lowering of the free energy of the cluster. Therefore, any cluster that has a radius smaller than r_c will dissociate back into the solution, and any cluster that has a radius larger than r_c will continue to grow into a crystal. The amount of energy in a liquid at constant temperature and pressure is constant, but the amount of energy present in a particular finite volume of the liquid is not constant. A distribution of molecular velocities within the solution translates into a distribution of energies around an average value. Fluctuations will occur in the vicinity of this average value, and in regions where the fluctuation is high enough to allow for the formation of a critically sized cluster, nucleation will occur.

The rates of thermally activated processes are normally described using the Arrhenius equation:

$$J = A \times \exp\left(\frac{\Delta G}{k_B T}\right) \quad \text{Eq. 7}$$

where A is a pre-exponential factor, ΔG is the change in free energy for the process, k_B is Boltzmann's constant, and T is the absolute temperature. The Gibbs-Thomson relationship states

$$\ln S = \frac{2\gamma v}{k_B T r} \quad \text{Eq. 8}$$

where S is the previously stated supersaturation, v is the molecular volume, and r is the radius of the cluster. Upon combining equations 5 and 6 and substituting into the Arrhenius equation, the rate of nucleation can be given as

$$J = A \times \exp\left(\frac{-16\pi\gamma^3 v^2}{3k_B^3 T^3 (\ln S)^2}\right) \quad \text{Eq. 9}$$

Equation 9 is the expression commonly used to describe the rate of primary homogenous nucleation. From this equation, one can see that three main variables describe the rate of nucleation: the temperature, the degree of supersaturation, and the interfacial tension. The assumption of a spherical nuclei was used in all of the above considerations. If that assumption were invalid, a different geometrical factor would have to be used.

Nielson¹³ developed an empirical approach to describe the nucleation process using an induction time, t_{ind} . The following relationship is derived

$$t_{ind} = k \times c^{1-p} \quad \text{Eq. 10}$$

where k is a constant, c is the concentration of the supersaturated solution, and p is the number of molecules making up a critical nucleus. This particular equation represents a simplified expression for the complex process of crystallization. The secondary nucleation empirical relationship along with classical nucleation theories provide a mechanism of clustering of molecules, but none of the proposed theories agree upon the relationship of the supersaturation with the size of the critical nucleus. Experimental evidence for the size dependence of the critically sized nucleus is necessary to further refine the nucleation theories. Several reviews of nucleation mechanisms have been published^{13, 14, 15} with the recent review by Kashchiev¹⁶ relating thermodynamics and kinetics to homogenous and heterogenous nucleation.

Heterogeneous Nucleation

Heterogeneous nucleation is considered to be nucleation induced by non-crystalline matter. Impurities can affect the crystallization process by either promoting or inhibiting the formation of a crystal. In many experiments, spontaneous nucleation is found to be induced by trace amounts of impurities in solution. Generally, aqueous solutions contain many particles that are greater than 1 μm in size; great care can be taken to reduce the number density of the impurities, but total elimination of impurities is virtually impossible. Impurities can also be found frequently trapped within cavities or on sides of the vessels that hold the crystallizing solution thereby making completely spontaneous nucleation a less likely event.

In order for an impurity to promote crystallization, the free energy change for the formation of the critical nucleus, $\Delta G'_{crit}$, under heterogeneous conditions must be lower than the free energy change, ΔG_{crit} , for homogeneous conditions. The effect of an impurity on the free energy change can be expressed by

$$\Delta G'_{crit} = \phi \Delta G_{crit} \quad \text{Eq. 11}$$

where ϕ is a factor less than unity in the case that the impurity is a promoter. As indicated previously with reference to Equation 9, the interfacial tension, γ , is seen to contribute to the rate of formation for a crystal. Figure 1 shows a phase diagram relating the contact of the crystalline phase, the impurity phase, and the solution phase. The interfacial tensions are denoted by γ_{cl} (interface between crystalline and liquid phase), γ_{sl} (interface between impurity and liquid phase), and γ_{cs} (interface between crystalline and impurity). Combining these forces in a horizontal direction gives

$$\gamma_{sl} = \gamma_{cs} + \gamma_{cl} \cos \theta \quad \text{Eq. 12}$$

Three scenarios exist for equation 12; θ can either equal 0° , θ can vary between 0 and 180° , or θ can be 180° . For each of those scenarios, the respective free energies would be

$$\Delta G'_{crit} = 0 \quad \text{Eq. 13}$$

$$\Delta G'_{crit} < \Delta G_{crit} \quad \text{Eq. 14}$$

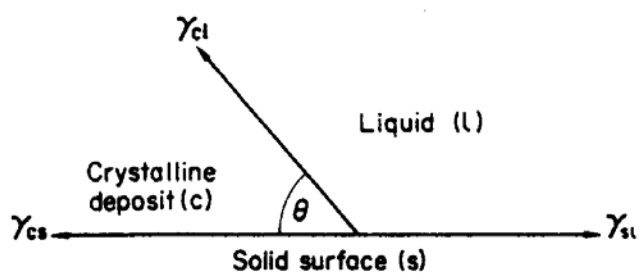


Figure 1. Crystallization angle relating contact of crystalline phase, impurity phase, and solutions phase. γ_{cl} , γ_{sl} , and γ_{cs} are crystalline-liquid phase, impurity-liquid phase, and crystalline-impurity interfacial tensions respectively. This figure is reprinted from Mullin¹⁷.

$$\Delta G'_{crit} = \Delta G_{crit} \quad \text{Eq. 15}$$

The scenario expressed in Eq. 13 corresponds to the impurity being a seed crystal of the material, and represents an example of secondary nucleation. For Equation 14, this corresponds to impurities that are able to promote the crystallization of the material. Equation 15 describes an example in which the material does not change the free energy required for nucleation.

Secondary Nucleation

A supersaturated solution will crystallize more quickly if crystals are already present in the solution. In this case, secondary nucleation represents the primary mode of formation of crystals due to the presence of previously formed crystals in solution. Strickland-Constable¹⁴ and Botsaris et al.¹⁸ have previously described various mechanisms in which secondary nucleation could occur. Constable-Strickland proposed four different mechanisms leading to secondary nucleation: initial breeding, needle breeding, polycrystalline breeding, and collisional breeding. Initial breeding is the formation of secondary nuclei as a result of dust that is swept off of the surface of the seed crystal when it is introduced to the system. Needle and polycrystalline breeding are similar in that each represents the detachment of part of the crystalline structure from the seed crystal (the detachment can occur through physical stress or strain to the system). Collisional breeding is the formation of the secondary nuclei through a process that involves the collision of multiple clusters that have formed as a result of the seed crystal.

Qian and Botsaris¹⁹ postulated a theory for the rate of secondary nucleation, which noted that the attraction between clusters and surfaces of the “mother crystal” would lead to higher nucleation rates. An empirical rate law for secondary nucleation in stirring experiments is of the formⁿ

$$R_s = k(c - c_0)^\alpha \quad \text{Eq. 16}$$

where k is a factor that depends upon the rate of stirring, c is the concentration, and c_0 is the concentration at saturation. The exponent α has been suggested to be greater than 1²⁰,²¹. This empirical rate law is similar in form to the empirical rate law for primary

nucleation. A more fundamental rate law model for secondary nucleation has not been proposed to date.

The principal investigations of secondary crystallization from chiral seeds have focused primarily on three objectives²². The first main objective is to identify the origins of secondary nuclei: are secondary nuclei fragments of a seed or a result of the concentration gradient surrounding the seed? A study by Denk and Botsaris²³ found that primarily, a crystal formed in the presence of a chiral seed crystal retained the chirality from the seed, though under specific conditions, the results could be reversed. Denk and Botsaris also concluded that secondary nuclei are generated through three mechanisms: growth and detachment of irregular surfaces, impurity concentration gradient at the crystal interface, and an ordering of water molecules near the surface of the seed (though this mechanism seems unlikely).

The second main objective regarding the generation of secondary nuclei is to understand whether there is a preference to crystallize into a specific enantiomer from a racemic solution in the presence of an enantiomeric seed crystal. Such results may be an indicator of the propagation of chirality through nature. An interesting result was found from investigations addressing this question. Yokoto and Toyokura²⁴ found that, when an L-crystal of S-carboxymethyl-D-cysteine (SCMC) was immersed in a solution of L-SCMC, pits developed on the crystal surface. Davey et al.²⁵ found similar results from a crystal of triazolylketone immersed in solution. Both groups attributed their findings to the inclusion of the opposite enantiomer into the crystal structure as a contaminant.

The third main objective for secondary nucleation studies is to try to relate secondary nucleation to the leading dominance of certain biochemical enantiomers in nature. This particular phenomenon is termed chiral symmetry breaking, which was realized by Kondepudi²⁶ with the crystallization of sodium chlorate. A more descriptive review of this phenomenon will be presented later in this dissertation.

To begin to describe secondary nucleation, Qian and Botsaris²² developed a model they entitled Embryos Coagulation Secondary Nucleation (ECSN). The ECSN model combines three facets: classical nucleation theory, attractive van der Waals forces between clusters in solution, and coagulation of colloids in solution. Qian and Botsaris¹⁹

have published quantitative results that reinforce the ECSN model. The ECSN model predicts that an increased concentration of embryos exists surrounding a seed crystal, and the embryos will coagulate to form a cluster of critical size. This process would be an example of the seed crystal aiding the production of other nuclei, but as seen from this postulate, there is no transfer of chirality from the seed to the other nuclei. This particular mechanism of formation would then be in competition with conventional secondary nucleation mechanism (SCN)²⁷. Qian and Botsaris show through a variety of experiments that the competition between the ECSN and SCN mechanisms is temperature dependent.

The ECSN model predicts that the pre-crystal embryos are amorphous and only acquire chirality before the critical sized cluster is formed; this would indicate that the chirality of the crystal is attributed to random factors influencing the formation. The ECSN model is also able to explain the findings of Yokota and Toyokura²⁴ and Davey et al.²⁵; as an embryo is attracted toward the surface of the seed crystal through the van der Waals attraction, it is incorporated into the crystal structure, thus affecting the chiral purity of the crystal.

In early crystallization studies, it was noted that many inorganic salts crystallized into less stable polymorphs when their solutions were cooled quickly. Ostwald^{28, 29} took the results from the salt crystallizations and formulated a general theory; he stated that an unstable system would not necessarily convert to the most stable form of the system, but would rather progress in stages through forms that most closely resembled itself. This theory has been explored theoretically, but thermodynamics has been unable to prove this hypothesis³⁰. When combined with theoretical kinetics³¹, some facets of Ostwald's rule of stages have been proven, though no complete proof exists.

Chapter III.

Nonphotochemical Laser Induced Nucleation of Glycine

Introduction

Glycine, shown in Fig. 1, is the simplest amino acid and is achiral; interestingly, glycine can crystallize into 3 different polymorphs: α , β , and γ glycine, which is chiral. The crystal structure of α glycine was first established by Albrecht and Corey³². From the crystal structure, it was seen that double layers of hydrogen bonded molecules were packed via van der Waal forces. The β form of glycine is the most unstable and is generally not observed; for this study, the details of β glycine will not be discussed. From the perspective of chiral discrimination, γ glycine is the only form of glycine that proves to be interesting. Gamma glycine is a strong piezoelectric crystal and crystallizes with a trigonal hemihedral symmetry, which was first reported by Iitaka³³. Interestingly, several publications^{34, 35, 36} illustrated different methods of growing γ -glycine crystals. Iitaka³⁴ reported the growth of γ -glycine by slowly cooling aqueous solutions of glycine and acetic acid or ammonium hydroxide. Bhat and Dharmaprakash³⁵ reported the formation of γ -glycine from the crystallization of aqueous solutions with minute quantities of sodium chloride present, and Yu and Ng³⁶ illustrated further the importance of pH in the formation of γ -glycine by examining the quantities of γ -glycine at varying pH's.

It is well known that molecules with ionizable groups (amino and carboxyl among others) can crystallize into either neutral species or salts with counter ions. Shown in Figure 2 is a depiction of the various ionic forms of glycine in solution as a function of pH. The particular form of glycine in solution is obviously paramount to the preferred polymorph. In α -glycine, cyclic dimers pack together to form a double layer that is hydrogen bonded together, and α -glycine is typically formed unless the solution is acidic

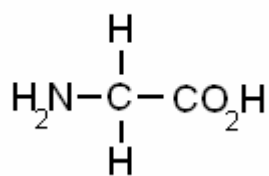


Figure 1. Molecular structure of glycine.

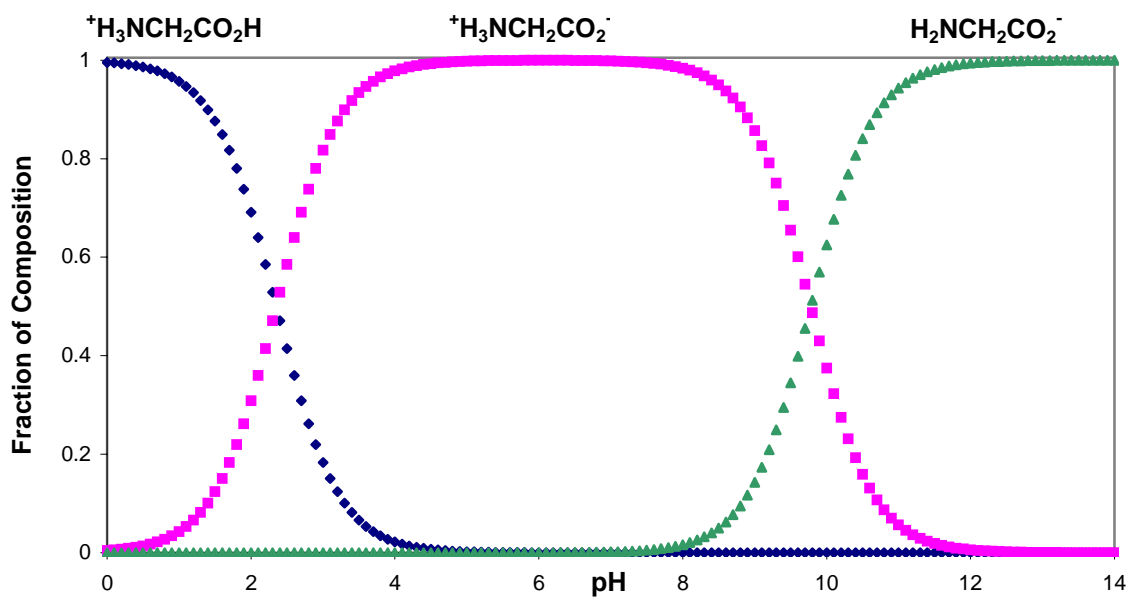


Figure 2. Fractional composition of glycine as a function of pH. It is seen that at low pH, the cationic (protonated amine) form is dominant, and at high pH, the anionic (carboxylate ion) is dominant. At biological range pH's, the zwitterionic form is most commonly observed.

or basic³⁴. The elemental growth of α -glycine has been previously explained³⁷ as being pictured as sheets of glycine molecules positioned perpendicular to the b-axis of the molecule. Each sheet of hydrogen bonded molecules forms a chain and is hydrogen bonded to an opposing sheet to form a bilayer, and the bilayers pack together via van der Waals forces. Conversely, γ -glycine crystallizes into helical chains with a 3 fold symmetry that are packed together hexagonally through lateral hydrogen bonds³⁴. Because of the helical nature, γ -glycine possesses chirality that is established through the solid state instead of a traditional chiral carbon center.

Identification of α - and γ -glycine can be performed through a variety of means. X-ray diffraction (XRD) was the original technique used to find the crystal structures for glycine polymorphs^{32, 33}. Other techniques that have been used to distinguish the presence of α - and γ -glycine are solid state ^{13}C NMR and Raman spectroscopy^{39, 40}. In the solid state ^{13}C spectrum, the C=O carbon of α -glycine occurs at $\delta=176.50$ ppm, while the C=O carbon of γ -glycine occurs at $\delta=174.60$ ppm. The reported peaks are specific to the carboxyl carbon and appear at different chemical shifts due to the slight differences in the hydrogen bonding in the solid state. The Raman spectrum shows that γ -glycine possesses two vibrations around 1340 cm^{-1} , while α -glycine has vibrations at 1320 and 1410 cm^{-1} .

In 1996, Garetz et al.⁴¹ published a work regarding the photochemical induced nucleation of supersaturated urea solutions. Using 1064 nm pulses from a Nd:YAG laser, they were able to spontaneously nucleate solutions of urea, and interestingly, they found that the polarization of the laser dictated the plane of growth for the initially formed crystals. The interpretation was that the electric field of the light was aligning the molecules in the path of the light (vertical or horizontal depending upon the polarization) similar to an optical Kerr effect⁴². Briefly, the optical Kerr effect in liquids states that an incident electric field induces a dipole moment in the liquid. The incident electric field then simultaneously interacts with the induced dipole moment applying a torque that causes the molecule to align its most polarizable axis parallel to the electric field. Garetz et al. termed this phenomenon for urea nonphotochemical laser induced nucleation (NPLIN).

Garetz extended the NPLIN work from urea to aqueous solutions of glycine⁴³. Supersaturated solutions, concentrations ranging from 3.7 to 3.9 M, of glycine were prepared and sealed in screw-cap vials and ‘aged’ an appropriate time. It was suggested⁴⁴ that ‘aging’ allowed larger glycine clusters to form, thus increasing the probability of nucleation. Using 1064 nm radiation from a Quanta-Ray DCR Nd:YAG laser, peak intensities on the glycine solutions were estimated to be $0.7 (\pm 10\%) \text{ GW/cm}^2$ with the assumption that the circular vial provided a slight focusing for the radiation. Samples were exposed to radiation for one minute before resealing and allowing for glycine to nucleate. Crystals were typically observed 30 minutes after exposure to the laser, though solutions did not nucleate for every exposure to the laser. The crystals that were formed were analyzed with XRD. Interestingly, it was found that γ -glycine crystals were formed during this process, whereas α glycine would typically crystallize in the absence of laser light.

Garetz et al.⁴⁵ later investigated the effects of polarization of the incident laser upon the crystallizing glycine solutions. The experimental details for these sets of experiments were consistent with the previous study except that a $\lambda/4$ waveplate was used to generate circularly polarized light. The results of these experiments were that linearly polarized light efficiently produced γ -glycine crystals via NPLIN and that α -glycine crystallized from circularly polarized light. These results appeared to be consistent with the earlier proposed optical Kerr effect. Briefly, the polarizability of the γ -glycine helix most closely resembles that of a rod and is most efficiently aligned via linearly polarized light. Conversely, the bilayers of α -glycine are similar to disks and are most easily aligned by circularly polarized light, thus the polarization of the laser dictated the alignment of glycine clusters.

McCann and Chen⁴⁶ performed initial studies on the effects of irradiating water and carbon tetrachloride solutions with intense radiation from a Quanta-Ray DCR Nd:YAG laser ($\lambda=266$ and 355 nm). The pH of the solutions was monitored via an Orian pH meter, and for an aqueous solution saturated with CCl_4 , irradiation with 266 nm light for five minutes dropped the pH from 5.76 to 3.62. Unfortunately, peak powers for the experiments are not listed, but McCann and Chen did demonstrate that lasers are capable

of greatly influencing the pH of solutions. This will be explored with respect to NPLIN of glycine.

The present experiments were carried out to confirm the NPLIN results of Garetz et al.¹⁴. Further, the experiments examined the effects of focusing the laser light with a lens rather than relying upon the self-focusing of the vials. The goals were to learn more about NPLIN.

Experimental

Supersaturated solutions of glycine were prepared with glycine purchased from Sigma-Aldrich and HPLC grade water; the glycine was not further purified. Concentrations of the solutions ranged from 3.7 to 3.9 M ($c_{\text{sat}} = 2.69 \text{ M}$ at 21°C) and were prepared by dissolving the appropriate amount of glycine in solution, heating the sample up, transporting portions of the sample to 1.3 cm diameter vials, and then allowing the solutions to cool for three days. The three day period also served to guarantee that the solution would not spontaneously crystallize. Samples were analyzed using a ^{13}C 400 MHz Solid State Varian NMR spectrometer, Philips X'Pert Diffractometer, and Dilor XY800 Raman spectrometer.

A total of 30 vials were utilized as controls for the series of glycine experiments. The first set of experiments utilized a Quanta-Ray DCR Nd:YAG laser ($\lambda=1064$) with an average power of 700 mW. The beam was put through a $\frac{1}{4}$ waveplate before passing through an aperture and the side of the vial containing the glycine sample; Figure 3 shows the model geometry for these experiments. A total of 10 samples were irradiated with linearly polarized light (LPL) and 10 samples were irradiated with right circularly polarized light (RCPL).

Further experiments continued to utilize the Quanta-Ray DCR Nd:YAG laser fundamental ($\lambda=1064 \text{ nm}$) and second harmonic ($\lambda=532 \text{ nm}$) with an average power of 800 mW. The experimental geometry is shown in Figure 4; the light passes through a $\frac{1}{4}$ waveplate before being focused with a 5 cm focal length lens through the surface of the

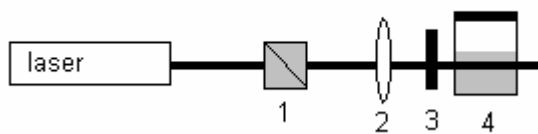


Figure 3. Experimental schematic for repeating experiments by Garetz et al. (1) a polarizer to ensure polarization (2) $\lambda/4$ waveplate (3) aperture (4) sample

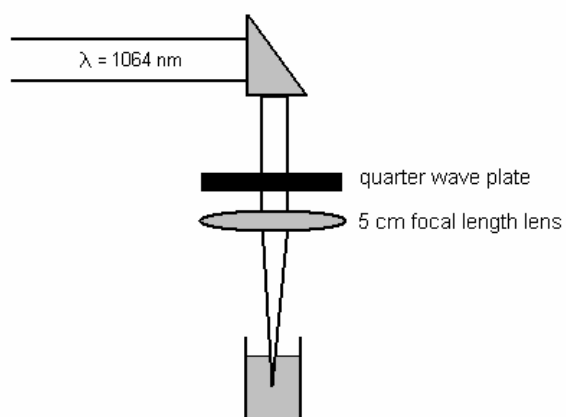


Figure 4. Schematic diagram for apparatus to focus polarized light into solution. Wavelength of radiation is 1064, 532, 514.5 nm.

solution. For 1064 nm light, 41 solutions were irradiated with LPL and 17 solutions were irradiated with RCPL. For 532 nm light, 6 solutions were irradiated with LPL and 4 solutions were irradiated with RCPL. Another set of experiments increased the average power of the fundamental and second harmonic of the Quanta-Ray DCR Nd:YAG to 1.5 W. For linearly polarized 1064 nm radiation, 21 samples were irradiated; for both RCPL and LCPL 6 samples were irradiated. At 532 nm, 4 samples were irradiated with LPL and 5 samples with RCPL.

To investigate the effects of continuous wave (CW) lasers upon crystallization, an Ar-Ion laser operating at 514.5 nm CW laser with an average power of 1.8 W was used to irradiate samples with both LPL and RCPL. A total of two samples were irradiated with LPL, and 23 samples were irradiated with RCPL.

The effect of pH upon laser induced crystallization in glycine was also investigated by adjusting the pH of the supersaturated glycine solutions to 4.0 by the addition of the appropriate amount of concentrated hydrochloric acid. For these experiments, 14 solutions served as controls, while 9 other solutions were irradiated with 700 mW 1064 nm LPL. Another set of experiments investigated the effects of 700 mW 1064 nm radiation on the pH of supersaturated glycine solutions (not adjusted to pH=4.0) over time. The pH was monitored with a standardized pH meter.

The last set of experiments relied upon the geometry shown in Figure 5; the metal 'boat' served as a means to generate a sound wave to investigate the effects of sound propagation (compression waves) in the mechanism of crystallization. Since each of the previous experiments induced a sound wave in solution, this present set of experiments will isolate the effects of the sound wave on the crystallization of glycine. A total of 8 solutions were exposed to the sound wave.

Results and Discussion

Results for all crystallization experiments are shown in Table 1. For a sample to be termed containing γ -glycine, the population of γ -glycine must be equivalent to the

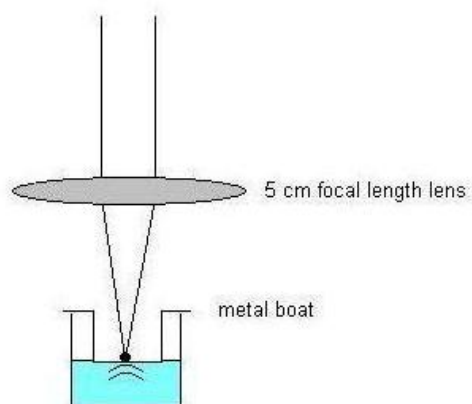


Figure 5. Experimental geometry for the sound wave nucleation experiments. The laser is focused onto a metal ‘boat’ that will generate a sharp sound wave that vibrates through the solution.

Table 1. Results for the compilation of glycine crystallization experiments. The samples column refers to the total number of samples irradiated, and the α and γ columns refer to the number of appearances of either α or γ crystals from samples that crystallized.

λ (nm)	Polarization	Power (W)	Samples	α	γ
1064	LPL	unfocused 0.7	10	4	5
	RCPL	unfocused 0.7	10	5	4
1064	LPL	0.8	41	10	0
	RCPL	0.8	17	5	1
1064	LPL	1.5	21	21	0
	RCPL	1.5	6	2	4
	LCPL	1.5	6	2	4
532	LPL	0.8	6	3	0
	RCPL	0.8	4	4	0
532	LPL	1.5	4	3	1
	RCPL	1.5	5	5	0
CW 514.5	LPL	1.8	2	2	0
	RCPL	1.8	23	10	0

pH = 4.0

1064	LPL	0.7	9	0	9
------	-----	-----	---	---	---

Controls

Control	-----	-----	10	10	0
pH = 4.0	-----	-----	14	4	10
Sound	-----	-----	8	4	4

portion of α -glycine present (50% γ , 50% α). All twenty of the control samples crystallized to form α crystals. The experimental conditions in the set of experiments with 700 mW 1064 nm radiation entering from the side of the vial were those similar to those used by Garetz et al.¹²; nine out of the 10 solutions irradiated with LPL crystallized with 4 being α and 5 γ . Similarly, 9 out of 10 crystallized that were irradiated with RCPL forming 5 α and 4 γ .

Of the 41 solutions that were irradiated with 800 mW 1064 LPL, 10 solutions crystallized with all crystals being α . Of the 17 solutions irradiated with 800 mW 1064 RCPL, 6 crystallized with 5 being α and one being γ . Of the samples irradiated with 1.5 W 1064 nm light, 21 samples crystallized for LPL with all samples being α , 6 samples crystallized for RCPL with 2 samples being α and 4 γ , and 6 samples crystallized for LCPL with 2 being α and 4 being γ . The 800 mW 532 nm experiments produced only α -glycine crystals. For the samples that were irradiated with 1.5 W 532 nm LPL, all 4 crystallized with 3 being α and 1 γ ; all 5 samples irradiated with 1.5 W 532 RCPL crystallized with 5 being α . The results for the samples that were irradiated with 514.5 CW nm light were as follows: both of the samples irradiated with LPL crystallized to form α crystals, and of the 23 samples irradiated with RCPL, only 10 crystallized, and all 10 of the samples were α crystals.

For the experiments that have been adjusted to a pH of 4.0, all 14 control samples crystallized with 4 being α and 10 being γ crystals. All 9 samples that were irradiated with 700 mW LPL crystallized into γ crystals. Further experiments showed that the pH of supersaturated glycine solutions dropped over the course of minutes when being irradiated with 700 mW 1064 nm light. All of the samples in the sound experiments crystallized to form α crystals.

The results of the experiments appear to indicate that wavelength does not correlate to the formation of γ -glycine. Rather the most efficient means of producing γ -glycine that was found was the use of high power laser intensities. Figures 6 and 7 show the effects on pH and temperature of irradiating solutions of glycine with 1064 nm light at 700 mW. The concentrations of the pH samples vary, explaining the slightly different

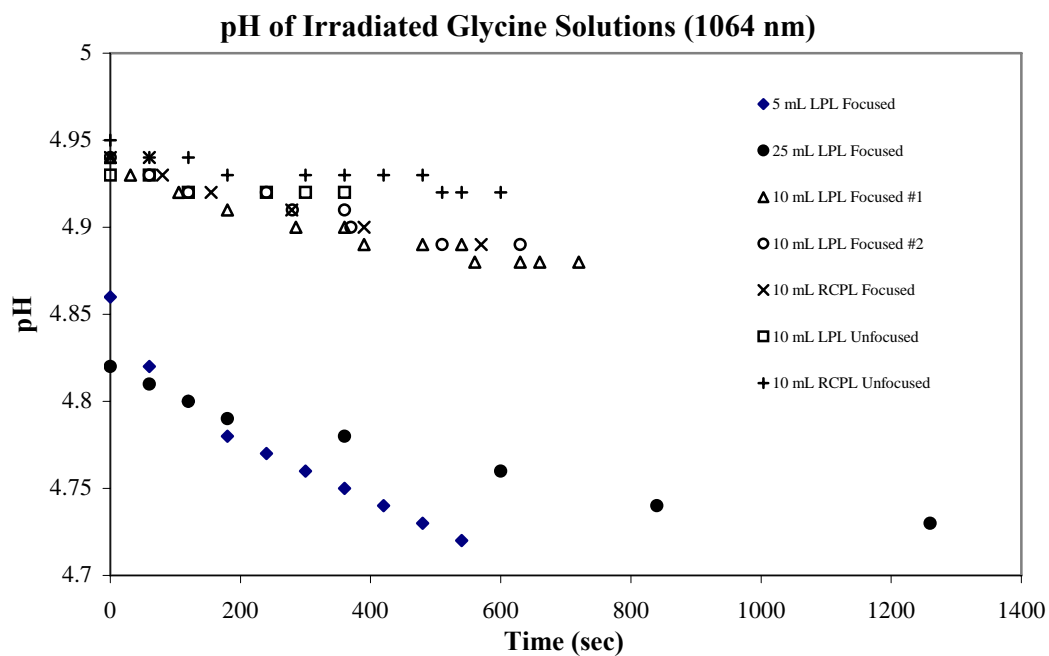


Figure 6. pH of glycine solutions (concentrations vary) irradiated with focused (or unfocused) 700 mW 1064 nm light as a function of time.

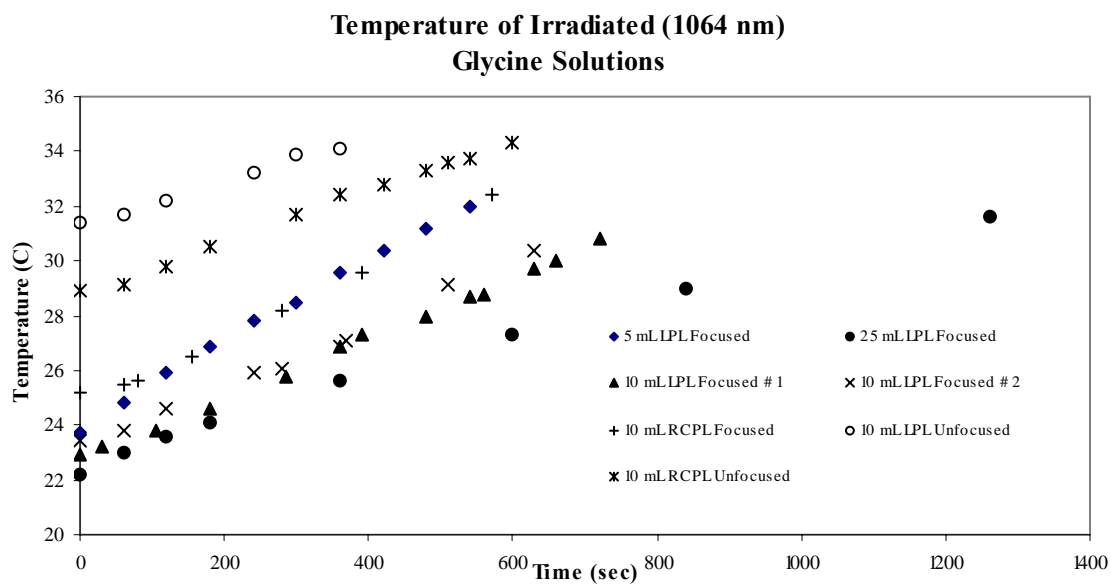


Figure 7. Results from irradiating glycine solutions (varying solution sizes) with 700 mW 1064 radiation.

pH at time = 0 seconds, and the sample sizes were varied for these experiments. Figure 6 shows that the longer a solution is irradiated with 1064 nm radiation, the lower the pH will drop due to the irradiation. Likewise, the temperatures of irradiated solutions rise as a function of time. The effects of irradiation on pH are helpful for understanding the formation of γ -glycine. As mentioned in the introduction, acidic or basic solutions have a propensity to crystallize γ -glycine, and since the laser has been shown to decrease the pH of the glycine solution, it is a factor that may contribute to the formation of γ -glycine. Similar to McCann⁴⁶, the laser is able to photochemically form ions that result in a decrease of the pH. It should be noted that a one-photon UV-Vis spectrum of a saturated glycine solution indicated no absorption at 532 or 1064 nm. Multi-photon processes, however, may occur.

The results for the experiments with glycine solutions at a pre-established pH of 4.0 did vary slightly from those of the pH control group. The pH control group had roughly twice as many γ -glycine crystals as α -glycine crystals, but when irradiated with focused 700 mW 1064 nm light, the crystals were exclusively γ -glycine. This would seem to indicate that the perturbative force of the laser light was able to induce nucleation of γ -glycine rather than a mixture of α - and γ -glycine crystals.

The experiments with focused lasers generated a sound wave in the solution as a result of the collapsing bubble. The primary effect from this sound wave was the propagation of a pressure wave through the solution inducing more collisions of glycine molecules, with themselves. The increased rate of collisions may lead to a preponderance of crystals being formed through pressure-wave effects and not NPLIN. The results of the sound wave experiments show that the expected polymorph is crystallized, α -glycine, but an interesting feature that should be noted is that many crystals, smaller than 1 mm in size, were formed quickly. During the experiments, 'micro'-crystals of glycine could be seen 'falling' from the bottom of the metal boat. The sound wave experiments did result in producing many more crystals of a much smaller size than was typically observed. This observation is probably a result of the distinct surface for the formation of the sound wave; the sound waves generated as a result of focusing the laser in the middle of the solution were less distinct than the surface

generated sound waves and could be expected not to carry as much force in their propagation. If the sound wave were the only mechanism for the formation of glycine crystals, only α -glycine crystals should appear, but since γ -glycine is observed, further credence is lent to NPLIN.

The effect of pH is able to explain the differences in the results from the focused laser experiments, but several experiments were performed with conditions nearly identical to those of Garetz, but the results did not completely correlate with the results of Garetz. Rather than forming exclusively γ -glycine, as reported by Garetz, linearly polarized light experiments produced a mixture of α - and γ -glycine. This particular discrepancy could possibly result in differing definitions on what is classified as a γ -glycine crystal (any appearance of γ -glycine might be termed γ -glycine exclusively for Garetz), but the results from the right circularly polarized light gave results that agreed with the prior results of Garetz, which had reported that with RCPL, α -glycine was preferentially formed. The interpretation of these results became clearer with a published report by Sun and Garetz⁴⁷. The recent studies were an extension of the earlier glycine studies, but focused upon the effects of concentration, polarization, and wavelength dependence (among other variables) in glycine NPLIN. The results of their experiments did indicate a narrow range at which their prior results were true, but at the same experimental conditions, the temperature at which the crystallization occurred could influence the formation of polymorphs. For example, at a crystallizing temperature of 290 K and $c_{\text{sat}} = 2.6$, γ -glycine could be formed using CPL or LPL. Crystallizing temperatures were not recorded for the present experimental results, but the results now appear to be more congruent with the earlier work of Garetz with the recent release of further data.

Conclusion

Nonphotochemical laser induced nucleation of glycine is a process that has been experimentally demonstrated in non-focused laser studies and may have been demonstrated in the focused laser studies. In crystallization experiments, many variables

that affect a microscopic phenomenon are present and are nearly uncontrollable, which complicates a phenomenon that appears to be statistically based. The process of NPLIN is one that appears to be valuable for the biological community if the supersaturated concentrations were not necessary. At the current understanding of NPLIN, supersaturated solutions of the solute are necessary, which, for a variety of biological molecules (such as proteins) is not a reasonable cost for the discovery a complex crystal structure. More work is required to gain a more complete understanding of NPLIN.

Chapter IV.

Nonphotochemical Laser Induced Nucleation of Sodium Bromate

Introduction

Sodium bromate is an achiral molecule that crystallizes in the chiral $P2_13$ space group. Despite being isomorphous with sodium chlorate, sodium bromate crystals with the same absolute configuration as sodium chlorate crystal has been found to rotate plane polarized light in the opposite direction of sodium chlorate^{48, 49}. Several authors have studied the nature of the optical activity within sodium bromate crystals and formulated theories that describe the optical properties of such crystals. Two main classes of theories have been proposed to explain the nature of optical activity using electromagnetic theory^{50, 51, 52, 53} and atomic polarizability contributions^{54, 55, 56, 57, 58}. Ramachandran's work^{56, 57, 58} focused on being able to accurately calculate the rotatory power in quartz, sodium chlorate, and sodium bromate crystals using a first-order theory with the electric vector of the light interacting with the anisotropically polarizable atoms. In this study, Ramachandran replaced the multiple oxygen atoms within the chlorate or bromate groups with a single anisotropically polarizable particle and neglected the contributions from the sodium and halide atoms. Incidentally, he incorrectly assigned the same sign of optical rotation for both sodium chlorate and sodium bromate crystals. In 1967, Chandrasekhar et al. published⁵⁹ another attempt to calculate the optical rotatory dispersion from experimental measurements for both sodium chlorate and sodium bromate crystals. Their results were able to correctly assign the sign for the optical rotatory dispersion for both sodium chlorate and sodium bromate. Madhava⁶⁰ then obtained experimental results for the temperature variation of the optical properties for both sodium chlorate and sodium bromate which agreed well with the formulas that Chandrasekhar et al.⁵⁹ presented.

The study of the effect of light upon the growth of crystals is not a new endeavor; in fact, in 1913, Fisher⁶¹ published a review on the subject. The only compound that showed any evidence for an increasing of growth rate while being illuminated was $\text{Ba}(\text{ClO}_3)_2$. All of these studies utilized sunlight for their supply of radiation. Noboru's study⁶² showed that selenium whiskers in the gas phase were converted to crystalline form by the presence of light, and the growth rate was increased if the energy of the photons exceeded 2.5 eV. Incidentally, 2.5 eV is the dissociation energy for the Se-Se bond. The same study concluded that the inclusion of infrared rays in the radiation retarded the growth of the selenium crystals.

Kasatkin⁶³ studied the effect of light on the growth rate of the (100) face of sodium bromate crystals. The apparatus consisted of white light irradiating the crystals while the crystal was observed under a microscope. At constant temperature and supersaturation, the growth of the (100) face of sodium bromate crystals was more stable under dark conditions, but he concluded the growth rate did increase under the influence of the white light.

Previous studies focusing upon the chiral nature of sodium bromate crystals have been conducted in this laboratory and other laboratories. In these studies, nearly saturated solutions of sodium bromate were placed in petri dishes and allowed to evaporate and crystallize, and then the produced crystals were analyzed with Polaroid film to determine their handedness. Since only two forms exist, and those forms only differ in their handedness, one would expect a bimodal distribution of those forms to occur. This was not the case; rather a dominance of d-crystals was observed. The initial hypothesis was that a chiral impurity was disturbing the crystallization process, but repeated experiments at Wake Forest University, with no prior exposure to chemicals or personnel, indicated the same results. These results completely contradicted the results obtained from sodium chlorate experiments, despite the two crystals being isomorphous with one another.

Sodium Chlorate

Kipping and Pope's study⁶⁴ looked at the frequency of enantiomorphs when NaClO_3 was crystallized from water. They speculated that there was no reason why one of the chiral forms should crystallize preferentially over the other form. After collecting NaClO_3 and examining its handedness by polarimetry, they concluded that sodium chlorate does spontaneously crystallize to either the laevo- or dextro- form of the crystal when enough samples are taken.

Another study²³ looked at the effect of secondary nucleation of sodium chlorate crystals under a range of conditions (supersaturation, impurity concentration, supercooling, etc.). From the varied conditions, specific conditions would produce only the enantiomorph corresponding to the seed crystal, but consequently, other conditions existed where both enantiomorphs would crystallize from the seeded solution. These results led the authors to conclude that multiple mechanisms exist for secondary nucleation.

A startling observation²⁶ was reported in 1990 that demonstrated spontaneous chiral autocatalytic resolution with crystallizing sodium chlorate crystals. Kondepudi's research agreed with the conclusions of Kipping and Pope, that if sodium chlorate will spontaneously crystallize into equal proportions of levo- or dextro- handed crystals, given enough data sampling. Kondepudi then made a simple adjustment to the experimental procedure that produced spectacular results; instead of letting the sodium chlorate solutions evaporate to induce crystallization, Kondepudi stirred the solutions while they were crystallizing. This one adjustment led to each batch of crystals being nearly entirely (+) or (-) in every experiment, while having no predisposition towards one form over the other.

Kondepudi et al.²⁶ concluded that secondary nucleation must be responsible for their observation, and stirring had been previously shown²⁰ to promote secondary nucleation. Another study by Kondepudi et al.⁶⁵ used computer simulations to investigate the kinetics of the secondary nucleation. Their simulations assumed the crystallizing solutions to have homogeneous parameters (temperature, concentration, etc.) throughout

the solution, which though maybe not entirely accurate, simplifies the problem at hand. The results from their study were that a minimum crystal size existed for the secondary nucleation mechanism to spontaneously break symmetry macroscopically.

Microscopically, this would indicate that the first crystal formed within the solution must grow to a “critical” size before fragmenting into a pair of crystals that would continue to grow with the same handedness of each other.

A study by Szurgot and Szurgot⁶⁶ seems to bring the results of Kondepudi’s stirring experiments into question. In this experiment, sodium chlorate crystals were grown in the bottom of a crystallizer at differing temperatures; the first crystal of each batch, along with each crystal from each batch were analyzed to determine the handedness of the crystals. Szurgot and Szurgot conclude that they have shown a trimodal distribution when the number of crystals from the batch is less than 50. A similar critique within Kipping and Pope’s work⁶⁴ was that previous experiments did not have enough samples to guarantee that symmetry breaking was present within the observed results; that may be the case within this work since the trimodal distribution is only present with the smaller crystal population.

In 2004, Viedma⁶⁷ demonstrated that secondary nucleation may not be the only explanation for the mechanism of autocatalytic chiral resolution in sodium chlorate stirred crystallization. The supersaturated sodium chlorate solutions were prepared and not allowed to spontaneously crystallize; the solutions were then stirred rigorously (approximately 1000 rpm) which resulted in an almost instantaneous appearance of microcrystals. The microcrystals were estimated to be approximately 20 μm in diameter. An analysis of the handedness of the microcrystals revealed that they were almost completely the same morphology. The rate at which the crystals appear would seem to indicate that the mechanism of secondary nucleation is not plausible in this instance, yet the handedness of all of the crystals remain the same. It should be noted that these results do not preclude Kondepudi’s assertion, that his experimental results are attributable to secondary nucleation, from being true. The research seems to indicate that differing scenarios and mechanisms may be responsible for the spontaneous chiral resolution of sodium chlorate crystals.

Despite being isomorphous with sodium bromate, sodium chlorate crystals are very different from the bromate analogue. Sodium chlorate crystals will normally crystallize into equal populations of both chiral forms, while the dextro- form of sodium bromate crystals has been found to be more prevalent in unpublished results from UT and Wake Forest laboratories. Kasatkin⁶³ showed that white light can increase the growth rate of sodium bromate crystals, but what effects does highly intense and monochromatic radiation display in sodium bromate crystallization? Can the excess of one enantiomeric form of sodium bromate be reduced through the use of radiation? This study intends to examine these questions regarding sodium bromate crystallization.

Experimental

Sodium bromate, NaBrO₃, solutions were prepared with sodium bromate provided from Sigma Aldrich and HPLC grade water. Concentrations typically ranged from 2.75 molal to 2.81 molal; the saturation concentration of sodium bromate is 2.48 molal. To achieve supersaturation, solutions were heated to ~60 °C while being stirred. After dissolving, the solution was transferred into either smaller vials or Petri dishes, depending upon the experiment. The vials typically contained ~10 mL of solution and were capped upon the addition of the sodium bromate solution. Solutions were then allowed to slowly cool back to room temperature over a period of typically three days. If the solution recrystallized within the three day time period, the vial was removed from the pool of samples. Some later sample solutions of sodium bromate were prepared with recrystallized sodium bromate from previous experiments. The previously crystallized sodium bromate was ground into finer pieces using a mortar and pestle before being added in appropriate amounts to solutions.

A set of experiments investigated the influence of the laser's power upon the polarization of the produced sodium bromate crystals. Solutions were prepared as described previously. The fundamental ($\lambda=1064$ nm) of a Quanta-Ray DCR Nd:YAG was used as the radiation source. Both linearly and right circularly polarized light were investigated. After passing through a quarter wave plate (to generate the desired

polarization), the radiation was focused through the air-solution interface with a 5 cm focal length lens. The experimental geometry is shown in Figure 1. The unfocused power of the laser was measured with the use of an Ophir AN/2 laser power meter. Each sample vial was irradiated for approximately one minute and was uncapped during this time. After being irradiated, solutions were recapped and not exposed to air until after crystallizing. A set of control samples was also uncapped for approximately one minute, but these samples were not exposed to the laser light. The average unfocused powers that were investigated were 0.5, 0.9, 1.2, and 1.5 W. The number of solutions that were irradiated with linearly polarized light at each power follow as: 54 solutions at 0.5 W, 54 solutions at 0.9 W, 38 solutions at 1.2 W, and 18 solutions at 1.5 W. For the right circularly polarized light samples, 35 samples were irradiated with 0.5 W, 20 samples were irradiated with 0.9 W, 18 samples were irradiated with 1.2 W, and 18 samples were irradiated with 1.5 W. Over all of the experiments, a total of 29 control samples were prepared.

Another set of experiments was conducted to analyze the effects of the sound waves in the solution. Solutions were prepared and treated identically as before, only the manner of irradiation changed. The sound waves were generated by focusing the laser with a 5 cm focal length lens onto a metal “boat” (~ 1 mm thick) that was placed on the surface of the solution. The laser power was 1.5 W to generate strong sound waves from the boat; 20 samples were “irradiated” for approximately one minute.

To determine whether crystallization in the open atmosphere influenced the polarization of produced crystals, a series of solutions were allowed to evaporate and crystallize in Petri dishes. A total of 8 Petri dishes were filled with the sodium bromate solution. The resulting crystals from each dish were then divided into vials before being analyzed. Each vial was labeled with which Petri dish its crystals originated.

The sodium bromate crystals that were produced during these experiments were often too small to analyze their polarizations by hand. To quantitate the polarizations of the crystals, the methodology developed by Bartus and Vogl⁶⁸ was utilized. Briefly, the

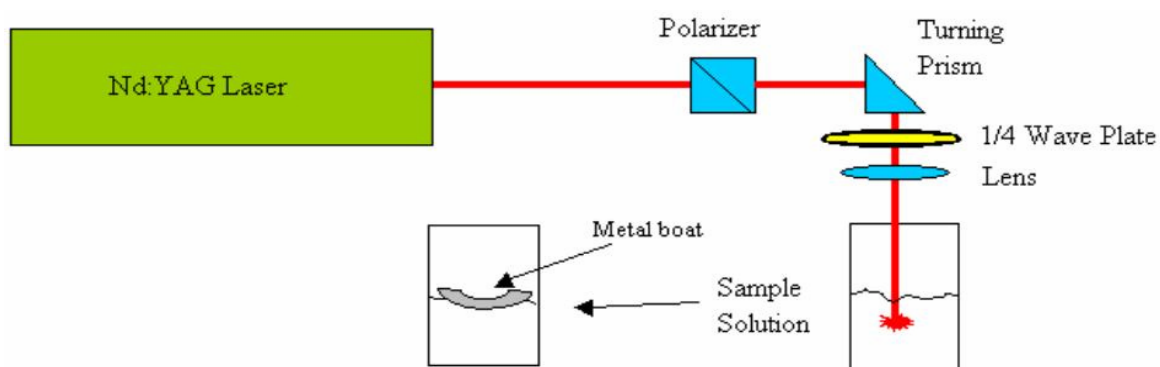


Figure 1. Experimental setup for the irradiation of the sodium bromate solutions. For the sound experiments, the metal boat was on top of the solution while irradiating.

crystals that were formed within each vial were harvested by removing the excess water and drying the resulting crystals. The harvested crystals were then ground into smaller crystal particles using a mortar and pestle. The polarization of the ground crystals was then determined by measuring the optical rotation by suspending the crystals in a solution of carbon disulfide, CS₂, and carbon tetrachloride, CCl₄, that was matched to the index of refraction of the sodium bromate crystals. The optimum mixture was 1 mL of CS₂ and 200 µL of CCl₄. To know the mass of crystals that were measured, initial masses of the ground sodium bromate crystals were recorded, and final masses of extra sodium bromate crystals were measured. The measured optical rotations were then correlated to the amount of sodium bromate crystals measured to give a measured rotation per gram of sodium bromate. These mass related rotations were then compared to known crystals (either (+) or (-) rotations) which underwent the same above procedure to give values for the mass related rotation for a pure (+) or (-) crystal.

Results and Discussion

The result for the standard (known polarization) NaBrO₃ crystals, the average optical rotation in degrees (at 589 nm) per gram, is ± 11.902 °/g (with the plus and minus sign corresponding to the correct polarization.). With these data, all other experiments can be related to the enantiomeric excess of the crystal, which is given by

$$EE = \frac{[\alpha]_0^p}{[\alpha]^p} \quad \text{Eq. 1}$$

where $[\alpha]_0^p$ is the observed optical rotation at the sodium D line and $[\alpha]^p$ is the optical rotation at the sodium D line for a pure (+) crystal.

For linearly polarized light experiments, the results are summarized in Table 1. Of the 54 solutions irradiated with 0.5 W linearly polarized light, 15 crystallized, and the average optical rotation per gram was 0.175 °/g. The 54 trials with 0.9 W LPL produced 21 solutions that crystallized; the average optical rotation per gram was -1.815 °/g. At 1.2 W, the linearly polarized light crystallized 12 of the 38 irradiated solutions with an average optical rotation per gram of -0.452 °/g. A total of 16 samples of the 18 samples

Table 1. Results for linearly polarized light irradiated sodium bromate.

Power (W)	Irradiated	Crystallized	Average °/g	Std. Dev.
0.5	54	15	0.175	4.437
0.9	54	21	-1.815	6.697
1.2	38	12	-0.452	2.491
1.5	18	16	-0.489	4.536

that were irradiated with 1.5 W LPL crystallized to give an average optical rotation per gram of $-0.489^{\circ}/\text{g}$. Figure 2 shows the compilation of the all of the experiments for LPL as a result of the enantiomeric excess along with the results for the control experiments.

The results for the right circularly polarized light experiments are given in Table 2. Of the 35 samples irradiated with 0.5 W right circularly polarized light, 21 crystallized with an average optical rotation of $1.399^{\circ}/\text{g}$. Nineteen of the 20 samples that were exposed to 0.9 W RCPL crystallized with an average optical rotation of $1.025^{\circ}/\text{g}$. A total of 17 of the 18 samples irradiated with 1.2 W RCPL crystallized with an average optical rotation of $-0.866^{\circ}/\text{g}$. Of the 18 samples that were irradiated with 1.5 W RCPL, 11 crystallized with an average optical rotation of $-0.397^{\circ}/\text{g}$. Figure 3 shows the compilation of the all of the experiments for RCPL as a result of the enantiomeric excess along with the results for the control experiments.

The results for the sound generated crystals are presented in Table 3. Of the 20 sodium bromate solutions that were exposed to sound waves, 16 crystallized with an average rotation of $-3.91^{\circ}/\text{g}$ with a standard deviation of $2.62^{\circ}/\text{g}$. All of the 18 irradiated sodium chlorate solutions crystallized with an average rotation of $1.72 \pm 4.12^{\circ}/\text{g}$. The results for the control samples and the Petri dish samples are presented in Table 4. Of the 29 prepared control samples, 16 crystallized with an average optical rotation of $0.252^{\circ}/\text{g}$. The 8 Petri dishes were subdivided into 32 samples, and the average optical rotation of the samples was $-5.082^{\circ}/\text{g}$. Figure 4 shows the compilation of all of the sound and Petri dish experiments compared with the sodium bromate control sample as a result of enantiomeric excess.

From a kinetic point of view, irradiating the sodium bromate solutions caused crystallization to occur much faster than a solution that had not been irradiated. This particular observation is easily attributable to the sound wave that is being produced to cause more frequent collisions, but as indicated by Fig. 4, the rotations of the formed crystals are all negative, thereby the sound mechanism is unable to account for the differences that seem to appear when the polarized light is used. In the sound generated crystallization experiments, the crystals appear readily in the solution upon the introduction of sound, and the solution becomes cloudy with the crystals being

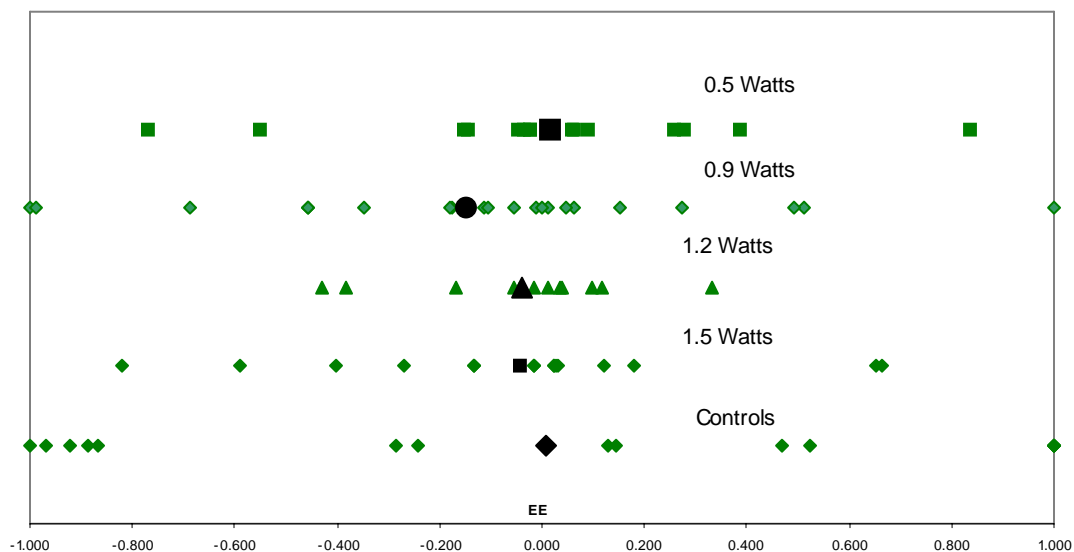


Figure 2. Comparison of the results for the linearly polarized light experiments for sodium bromate. The x-axis corresponds to the enantiomeric excess percent purity. The larger, darkened figure for each data set represents the average for each data set's experimental conditions.

Table 2. Results for the right circularly polarized light irradiated sodium bromate.

Power (W)	Irradiated	Crystallized	Average °/g	Std. Dev.
0.5	35	21	1.399	5.959
0.9	20	19	1.025	1.801
1.2	18	17	-0.866	4.448
1.5	18	11	-0.397	1.095

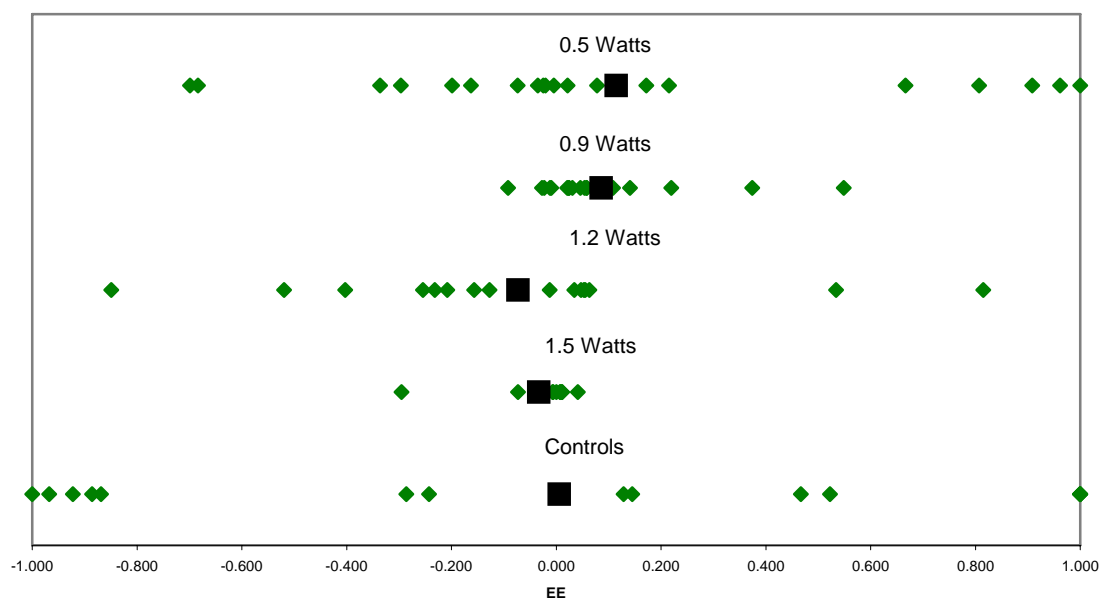


Figure 3. Comparison of the results for the right circularly polarized light experiments for sodium bromate. The x-axis corresponds to the enantiomeric excess percent purity. The larger, darkened figure for each data set represents the average for each data set's experimental conditions.

Table 3. Results for the sound generated sodium bromate crystals.

Sample	Prepared	Crystallized	Average %g	Std. Dev.
NaBrO ₃	20	16	-3.91	2.62

Table 4. Results for the control and Petri dish experiments for sodium bromate.

	Prepared	Crystallized	Average %g	Std. Dev.
Control	29	16	0.252	9.872
Petri	32	32	-5.082	6.379

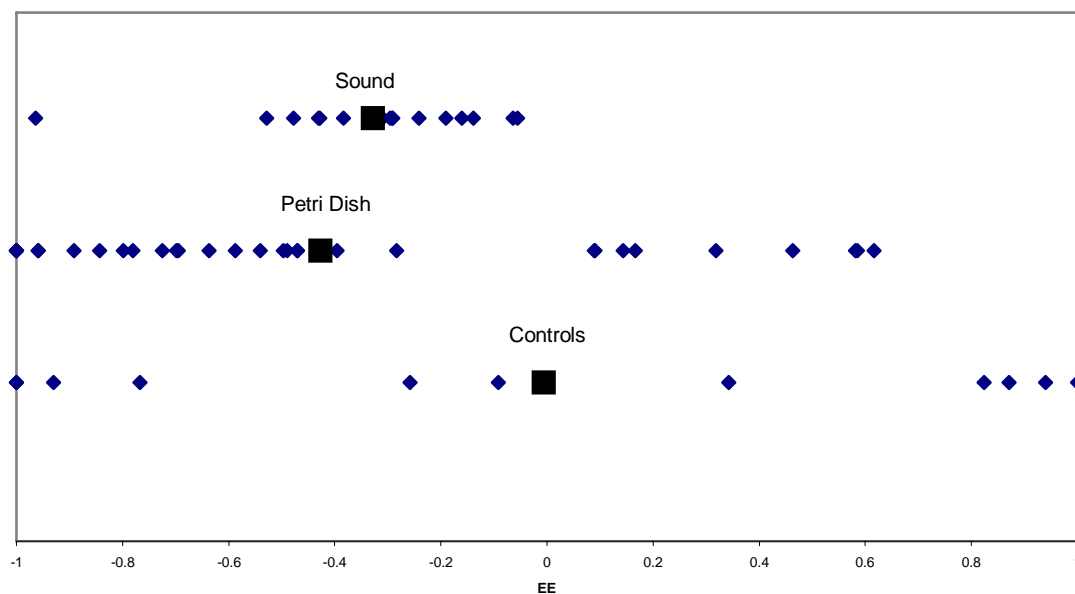


Figure 4. Comparison of the results for the sound and Petri dish experiments for sodium bromate. The X-axis corresponds to the enantiomeric excess percent purity. The larger, darkened figure for each data set represents the average value for each data set's experimental conditions.

“shaken” out of solution. This particular scenario is similar to the description offered by Viedma⁶⁷ for the stirring experiments for sodium chlorate crystallization. Unlike that found in Viedma’s study, the rotations show that crystals are not of pure (+) or pure (-), but do favor the negative rotation slightly, which is contrary to the control samples. Since the final weights of the samples were not measured, unfortunately there is not a way to accurately determine the purity of the sound generated trials for comparison purposes. These results though do tend to mimic the results obtained by Viedma, and the experimental conditions could be considered to be comparable.

Starting the analysis of the power dependent crystallization with the high power irradiations (1.2 and 1.5 W), one can see that the average rotation per gram of sample for both linearly and right circularly polarized light begins to approach one another. For 1.2 W, the values are -0.452 °/g and -0.866 °/g respectively, while 1.5 W is -0.489 °/g and -0.397 °/g respectively. This convergence of the average rotation values is due to the overriding mechanism of the formation of the crystals. At lower powers, though a sound wave is being formed from the focusing of the laser, the formation of the microscopic nuclei is more likely due to the electromagnetic field orienting pre-existing pre-critically sized clusters in solution. Garetz et al.⁴¹ suggested that 1064 nm light was able to align prenucleated clusters of urea and thereby enhance the rate of nucleation; other studies^{43, 45} indicate that laser light is efficient in enhancing, and directing, crystallization of glycine solutions. At the higher power, this alignment process, though occurring, is competing against the increased number of collisions due to the sound wave compressing the solution. That the compression mechanism is dominating at higher powers is seen as the average rotation values begin to converge to the same value, and looking at Table 3, it appears as though the sound induced trials have a comparable value as to the higher power trials.

The effect of the two lower power values, 0.5 and 0.9 W, on crystallization is more difficult to explain. For 0.5 W linearly polarized light, the average rotation was 0.175 degrees per gram, which is very close to the control value of 0.252 degrees per gram. Interestingly, the average value for right circularly polarized light samples had a rotation of 1.399 °/g, which happens to be over one degree higher than the samples

generated with linearly polarized light. At 0.9 W, the linearly polarized light samples' average rotation drops to $-1.815^{\circ}/\text{g}$, while the right circularly polarized light samples' average rotation only drops to $1.025^{\circ}/\text{g}$. The power level of 0.9 W is the most glaring difference between the two polarizations, but the reason for the difference is not completely certain. The chirality from the sodium bromate crystals is due to the helical arrangement of the oxygen atoms within the lattice structure; the helical nature of the crystal lattice would give the crystal structure a rod-like polarizability. Looking at Garetz's work⁴⁵, the shape of the polarizability for the molecule can begin possibly to explain behavior stemming from differing polarizations of light. Garetz showed that linearly polarized light is able to effectively align clusters or lattices with rod-like polarizabilities. The average rotation value for linearly polarized irradiated crystals was only -1.815 degrees per gram, but the standard deviation of this value was $6.697^{\circ}/\text{g}$. Two things should be noted with the knowledge of the standard deviation: first, only 21 samples were measured, so the data may represent only a sampling of a far end of a gaussian distribution, and secondly, this deviation may show that (+) rotations are achievable with linearly polarized light, though the tendency is towards a (-) rotation. This observation seems to fit in with the observation that rapid crystallizations, such as in the sound induced experiments, give negative values of rotation, but the wide standard deviation range could result from the lack of high statistical sampling and that the linearly polarized light does not have a predisposition towards either a (+) or a (-) rotation. When considering the 0.9 W results for RCPL, a comparison to the control data should be made; the control samples had an average rotation of $0.252^{\circ}/\text{g}$ with a standard deviation of $9.872^{\circ}/\text{g}$. The average rotation for a pure gram of sodium bromate crystals is ± 11.902 degrees; the standard deviation for the RCPL trials represents almost the value of a pure crystal. Looking at the control data again, the sodium bromate that is not irradiated, but open to the atmosphere for approximately one minute, tends to crystallize in either the (+) or (-) form, but tends to slightly favor a positive rotation form of the crystal. The 0.9 W right circularly polarized light samples have an average rotation of $1.025^{\circ}/\text{g}$ with a standard deviation of $1.801^{\circ}/\text{g}$. This standard deviation is markedly smaller than the linearly polarized light equivalent; and the interpretation of the right

circularly polarized light data for this power is that the results tend to mimic those of the control samples except with a slightly greater propensity to favor a positive rotation. A greater question still remains: why do the control samples and sound wave samples have different results?

Sound wave induced crystallization of sodium bromate shows a slight propensity to favor crystallizing to the (-) form, which is in contrast to the sodium bromate controls, which are centered on an EE of zero. The non-zero average rotation favors the interpretation that is similar to that of Viedma⁶⁷ that a vigorous crystallization process will give a slight excess of one handedness over the other. In the sound induced crystallization experiments, crystals are seen coming down from the 'boat' almost immediately after exposure to the sound wave, and all of the formed crystals are small in size (less than a mm). These physical observations are consistent with Viedma's results and show that sound waves perturb the solution in a similar way to the rigorous stirring.

The experimental results for the Petri dish experiments provide a stark contrast to the data from the control experiments. The Petri dish results had an average rotation of $-5.082^{\circ}/\text{g}$ with a standard deviation of $6.379^{\circ}/\text{g}$, while the control experiments had an average rotation of $0.252^{\circ}/\text{g}$ with a standard deviation of $9.872^{\circ}/\text{g}$. The only experimental difference between these data sets is that the Petri dish was continuously open to the atmosphere while the control samples were only open for approximately one minute. The results from the Petri dish experiments is interpreted as meaning 75% of crystals grown through open-air evaporation produces crystals with a negative optical rotation. Interestingly, the control experiments give an almost equal representation of either (+) or (-) crystals, with a possible slight bias toward a positive rotation. It has been commonly accepted that dust in the atmosphere is comprised of chiral substances, and these impurities may be important in the bias toward the formation of the negative rotation crystal.

Conclusion

The above experiments show that the sound wave trials mimic the results of Viedma⁶⁷, which might help in understanding the mechanism that is causing the formation of the enantiomeric excess of the sodium bromate crystals. Likewise, the sound results are able to explain the results from both polarizations of the higher power experiments: the mechanism for the formation of the crystals seems to be the same as that of the sound wave experiments. The lower power (0.5 and 0.9 W) experiments for linearly polarized light show that, although both forms of the crystal are formed readily, which is shown through the large standard deviation, the negative rotation form of the crystal is slightly favored. The results for the right circularly polarized light experiments are harder to explain, and no complete conclusions are reached in this study. It is not understood why the circularly polarized light samples have positive values of rotation that are higher than the control samples, unless statistical error is the underlying cause. Likewise, it is not clearly understood why the Petri dish samples have larger negative value rotations than the control samples, which have a slightly positive value, unless chiral matter in the atmosphere directed the crystals' morphologies.

Chapter V.

Linear and Non-linear Optical Rotation in Sodium Chlorate and Sodium Bromate

Introduction

Optical rotatory dispersion is the physical process in which plane polarized light experiences a rotation through some angle, θ , after passing through a chiral substance. Several origins of chirality exist, but the most prominently recognized is that of molecules having a chiral carbon center. For many systems, chirality originates from the spiral spatial arrangements of atoms. The rotation of plane polarized light has been treated quantum mechanically by many authors. Below, we consider the treatment by Kauzmann et al.⁶⁸.

If a region is free of real charges or currents, Maxwell's equations can be written as

$$\text{div} D = 0 \quad \text{Eq. 1}$$

$$\text{div} B = 0 \quad \text{Eq. 2}$$

$$\text{curl} E = -\frac{1}{c} \frac{\partial}{\partial t} B \quad \text{Eq. 3}$$

$$\text{curl} H = \frac{1}{c} \frac{\partial}{\partial t} D \quad \text{Eq. 4}$$

where c is the speed of light, t is time, D is the electric displacement vector, B is the magnetic field, E is the electric field, and H is the effective magnetic field. For a substance with N_1 molecules per cm^3 ,

$$P = N_1 p \quad \text{Eq. 5}$$

$$M = N_1 m \quad \text{Eq. 6}$$

where P is the electric moment, p is the electric moment per molecule, M is the magnetic moment, and m is the magnetic moment per molecule. Rosenfeld⁶⁹ proved that a

perturbing electromagnetic wave gave the following induced electric and induced magnetic moments in a molecule

$$p_a = \alpha_a E' - \frac{\beta_a}{c} \frac{\partial}{\partial t} H' + \gamma_a H' \quad \text{Eq. 7}$$

$$m_a = \frac{\beta_a}{c} \frac{\partial}{\partial t} E' + \gamma_a E' \quad \text{Eq. 8}$$

where the subscript refers to state a, E' is the effective electric field on the molecule, H' is the effective magnetic field on the molecule, and

$$\alpha_a = \frac{2}{3h} \sum_b \frac{\nu_{ab} |a/p/b|^2}{\nu_{ab}^2 - \nu^2} \quad \text{Eq. 9}$$

$$\beta_a = \frac{c}{3\pi h} \sum_b \frac{\text{Im}\{(a/p/b) \bullet (b/m/a)\}}{\nu_{ab}^2 - \nu^2} \quad \text{Eq. 10}$$

$$\gamma_a = \frac{2}{3h} \sum_b \frac{\nu_{ab} \text{Re}\{(a/p/b) \bullet (b/m/a)\}}{\nu_{ab}^2 - \nu^2} \quad \text{Eq. 11}$$

where α , β , and γ are averaged over all possible orientations. The terms $(a/p/b)$ and $(b/m/a)$ refer to the electric and magnetic matrix components for state a and state b, ν_{ab} is the frequency of a transition from state a to state b, and Im and Re refer to either the imaginary or real components of the matrix terms. γ_a has been shown to give small second order effects⁷⁰ and is typically ignored. The average induced moments are then given by

$$p = \alpha \left(E + \frac{4\pi N_1}{3} p \right) - \frac{\beta}{c} \frac{\partial}{\partial t} H \quad \text{Eq. 12}$$

$$m = \frac{\beta}{c} \frac{\partial}{\partial t} \left(E + \frac{4\pi N_1}{3} p \right) \quad \text{Eq. 13}$$

where α and β are a sum of all possible states multiplied by the probability of that state. α is defined as the polarizability, and β is defined as the molecular rotatory parameter. Using equations 12 and 13, D and B become

$$D = \left(\frac{3 + 8\pi N_1 \alpha}{3 - 4\pi N_1 \alpha} \right) E - \frac{12\pi N_1 \frac{\beta}{c}}{3 - 4\pi N_1 \alpha} \frac{\partial}{\partial t} H \quad \text{Eq. 14}$$

$$B = H + \frac{12\pi N_1 \frac{\beta}{c}}{3 - 4\pi N_1 \alpha} \frac{\partial}{\partial t} E \quad \text{Eq. 15}$$

where the previously defined values remain the same. It can be seen that

$$\frac{\varepsilon - 1}{\varepsilon + 2} = \frac{4\pi N_1 \alpha}{3} \quad \text{Eq. 16}$$

$$g = \frac{4\pi N_1 \beta}{c} * \frac{\varepsilon + 2}{3} \quad \text{Eq. 17}$$

where g is the coefficient term for $\frac{\partial}{\partial t} H$.

For an electromagnetic plane wave moving through a chiral medium, it has been shown⁷⁰ that the index of refraction is different depending upon the polarization

$$n_r = \varepsilon^{\frac{1}{2}} - 2\pi \nu g \quad \text{Eq. 18}$$

$$n_l = \varepsilon^{\frac{1}{2}} + 2\pi \nu g \quad \text{Eq. 19}$$

where n_r and n_l refer to the index of refraction for right and left circularly polarized light respectively. The wavefunction for each polarization can be thought of as

$$\psi_r = \psi_0 + \delta \quad \text{Eq. 20}$$

$$\psi_l = \psi_0 - \delta \quad \text{Eq. 21}$$

where ψ_r and ψ_l are the two respective wavefunctions for right and left circularly polarized light, ψ_0 is the unperturbed wavefunction, and δ is

$$\delta = 4\pi^2 \nu^2 g \frac{z}{c} \quad \text{Eq. 22}$$

where z is the axis of propagation. For δ not equal to zero,

$$\varphi' = \left(\frac{2\pi}{\lambda}\right)^2 c g = \frac{\pi}{\lambda} (n_l - n_r) \quad \text{Eq. 23}$$

where φ' is the rotation in radians per cm, n_l is the index of refraction for left circularly polarized light, and n_r is the index of refraction for right circularly polarized light. The specific rotation, $[\alpha]$ is defined as

$$[\alpha] = \frac{\varphi}{\rho} \quad \text{Eq. 24}$$

where φ is the rotation in degrees per decimeter, and ρ is the density in g/mL.

The above treatment represents a quantum mechanical derivation of optical activity. In principle, a complete knowledge of optical rotation or circular dichroism (preferential absorption of right or left circularly polarized light) is possible, but such knowledge is difficult due to the complexity of explicitly solving for all states in a quantum nature. Rather, three theories regarding optical rotatory power have been proposed: coupled-oscillator theory, polarizability theory, and one electron theory. Each of the theories will be treated below.

The coupled oscillator theory was proposed by Born⁷¹, Oseen⁵¹, and Kuhn⁵³; the theory was originally proposed via classical terms, it has since been shown from quantum mechanical considerations to follow from the previous treatment. In essence this method considers two masses, m_1 and m_2 , with charges e_1 and e_2 and vibrating perpendicular to each other with frequencies ν_1' and ν_2' , separated by an equilibrium distance d . If the potential energy coupling the oscillators is of the form

$$V = \frac{1}{2}k_1x_1^2 + \frac{1}{2}k_2x_2^2 + \frac{1}{2}k_{12}x_1x_2 \quad \text{Eq. 25}$$

with k_n being the force constant for that oscillatory motion, the resulting motions are easily separated into normal modes through a rotation of the original axes by the angle a . The normal frequencies will then be shifted slightly to ν_1 and ν_2 . Assuming a random orientation of N_1 molecules per cm^3 , the optical rotation is given by

$$\alpha = \frac{2\pi N_1}{3} \frac{n^2 + 2}{3} \frac{d}{\lambda^2} \sin a \cos a \frac{e_1 e_2}{(m_1 m_2)^{\frac{1}{2}}} \left\{ \frac{1}{\nu_1^2 - \nu^2} - \frac{1}{\nu_2^2 - \nu^2} \right\} \quad \text{Eq. 26}$$

The polarizability theory was originally developed by Kirkwood⁵⁵ after transforming the general form from Eq. 23 to a form containing polarizabilities and anisotropies of functional groups within the molecule. The main premise of this formulation of optical rotatory power relies upon an electron being ‘assigned’ to a specific functional group without moving to another functional group; another premise that builds upon this first assumption is that each electronic transition is localized within

a specific chromophore. The assumption that electrons are associated exclusively with one functional group of the molecule allows the electric and magnetic moments to be written as

$$P_{ab} = \sum_k P_{ab}^{(k)} \quad \text{Eq. 27}$$

$$m_{ab} = \sum_K (R_k \times P_{ba}^{(k)} + \frac{2mc}{e} m_{ba}^{(k)}) \quad \text{Eq. 28}$$

where k denotes the kth group, R_k is the radius vector of the center of mass for the kth group relative to a fixed point, $P^{(k)}$ is the total electronic momentum operator of group k, $p^{(k)}$ is the electric moment operator of group k, $m^{(k)}$ is the magnetic moment operator for group k, m is the mass of the group, e is the charge of the electron, and b and a denote electronic states for the kth group. Referring back to Equation 23, β becomes

$$\beta = \frac{c}{3\pi\hbar} \sum_{a,b} \{ e^{\frac{-\varepsilon\alpha}{kT}} \frac{\text{Im}(p_{ab} \bullet m_{ba})}{\nu_{ba}^2 - \nu^2} \} = \beta^{(0)} + \beta^{(1)} + \sum_k \beta_k \quad \text{Eq. 29}$$

where h is Planck's constant, ε is the dielectric constant of the medium, α is the polarizability, k is Boltzmann's constant, T is the temperature, and the β terms are give by

$$\beta^{(0)} = \frac{1}{3h} \sum_{i>k} \sum_a e^{\frac{-\varepsilon\alpha}{kT}} \sum_{b>a} \frac{\nu_{ba}}{\nu_{ba}^2 - \nu^2} \text{Re}(R_{ik} \bullet * p_{ab}^{(i)} \times p_{ba}^{(k)}) \quad \text{Eq. 30}$$

$$\beta^{(1)} = \frac{c}{3\pi\hbar} \sum_{i>k} \sum_a e^{\frac{-\varepsilon\alpha}{kT}} \sum_{b>a} \frac{\text{Im}(p_{ab}^{(k)} \bullet m_{ba}^{(i)})}{\nu_{ba}^2 - \nu^2} \quad \text{Eq. 31}$$

$$\beta_k = \frac{c}{3\pi\hbar} \sum_k \sum_a e^{\frac{-\varepsilon\alpha}{kT}} \sum_{b>a} \frac{\text{Im}(p_{ab}^{(k)} \bullet m_{ba}^{(k)})}{\nu_{ba}^2 - \nu^2} \quad \text{Eq. 32}$$

where R_{ik} is the distance vector from the center of gravity i to that of k. β_k is typically assumed to be negligible for symmetric groups. $\beta^{(1)}$ is the contribution resulting from the coupling of the magnetic moment on one chromophore to the electric moment on another chromophore. This contribution to β is typically assumed to be small, though in certain circumstances it does become a non-negligible contributor. $\beta^{(0)}$ is the main contributor to the optical rotatory power and is similar in origin to the coupled oscillator theory.

The approximation that all electronic transitions are defined to a specific group allows for the calculation of $\beta^{(0)}$. Perturbation theory is applied using the potential V

$$V = \frac{P_i P_j}{R_{ij}^3} (\cos \theta - 3 \cos \chi \cos \psi) \quad \text{Eq. 33}$$

where p_i and p_j are two dipoles separated by a distance R_{ij} , χ is the angle between p_i and R_{ij} , ψ is the angle between p_j and R_{ij} , and θ is the angle between the two dipoles. The calculation of eigenfunctions using this potential will allow for the calculation of $p_{ba}^{(k)}$, which in will then allow for substituting the dot and cross product terms in Eq. 30 with terms involving polarizabilities, anisotropies, and orientations relative to axes i and k. The final expression for $\beta^{(0)}$ by Kirkwood is

$$\beta^{(0)} = -\frac{1}{6} \sum_{i>k} \sum_{r,s} \alpha_{rr}^{(i)} \alpha_{ss}^{(k)} (b_r^{(i)} \bullet T_{ik} \bullet b_s^{(k)}) R_{ik} \bullet (b_r^{(i)} \times b_s^{(k)}) \quad \text{Eq. 34}$$

where $\alpha_{rr}^{(i)}$ are the polarizabilities along the principal axes $b_r^{(i)}$ of group i, with similar notation for the other groups' polarizabilities, and T_{ik} is

$$T_{ik} = \frac{1}{R_{ik}^3} (1 - 3 \frac{R_{ik} R_{ik}}{R_{ik}^2}) \quad \text{Eq. 35}$$

Though the polarizability treatment is somewhat easier to manipulate, the approximations make it inadequate in various scenarios, particularly with weak absorption bands⁷². For molecules with weak absorption bands that contribute to the optical rotation, it is probable that $\beta^{(1)}$ and $\beta^{(k)}$ contribute to β . Another inadequacy of the polarizability theory is the assumed potential. Equation 33 is only valid for dipoles separated by distances that are large when compared to the charge separation within the dipoles. For excited states, the distances begin to overlap between groups, thereby nullifying the use of the potential V in Eq. 33.

The one electron theory of optical activity relies upon the optical rotation of materials in the visible and ultra-violet portion of the electromagnetic spectrum resulting from electronic transitions. Due to this fact, any theory attempting to describe optical rotation must contain electronic transitions as a central feature, and the one electron

theory accounts for electronic transitions exclusively. The eigenfunctions for two states of a chromophore using perturbation theory are given by

$$\psi_a = \psi_a^0 + \sum_{i \neq a} c_{ia} \psi_i^0 \quad \text{Eq. 36}$$

$$\psi_b = \psi_b^0 + \sum_{j \neq b} c_{jb} \psi_j^0 \quad \text{Eq. 37}$$

where ψ_a^0 and ψ_b^0 are the unperturbed wave functions for state a and b and c_{ia} and c_{jb} are given by

$$c_{ia} = \frac{\int \psi_i^0 V \psi_a^0 d\tau}{E_a^0 - E_i^0} \quad \text{Eq. 38}$$

$$c_{jb} = \frac{\int \psi_j^0 V \psi_b^0 d\tau}{E_b^0 - E_j^0} \quad \text{Eq. 39}$$

Using these new wavefunctions, the rotatory strength is given as

$$R_{ba} = p_{ab} \bullet m_{ba} + \sum_i c_{ia} (p_{ib} \bullet m_{ba} + p_{ab} \bullet m_{bi}) + \sum_j c_{jb} (p_{aj} \bullet m_{ba} + p_{ab} \bullet m_{ja}) + \\ \sum (\text{terms involving products of two } c\text{'s}) + \dots \quad \text{Eq. 40}$$

where

$$p_{ab} = \int \psi_a^0 p \psi_b^0 d\tau \quad \text{Eq. 41}$$

$$p_{ai} = \int \psi_a^0 p \psi_i^0 d\tau \quad \text{Eq. 42}$$

$$m_{ab} = \int \psi_a^0 m \psi_b^0 d\tau \quad \text{Eq. 43}$$

and similar notation for the other electric and magnetic components. For the unperturbed states, generally it is assumed that there is no optically active transition, therefore,

$p_{ab} \bullet m_{ba}$ is taken to be zero. Most of the $p \bullet m$ terms are sufficiently small such as to be considered negligible. Thus, only a small number of c_{ia} and c_{jb} terms need to be calculated. The first summation in Equation 40 gives first order contributions to the optical activity, and the following summations give the higher order effects, though they are typically smaller in magnitude than the first order effects since interactions between the groups are small. Similarly, as the distance between functional groups and the chiral center increases, the contributions from the functional groups become decreasingly

important. Through the perturbative treatment, two main questions arise: what wavefunction should be used to describe the unperturbed state and what forces perturb the ground states? To answer the first question regarding appropriate wavefunctions, any linear combination of wavefunctions in practice is appropriate, but generally the hydrogen-like orbital functions are used for simplicity.

Proper treatment of the potential perturbing the ground state is more complicated; the perturbing potential is generally divided into force fields composed of dipole forces, ionic forces, electronic cloud overlap forces, exchange repulsion forces, and van der Waals' forces. The c_{ia} component by one of the forces, V_j , includes the calculation of

$$\int \psi_i^0 V_j \psi_a^0 d\tau \quad \text{Eq. 44}$$

Dipolar forces may be treated as either a physical separation of charges, or the use of an expression considering an electron in a dipolar field, μ , that makes an angle θ with length R may be used to calculate

$$V = \frac{\mu e}{R^2} \cos \theta \quad \text{Eq. 45}$$

where e is the charge of an electron. Previous work⁷³ has shown that dipolar forces are mainly responsible for the observed optical rotation in phenylmethylcarbinol nitrite, but the same work showed that dipolar forces are not mainly responsible for the observed rotation in *sec*-butyl alcohol. Fields of ions and ionic charges are typically of the form

$$V = \frac{Ze^2}{DR} \quad \text{Eq. 46}$$

where Ze is the ionic charge, D is the dielectric constant of the medium and R is the length away from the potential. The specific form for potentials arising from electronic cloud overlap, exchange repulsion forces, and van der Waals interactions vary with the method of treatment. As can be seen, the ability to accurately define the potential field experienced by the excited electron limits the accuracy to which the optical activity can be calculated.

The preceding treatment considers only one photon optical activity (optical activity at low light intensities); at higher light intensities, it is possible for spectroscopic events to occur through the interaction of multiple photons. Several models exist for the

description of multiphoton circular dichroism^{74, 75, 76} though only one model has been published with an attempt at forecasting nonlinear optical rotatory dispersion⁷⁷. Briefly, the theory of multiphoton circular dichroism will be reviewed before proceeding to the theoretical model for multiphoton ORD.

One photon circular dichroism is described by

$$\varepsilon_L(\nu) - \varepsilon_R(\nu) = 4A \text{Im} \mu_{0f} \bullet m_{f0} \quad \text{Eq.47}$$

where

$$A = \frac{8\pi^3 \nu g(\nu)}{6.909hc} \quad \text{Eq. 48}$$

and ε is the extinction coefficient at a particular frequency ν , μ_{0f} is the electric dipole transition moment, m_{f0} is the magnetic dipole transition moment, and $g(\nu)$ is the normalized line shape. In the description of two photon circular dichroism, we consider the function describing two photon absorption coefficient⁷⁸

$$\delta = B |\lambda \bullet T_{0f} \bullet \mu|^2 \quad \text{Eq. 49}$$

where λ and μ denote the polarization of the two photons, T_{0f} is the absorption probability tensor, and B is given by

$$B = \left(\frac{e}{m}\right)^4 \left(\frac{1}{hc}\right)^2 \frac{g(\nu_\lambda + \nu_\mu)}{\nu_\lambda \nu_\mu} \quad \text{Eq. 50}$$

where ν_λ and ν_μ are the frequencies of the photons with labeled polarizations, $g(\nu_\lambda + \nu_\mu)$ is the normalized line shape, e is the charge of an electron, and m is the mass of an electron. The multi-photon CD is defined as the difference in two photon absorption for left, δ_L , and right, δ_R , circularly polarized light, i.e.

$$\delta_L - \delta_R = B [|\lambda \bullet T_{0f} \bullet \mu|^2 - |\lambda^* \bullet T_{0f} \bullet \mu^*|^2] \quad \text{Eq. 51}$$

where either λ or μ (or both) specify a left circularly polarized photon and refer to the polarization and direction of the photons. In general, the multi-photon CD can be written as¹²

$$\delta_L - \delta_R = [(2\pi)^4 \nu^2 g(2\nu)/(hc)^2] \left(\frac{4}{15}\right) [b_1 \alpha_{0f}^{\mu m} : \alpha_{0f}^{\mu \mu} + b_2 \left(\frac{\pi \nu}{c}\right) \alpha_{0f}^{\mu Q} : \alpha_{0f}^{\mu \mu} + b_3 \alpha_{0f}^{\mu m} : \alpha_{0f}^{\mu \mu}] \quad \text{Eq.52}$$

where the b coefficients depend upon the polarization and propagation of the photons, and the α terms are three polarizabilities resulting from electric dipole, magnetic dipole, and quadrupole interactions.

Evans⁷⁷ uses group theoretical statistical mechanics to explore theoretical components that would describe nonlinear optical rotatory dispersion. The conclusion of his derivation is that the use of intense plane polarized light will result in optical rotation stemming from the molecular property tensor β_4 given by

$$\beta_4 = \left(\frac{\partial^3 E}{\partial B \partial B \partial B} \right)_{00} \quad \text{Eq. 53}$$

where E and B are the electric and magnetic components of the electromagnetic field.

Since Evans' publication, two groups^{79, 80} have published reports of having observed multi-photon effects on optical rotation. Gedanken and Tamir⁷⁹ reported the observation of multi-photon ORD at 456 nm in aqueous solutions of camphorsulfonic acid (CSA). The results of the study are mildly inconclusive, but it appears that the optical rotation of +CSA increases with increasing laser intensity. Cameron and Tabisz⁸⁰ investigated the effects of laser intensity on the optical rotation of uridine, sucrose, and borneol. Their results are more unreliable than the previously published Gedanken results since the spread of the data points is so large. The experimental observations at 308 nm for aqueous solutions of uridine are that the optical rotation decreases as a function of increasing power. An initial survey of a previously published ORD curve⁸¹ for uridine seem to indicate that the optical rotation at 154 nm ($\lambda=308/2$ nm) is negative, thus indicating the possibility that the increased intensity gives rise to a contribution to the optical rotation from $\lambda/2$.

As stated in a previous chapter, crystals of sodium chlorate and sodium bromate crystallize into the same space group, $P2_13$. Interestingly, when each crystal has the same configuration, they rotate the plane of polarization of linearly polarized light in opposite directions. Chandrasekhar and Madhava⁵⁹ have extensively studied the ORD curve for sodium chlorate in the visible and ultra-violet region of the electromagnetic spectrum; the following formula was postulated to give a good fit to the experimental data for measured ρ , °/mm of crystal

$$\rho = \frac{1.2528}{(\lambda^2 - (0.10)^2)} - \frac{0.1546}{(\lambda^2 - (0.21)^2)} \quad \text{Eq. 54}$$

where λ is the wavelength in microns. Equation 54 is of the Cauchy form containing two terms to account for characteristic absorbances at 100 and 210 nm. The reported error for the fit to experimental data is ~2.2%, except at 623 nm, where the reported error is 2.9%. Einhorn et al.⁸² later published work for the far UV ORD of sodium chlorate and refined the predicted absorbance at 210 nm to 214.5 nm. Kizel et al.⁸³ published a similar equation for the same conformation of sodium bromate:

$$\rho = \frac{1.449}{(\lambda^2 - (0.1)^2)} - \frac{1.887}{(\lambda^2 - (0.224)^2)} \quad \text{Eq. 55}$$

where ρ is again measured in °/mm, and the characteristic absorbances for sodium bromate are 100 and 224 nm. The reported error for this data fit is a deviation of ~2%.

Experiments will be described that confirm the one photon ORD curve for the visible and some ultra-violet regions for sodium chlorate and sodium bromate crystals. Further, studies will show the effects of non-linear optical rotatory dispersion in sodium chlorate and sodium bromate at 532 and 355 nm.

Experimental

The optical rotation of crystalline sodium chlorate and sodium bromate were measured using a Continuum OPO laser $\lambda=700\text{-}475$ nm and using the fundamental and harmonics of a Quanta Ray DCR Nd:YAG laser (pulse width 7 ns). Figure 1 gives a schematic of the experimental setup. In essence, the laser serves as the monochromatic light source, and the polarization of the beam is insured using a Glan-air prism. The light then passes through the crystal before passing through the polarizer serving as the analyzer. The detector was either an Ophir AN/2 power meter or a ThorLabs photodiode. The linear ORD studies utilized the OPO laser with a frequency of 10 Hz; the non-linear ORD studies utilized the Quanta Ray DCR Nd:YAG second ($\lambda=532$ nm) and third ($\lambda=355$ nm) harmonics.

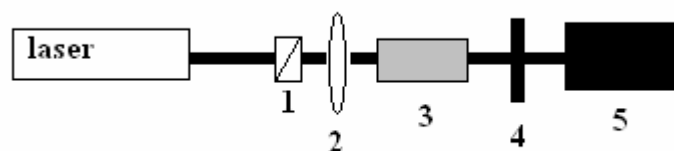


Figure 1. Schematic diagram for optical rotation measurements. (1) Glan-air prism (2) 13 cm focal length lens (3) crystal sample (4) polarizer (5) detector

For each measurement, the minimums and maximums (2 each) relative to the detector signal were found as a function of the angle of the polarizer; these values served as the reference point for the samples. For the same corresponding laser power, the optical rotation of the crystals was measured; typically measurements corresponding to two full revolutions of the polarizer were made ($2 \times 360^\circ$ revolutions). For the blank and crystal data sets, the minimums and maximums were found by fitting the data to a quadratic equation and solving for the angle of the polarizer for either the minimum or maximum signal at the detector. The optical rotation was defined as the difference between the blank and the crystal for the corresponding minimum and maximum angle of the polarizer. After the observed rotation surpassed 90° , either shorter pathlengths or extrapolation were necessary for the correct assignment of the rotations. Only one sodium chlorate crystal was used, and it had a length of 12.24 mm. Two sodium bromate crystals were utilized; one with a length 19.58 mm, and the other with a length of 3.05 mm.

Results and Discussion

The results for the linear optical rotation for sodium chlorate and sodium bromate are tabulated in Table 1. The experimental values fit well with previously obtained experimental optical rotation curves. Experimental attempts were made to measure the optical rotation for sodium bromate at 266 nm, but the quality of the laser beam after passing through the crystal made all attempts to make measurements impossible. For the better portion of the data, the experimental values agree well with previously obtained experimental data; the only discrepancies between the series of data are at the lower wavelengths for sodium bromate. Figure 2 gives a graphical representation of the experimental data and the relative behavior of the previously obtained experimental data. The results for the power dependent studies of optical rotation for sodium chlorate and sodium bromate are seen in Tables 2 and 3. The data in Table 2 was obtained at 532 nm, and data in Table 3 shows the power dependence at 355 nm.

Table 1. Results for linear optical rotatory dispersion curve for sodium chlorate and sodium bromate crystals. Units are degrees per mm. The calculated column refers to the predicted values following from the statistical fit via Eq. 54 and 55 respectively.

	NaClO ₃		NaBrO ₃	
λ (μm)	Calc.	Exp.	Calc.	Exp.
0.700	2.17	2.49	1.34	0.26
0.675	2.34	2.37	1.47	1.94
0.650	2.54	2.31	1.61	1.88
0.625	2.76	2.83	1.79	2.35
0.600	3.01	3.15	2.00	2.12
0.575	3.30	3.36	2.25	2.46
0.550	3.63	3.43	2.56	2.5
0.532	3.89	3.59	2.82	2.79
0.525	4.00	4.04	2.94	2.83
0.500	4.44	4.63	3.42	3.18
0.475	4.94	5.44	4.04	4.16
0.355	9.06	9.29	12.38	12.06
0.266	15.00	15.08	67.34	-----

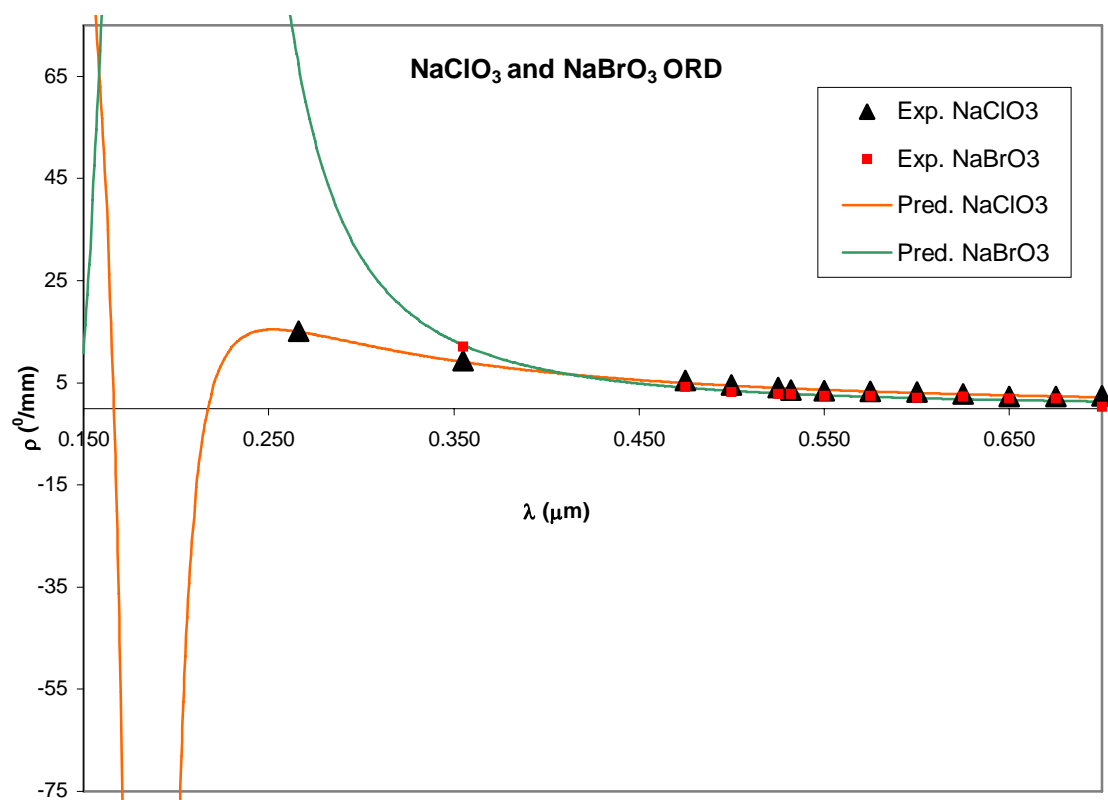


Figure 2. Graphical depiction of experimental results for one-photon ORD of sodium chlorate and sodium bromate and predicted (Eq. 54 and 55) values.

Table 2 (a) Results for the power dependent optical rotations of NaClO_3 at 532 nm. Units of results are degrees/mm. (b) Results for power dependent optical rotations of sodium bromate at 532 nm. Units are in degrees/mm. The listed intensity is the peak power density. Error bars are the standard deviations from multiple measurements.

(a)

Intensity (W/cm^2)	Log (Intensity)	NaClO_3 ($^\circ/\text{mm}$)
6.34E+06	6.802	3.59 +/- 0.36
1.27E+07	7.104	3.89 +/- 0.05
1.99E+07	7.299	3.92 +/- 0.05
5.41E+10	10.733	3.98 +/- 0.23
1.08E+11	11.033	4.00 +/- 0.15
1.69E+11	11.228	3.91 +/- 0.29

(b)

Intensity (W/cm^2)	Log (Intensity)	NaBrO_3 ($^\circ/\text{mm}$)
6.34E+06	6.802	2.79 +/- 0.13
1.27E+07	7.104	2.79 +/- 0.07
1.99E+07	7.299	2.79 +/- 0.05
5.41E+10	10.733	2.97 +/- 0.22
1.08E+11	11.033	2.81 +/- 0.04
1.69E+11	11.228	2.74 +/- 0.26

Table 3 (a) Results for power dependent optical rotations of NaClO₃ at 355 nm. Units of results are degrees/mm. (b) Results for power dependent optical rotations for NaBrO₃ at 355 nm. Units are in degrees/mm. The listed intensity is the peak power density.

Error bars are the standard deviation from multiple measurements.

(a)

Intensity (W/cm ²)	Log (Intensity)	NaClO ₃ (°/mm)
4.06E+06	6.609	9.37 +/- 0.50
7.14E+06	6.854	8.92 +/- 0.05
7.94E+06	6.900	8.95 +/- 0.19
6.76E+10	10.830	9.04 +/- 0.10
9.60E+10	10.982	8.69 +/- 0.94
1.08E+11	11.033	8.84 +/- 0.66

(b)

Intensity (W/cm ²)	Log (Intensity)	NaBrO ₃ (°/mm)
9.52E+06	6.979	12.06 +/- 1.17
1.27E+07	7.104	12.53 +/- 0.71
1.59E+07	7.201	11.55 +/- 1.90
2.22E+07	7.346	9.22 +/- 1.29

Looking initially at the power dependent rotations for sodium chlorate at 532 nm, the rotations are seen to increase as the power increases, before reaching a plateau, or saturation point. This effect is not unexpected since it could be thought that a finite number of crystal lattice points are interacting with the incoming photons. Eventually, a point is reached where the number of affected crystal lattice sites interacting with incoming photons has been maximized, and the observed rotation can no longer be affected. For sodium bromate at 532 nm, a similar relationship applies, though it is not as obvious an example as sodium chlorate data. Interestingly, the optical rotations of sodium chlorate at 355 nm shows that the optical rotation of the crystal goes down as the intensity increases (conversely, experimental evidence initially appears that the optical rotation increases as the power increases, though the latter data points seem to dispute that claim). The latter data points of the 355 nm power dependent studies of sodium bromate will be discussed later.

An explanation of the non-linear optical rotations can be thought of as a 2 photon system where the first photon exhibits the traditionally observed optical rotation. Referring back to Eq. 30, the optical rotation is determined by the frequency of the incoming photon (with inclusion of the effects of all summed excited states), and with a high enough intensity, the second photon may further rotate the plane polarized light by a contribution from what the effects of $2\nu_1$ would be. Figure 3 shows schematically what is being described.

Taking the NaClO_3 data for 532 nm, the one photon optical rotation is observed to be $3.59^\circ/\text{mm}$, and a higher intensity of 532 nm light slightly increases the observed rotation to plateau value of $\sim 4.00^\circ/\text{mm}$. The observed one photon optical rotation at 266 nm is $15.08^\circ/\text{mm}$ for sodium chlorate. One may represent the power dependent ORD as

$$\rho_{\text{exp}} = \rho^1 + f(I)\rho^2 + \dots \quad \text{Eq. 56}$$

where ρ_{exp} is the experimentally observed optical rotation, ρ^1 is the one photon optical rotation, $f(I)$ is a function of intensity that relates the contribution of ρ^2 , the optical rotation at $2\nu_1$. It can be imagined theoretically to have higher order terms when higher order contributions are included. For the example of the 532 nm data for sodium

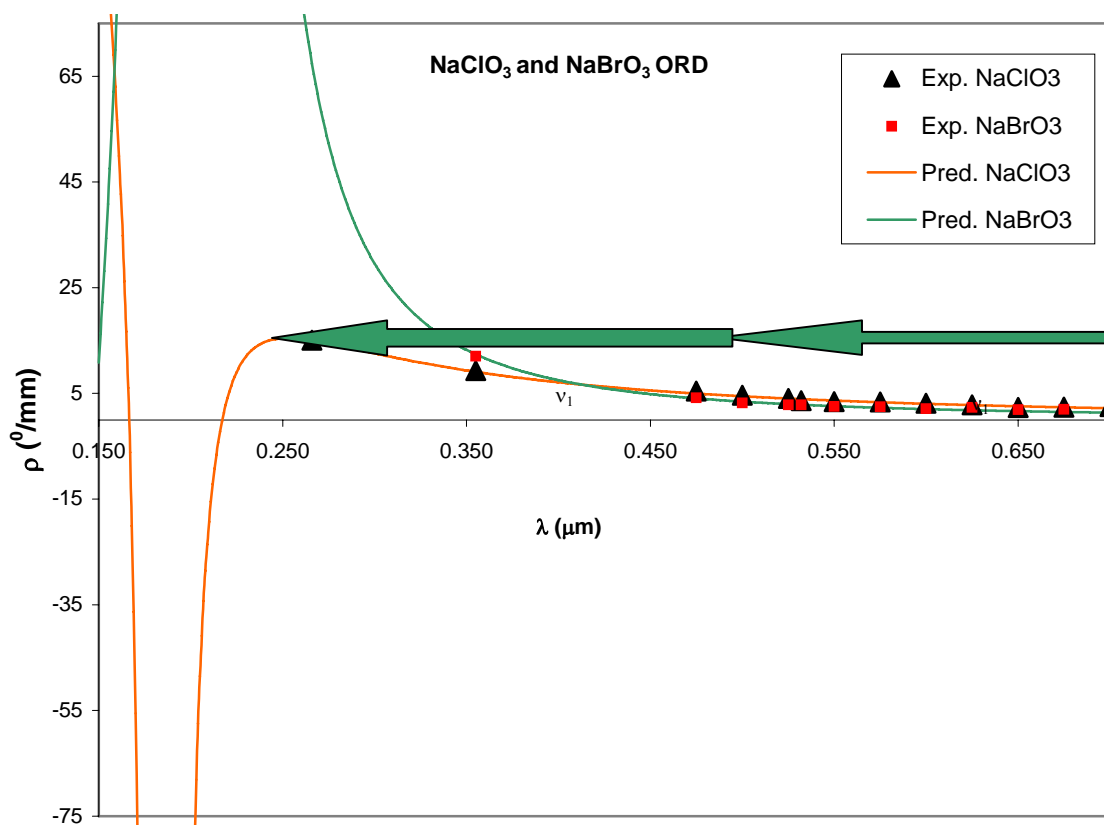


Figure 3. Graphical interpretation for the non-linear optical rotation. A photon of frequency, ν_1 , gives the traditionally observed one photon optical rotation; when the intensity of radiation is high enough (has reached a critical threshold) a second photon contributes an effect that would be equivalent to the one photon observed rotation for $2 \nu_1$.

chlorate, the $2\nu_1$ contribution to the optical rotation is $\sim 2.72\%$ at a peak power density of $1.08 \times 10^{11} \text{ W/cm}^2$, or $f(I)$ is equal to 0.0272 at $1.08 \times 10^{11} \text{ W/cm}^2$. Figure 4 takes the data for sodium chlorate from Table 2 and calculates the percentage of contribution that ρ_{266} makes to the observed optical rotation. Initially, a relationship between the log of the intensity and the 266 nm contribution appears, but $f(I)$ is expected to be a function with a threshold intensity needed before two photon effects appear.

Further experimental evidence for an equation of the form of Eq. 56 is seen in the 532 nm sodium bromate data and the 355 nm data for sodium chlorate (sodium bromate will be addressed to show that it may too be consistent). Looking at the intensity studies for sodium bromate at 532 nm, $\sim 7\%$ increase in the optical rotation is seen as the optical rotation increases from 2.79 to $\sim 3.00^\circ/\text{mm}$. Since an experimental value for the optical rotation at 266 nm for sodium bromate was not measured, the predicted value from past data is $67.37^\circ/\text{mm}$. The latter data points at high power indicate that the contribution threshold has probably been reached at a power density of $5.41 \times 10^{10} \text{ W/cm}^2$, but nevertheless, a slight increase of the optical rotation is observed with increasing power, which follows the prediction from Eq. 56. The optical rotation of sodium chlorate at 355 nm decreases with increasing power, and the predicted optical rotation (albeit a theoretical modeling of experimental data that does not extend to that range) is $\rho_{178} \sim -500^\circ/\text{mm}$, which would explain the decrease of the optical rotation with an increase in power. The example of sodium bromate at 532 nm and sodium chlorate at 355 nm shows that the contribution of $\rho_{2\nu_1}$ is small and apparently a function of the frequency of light (i.e. $f(I)=f(I,\nu)$) as expected.

The power dependent studies for sodium bromate at 355 nm were restricted to the use of a crystal with a length of 3.05 mm; initial attempts were made with the crystal with a length of 19.58 mm, but results were difficult to interpret with a projected observed rotation of approximately 230 degrees, thus the change to the shorter crystal. Likewise, during the attempts to measure the rotation with the longer crystal, damage occurred at the surface of the crystal, thus rendering it essentially useless for future measurements.

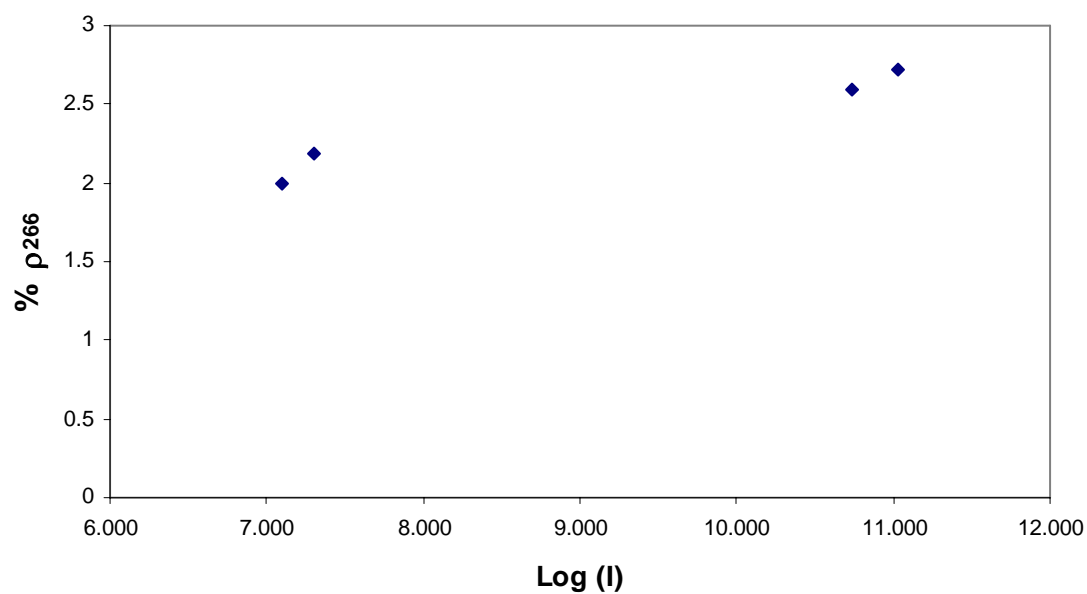


Figure 4. Contribution of ρ_{266} from the data from table 2(a) is plotted versus the logarithm of the intensity for data from sodium chlorate at 532 nm.

Results for the sodium bromate crystal with a length of 3.08 mm were interpretable, but using a lens to focus the beam to increase the power density was not possible without damaging the crystal. From the experimental evidence for sodium bromate at 355 nm, it is not entirely conclusive, but coupled with the data for sodium chlorate at 532 and 355 nm and sodium bromate at 532 nm, it is expected that the initially observed trend that the optical rotation increases with increasing power is correct.

Earlier work investigated the effects of power on the optical rotations of CSA⁷⁹ and uridine (among other molecules)⁸⁰; those results appear to be consistent with the present results. Specifically, uridine is known to have a positive optical rotation at 308 nm; the power dependent studies of Cameron⁸⁰ show that as the power increases, the optical rotation decreases slightly. Previous studies⁸¹ have shown that the low wavelength optical rotation of uridine is negative, thus the second photon would give a negative contribution to the optical rotation. It should be noted that the previous studies regarding NL-ORD did not propose a mechanism that would explain the observed phenomena; this study has a proposed hypothesis. From experimental evidence for sodium chlorate, sodium bromate, and prior work with uridine, the observed multi-photon optical rotation is proposed to be of the form of equation 56. Specifically, it is suggested that the power dependent optical rotation depends upon the sign of the optical rotation at the n-photon region. This particular technique is a means to probing far UV regions of optical activity to learn about the qualitative behavior of the optical rotation.

Conclusion

Optical rotation is known to be a frequency dependent property, but it is observed in sodium chlorate and sodium bromate crystals that at high enough power densities, multiple photon processes contribute to the observed rotation. A relationship of the form of equation 56 is postulated as the form for the contribution of multiple photons to the optical rotation. It is not clear whether the experimental results can be expected by Evans' theory⁷⁷. The results from sodium chlorate and sodium bromate do indicate that

the observed optical rotation is dependent upon the sign of the optical rotation in the n-photon region.

Chapter VI.

Speed of Sound in Racemic and Optically Pure α -Methylbenzylamine

Introduction

Measurements of the speed of sound in liquids provide important information on their thermodynamic properties and structure. Formally, the speed of sound, u is related to the isentropic compressibility, β , through

$$\beta = -\frac{1}{V} \left(\frac{\partial V}{\partial P} \right)_S = \frac{1}{\rho u^2} \quad \text{Eq. 1}$$

where V , P , S , and ρ represent the volume, pressure, entropy, and density of the liquid. The isentropic compressibility, K_T , is related to the isothermal compressibility through

$$K_T = \beta + \alpha^2 T \frac{V_m}{C_{p,m}} \quad \text{Eq. 2}$$

where α is the isobaric expansivity, V_m is the molar volume, T is temperature, and $C_{p,m}$ is the molar heat capacity at constant pressure. Knowledge of V and P defines the compressibility of the fluid. The use of sound velocities in liquids have been used to study physiochemical and molecular interactions in numerous fluids and mixtures.

Previously, the pulse-echo-overlap (PEO)^{84, 85} method was used to determine the speed of sound in liquids. The PEO method can operate in multiple-echo or in through-transmission mode, both with either broadband or r.f. pulses. In short, the apparatus emits an acoustic wave of known frequency into the sample, which is then reflected back to the point of generation. The transit time of the pulse is recorded with an oscilloscope, and the distance of transit is known, and the velocity can be determined via

$$u = \frac{d}{\Delta t} \quad \text{Eq. 3}$$

where d is the distance the sound wave travels, and Δt is the transit time for the sound wave. This reflected sound wave will continue to ‘echo’ until the sound wave dies out, at

which time, a new sound wave is re-emitted to overlap with the time position of the previous acoustic wave. With correct echo-overlapping, a speed of sound with a very high precision is obtained. This method typically relies upon the calibration of the system with distilled water, but is capable of measuring frequency dependent sound velocity data.

This method of measuring the speed of sound in liquids has been used in many applications and varied to meet those applications, and a few will be mentioned briefly. Tardajos et al.⁸⁶ utilized a variation of the PEO method with broadband pulses in multiple-echo mode to measure the speed of sound in a variety of pure liquid samples. Povey et al.⁸⁷ conducted speed of sound measurements in *n*-alkanes, 1-alcohols, and dimethylsiloxanes using an acoustic wave with a frequency of 2.25 MHz. The measurements were then compared to Schaafs' semi-phenomenological molecular model⁸⁸, and Povey concluded that Schaafs' model was appropriate for linear chain hydrocarbons and silicones. Zak et al.⁸⁹ constructed an apparatus based upon the PEO method principle which allowed for variation of pressure, up to 300 MPa, and temperature. Zak proceeded to measure the speed of sound in *n*-heptane and ethanol as a function of pressure and good agreement was found with previously published collections of pVT data.

In 1941, Schaafs devised a semi-phenomenological molecular model⁸⁸ for the sound velocity in liquids, as shown by Equation 4

$$\nu = \frac{W\rho B}{M} - \frac{W}{\left(1 + \frac{B}{\beta}\right)} \quad \text{Eq. 4}$$

where *W* (m/s) is the ideal sound velocity (within the molecule only), *M* is the molecular weight, *B* is the molecular volume, ρ is the density, and β is the end group volume. *B* is not the molar volume, but rather is an estimate of the volume a molecule occupies without accounting for intermolecular space. This molecular model is applicable for straight chained molecules and was appropriately utilized by Povey⁸⁷ in the analysis of *n*-alkanes and 1-alcohols.

Low frequency vibrational spectroscopy of liquids is a field that is receiving more attention and yields information that is relevant to intermolecular interactions. Treating the molecular liquid as a pseudolattice, the corresponding absorption, ν , for intermolecular vibrations is given by⁹⁰

$$\nu = \frac{1}{2\pi c} \left(\frac{3}{N_1 \bar{M} \beta r^2} \right)^{\frac{1}{2}} \quad \text{Eq. 5}$$

where c is the speed of light, N_1 is the number of molecules per unit volume, \bar{M} is the reduced mass of two molecules, β is the isothermal compressibility, and r is the effective interaction radius. Low frequency absorption has been observed in liquids ranging from carbon disulfide to water; thus, the measurement of low frequency vibrations in liquids is another route to the determination of the compressibility of a liquid. One publication⁹¹ has noted that the effective interaction radius, r , is smaller for associated systems.

Chiral discrimination in α -methylbenzylamine^{92, 93, 94} (MBA), shown in Figure 1, has been studied by several groups. Lepori⁹² reported the excess molar volume, V^E , for a series of enantiomeric liquids mixed with the opposing enantiomer in increasing fashion. For (*S*)-(-)- α -methylbenzylamine, Lepori reported the difference between the partial molar volume of the solute at infinite dilution and molar volume of the pure liquid as $-0.0214 \frac{\text{cm}^3}{\text{mol}}$ at 25 °C when mixed with the (+) form of MBA. Using a statistical treatment for investigating the effect of chiral discrimination on thermodynamic properties¹² of classical, rigid, non-spherical fluids, he showed that differences in the partial molar volume of $\sim 0.05 \frac{\text{cm}^3}{\text{mol}}$ were possible. This particular model considers the discrimination as arising from space-filling differences in pair-wise contact of hard spheres. The magnitudes predicted by the model were consistent with the experimental results, though the sign was not always correct; the model predicted that the partial molar volume of the liquid in itself as a solvent would always have the lower volume.

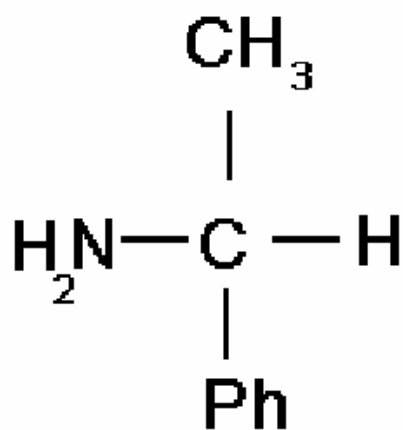


Figure 1. Flat view of (*S*)-α-methylbenzylamine.

Atik⁹³ reported the presence of chiral discrimination in MBA via the excess molar enthalpy as a function of concentration and cited a previous result⁹⁶ for the excess molar volume of MBA as $-0.0018 \pm 0.0004 \frac{\text{cm}^3}{\text{mol}}$ at 30 °C. The deviation from Lepori's published value⁹² of V^E may be a result of the differing temperature for the experiments. Atik⁹⁴ extended his study of chiral discrimination of MBA to the enthalpy of vaporization. For the liquid to gas phase transition of MBA at 25 °C, Atik calculates the chiral discrimination from Eq. 6

$$\left[\Delta_l^s H_m \{ (+) - C_8 H_{11} N \} - \Delta_l^s H_m \{ (\pm) - C_8 H_{11} N \} \right] \approx 0 \quad \text{Eq. 6}$$

Thus Atik concludes that the chiral discrimination for the liquid to gas phase transition is small and consistent with experimental uncertainties.

Jorgensen and Bigot⁹⁷ reported on the pressure dependence of mixing the enantiomeric liquid 1,2-dichloropropane using Monte Carlo simulations in the isothermal, isobaric ensemble. The simulation conditions were 25 °C and pressures from 1 to 5000 atm. The conclusion of this study was that there was no chiral discrimination at 1 atm or 5000 atm, nonetheless, it was possible to theoretically model chiral organic liquids. It should be noted that 1,2-dichloropropane is not capable of forming intermolecular hydrogen bonds while MBA does form hydrogen bonds.

Zingg et al.⁹⁸ reported chiral discrimination in the structure and energetics of the association of stereoisomeric salts of mandelic acid with MBA. This particular study conducted extensive studies using differential scanning calorimetry, enthalpies of solution, enthalpies of dissociation, enthalpies of reaction of mandelic acid with the stereoisomeric base, conductance, ¹H magnetic resonance, and X-ray crystallography. Figures 2 and 3 show the proposed structure for the (*R*)-(+)- α -phenylethylammonium (*S*)-(+)-mandelate ion pair and (*R*)-(+)- α -phenylethylammonium (*R*)-(-)-mandelate ion pair respectively, as produced by Zingg et al.⁹⁸ In the (*R*)-(+)- α -phenylethylammonium (*R*)-(-)-mandelate ion pair, a bidentate, intermolecular hydrogen bond is proposed between the carboxyl and amino group, while in the (*R*)-(+)- α -phenylethylammonium (*S*)-(+)-mandelate ion pair a single hydrogen bond is suggested. The proposed (*R*)-(+)- α -phenylethylammonium (*R*)-(-)-mandelate ion pair is shown in Figure 3 to have a better

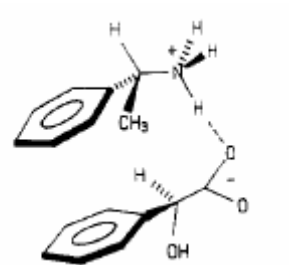


Figure 2. Proposed structure for the (*R*)-(+)- α -phenylethylammonium (*S*)-(+)-mandelate ion pair as produced by Zingg et al.⁹⁸

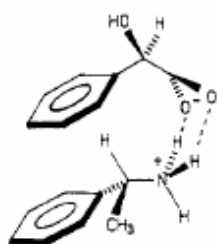


Figure 3. Proposed structure for the (*R*)-(+)- α -phenylethylammonium (*R*)-(-)-mandelate ion pair as produced by Zingg et al.⁹⁸

overlap between the phenyl rings and less steric effects (the base methyl group does not lie over the ring) than the diastereomeric ion pair. Zingg et al. conclude that ion pairing in the (+)/(-) salt system is favored.

The absorption of laser pulses in a liquid is known to create acoustic waves, and the mechanisms for this process are diverse. For an energy density such that the original state of the molecule does not change, the thermal mechanism are known to be the dominant mechanism for the acoustic wave formation. In short, the acoustic waves are generated due to the thermal expansion and collapse of the liquid. Kasoev⁹⁹ and Egerev¹⁰⁰ treated the shape of the acoustic pulse theoretically. Kasoev⁹⁹ concluded that the acoustic pressure generated by lasers is of the form

$$p(x, y, z, t) = \frac{H_0 \beta a^2}{8C_p R \tau_\mu} e^{s^2/4} \left[\exp\left(-\frac{R/(c-t)}{\tau_\mu}\right) \text{Erfc}\left(s/2 - \frac{R/(c-t)}{\tau_a}\right) - \exp\left(\frac{R/(c-t)}{\tau_\mu}\right) \text{Erfc}\left(s/2 + \frac{R/(c-t)}{\tau_a}\right) - \exp\left(-\frac{R/(c-t+\tau)}{\tau_\mu}\right) \text{Erfc}\left(s/2 - \frac{R/(c-t+\tau)}{\tau_a}\right) + \exp\left(\frac{R/(c-t+\tau)}{\tau_\mu}\right) \text{Erfc}\left(s/2 + \frac{R/(c-t+\tau)}{\tau_a}\right) \right] \quad \text{Eq. 7}$$

where $s = \tau_a / \tau_\mu$, $\tau_a = (a \sin \theta) / c$, $\tau_\mu = (\cos \theta) / (\mu c)$, t is the laser pulse width, C_p is the heat capacity at constant pressure, β is the coefficient of expansion, c is the sound velocity, H_0 is the laser intensity, a is the effective radius of the laser beam, t is time, R is the spherical zone of sound generation, and θ is the angle between the z -axis and the direction to the point of observation. These authors were able to accurately model the acoustic pressure levels in water as a function of time, thereby estimating the distribution of acoustic frequencies present.

Using a novel methodology to measure the speed of sound in liquids and low frequency Raman measurements, the compressibility of the racemic and enantiomeric solutions will be examined. Results will be discussed with reference back to the published results of Zingg et al.⁹⁸

Experimental

(*S*)-(-)- α -Methylbenzylamine (Aldrich >98%) and racemic α -methylbenzylamine (Aldrich >99%) were used without further purification. Purity of the samples was checked with a GC/MS, and each of the samples was of similar purity levels (~98%), with the same impurities present in both samples. Impurities were probably the result of extended exposure to carbon dioxide. The apparatus for measuring the speed of sound has been previously published¹⁰¹, but was modified to accommodate the MBA solution. Briefly, the sound pulse in the liquid is generated from the second harmonic of a Quanta-Ray Nd:YAG laser ($\lambda=532$ nm, pulse width ~7 ns) focused with a lens into the solution, and the motion of the sound wave through the solution is monitored by using a He:Ne laser as described below. It was found that the MBA greatly absorbed the sound wave and the focused laser beam could not be employed as the sound source, so a filament of copper wire was placed into the solution, and the laser was focused onto the tip of the filament to produce an intense sound source. The sample cell was approximately 4 cm in length and 1 cm wide with a depth of 4 cm; the cell was mounted on a translation stage. The position of the translation stage could be changed in increments of 0.080 mm. The detector for the sound wave was a Metrologic He:Ne laser beam that was collimated to a diameter of 0.5 mm before passing through the solution and into a photodiode (ThorLabs Model DET1-SI). The photodiode was triggered with the generation of the light source, and the transit time between the generation of the sound wave to the disturbance of the He:Ne beam was monitored as a function of distance with the mobile stage. A schematic of the experimental setup is shown in Figure 4. The time of transit of the sound wave was taken to be the difference between the trigger time and the time at the highest point of the wave pattern. The speed of sound in the liquid is the slope of a best fit line through the plot of the time for the sound wave to travel versus the distance the wave traveled. Attempts to measure the speed of sound with a Nusonics Model 6080 Concentration Analyzer were also made, however, attenuation of the sound wave prevented the use of this method. Attenuation of the sound in the present experiment also affected the quality of data of the present experiment. Using the laser based methodology without the copper

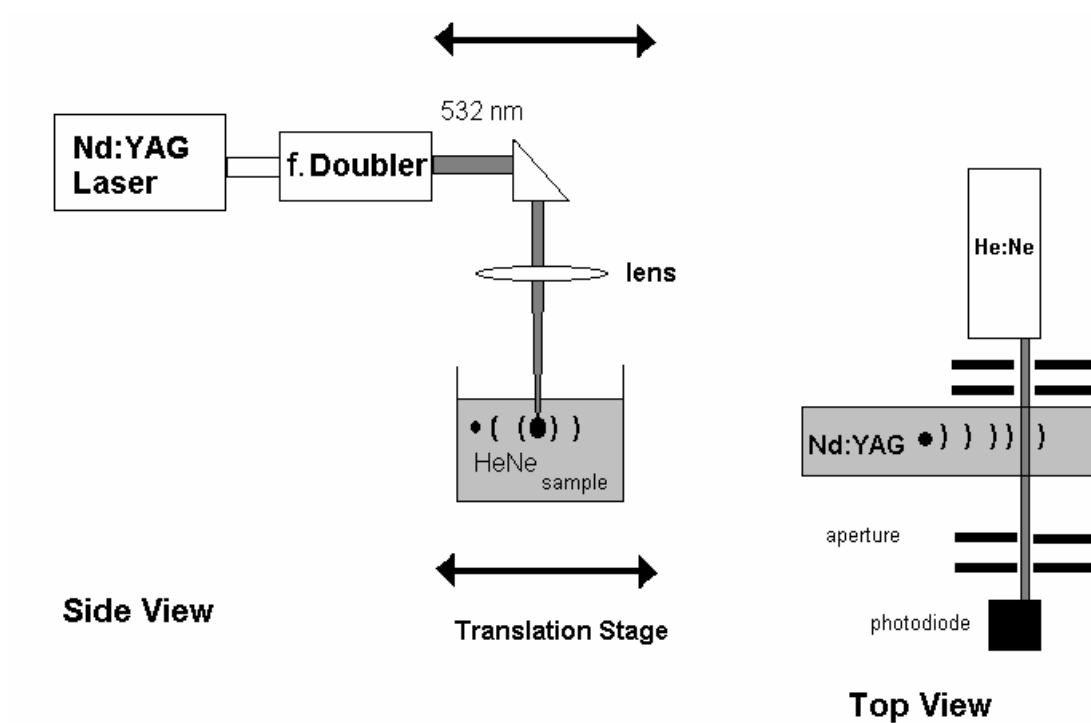


Figure 4. Experimental apparatus used to determine the speed of sound in liquids. The glass cell (4x1x4 cm) and turning prism are mounted on a controlled translation stage. The He:Ne and Nd:YAG positions are fixed. The copper wire is a modification of the method for MBA measurements.

tip, the error of the measurements in aqueous alanine and aqueous solutions was expected to be ~0.5%.

Raman spectra were recorded with a Dilor XY800 Raman spectrometer using an Ar⁺ source ($\lambda=514.5$ nm). Spectra were taken at room temperature and at liquid nitrogen temperature (77 K). The excitation source's power was 500 mW.

Results and Discussion

The results of the speed of sound experiments are seen in Table 1. The data in Table 1 show that the speed of sound in the racemic sample is faster than that for (S)-MBA by approximately 14.4 m/s (or ~1%) with each sample having roughly the same standard deviations. Using Equation 1 and a density of 0.949 g/mL (quoted from Sigma-Aldrich), the racemic and (S)-(-)- α -methylbenzylamine have isentropic compressibilities of $4.660 \pm 0.012 \times 10^{-10} \frac{m^2}{N}$ and $4.748 \pm 0.011 \times 10^{-10} \frac{m^2}{N}$, respectively. Figure 5 shows a typical recorded spectrum from the experimental apparatus; the 'ringing' appearance at the beginning of the data acquisition is a product of the copper wire being used to assist in the generation of the sound wave. The copper wire plays a role in the production of the sound wave, but the sound wave that is monitored is not from the copper wire since the speed of sound from the copper wire would measure ~3800 m/s, whereas, ~1500 m/s is measured. Figure 6 shows the resulting spectrum if the sound generating laser nearly overlaps (<0.080 mm) the He:Ne detection beam on the copper wire. Comparison between Figures 5 and 6 shows that the marked peaks are a result of sound propagation in the MBA sample; other peaks are seen in the spectrum and are probably a result of reflection off of vessel walls.

The low wavenumber Raman spectra of (S)- and racemic MBA at room temperature are shown in Figure 7. The peaks of interest are at 143 cm^{-1} for each sample; the resolution of the spectrometer is not sufficient to distinguish one sample's vibrations from those of the other sample. Assuming equivalent densities and using

Table 1. Results for the individual speed of sound experiments; values are tabulated for both the racemic and (*S*)-(-)- α -methylbenzylamine. All experiments were at 25 ± 1 °C.

<u>Racemic (m/s)</u>		<u>S-(-) (m/s)</u>	
	1499.5		1498.3
	1507.5		1489.7
	1508.6		1491.7
	1507.3		1493.3
	1503.7		1487.8
	1507.3		1492.3
	1504.1		1481.8
	1504.1		1490.7
	1499.9		1489.0
	1507.3		1491.7
	1494.1		1489.1
	1501.0		1485.5
	1505.2		1487.5
	1498.6		1486.3
	1499.1		1488.6
	1506.9		1486.7
	1502.8		1489.7
	1506.0		1491.7
	1506.7		1494.4
<u>Average:</u>	1503.7	<u>Average:</u>	1489.3
<u>Std. Dev.</u>	3.97	<u>Std. Dev.</u>	3.65

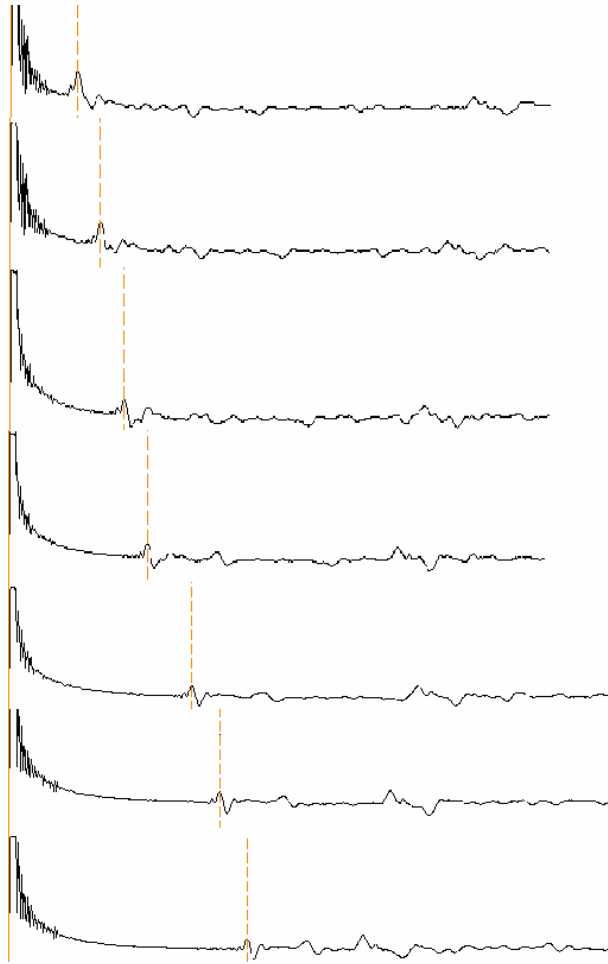


Figure 5. Typical spectra of the speed of sound profile in MBA. The top spectrum represents a distance of 1.250 mm between the two lasers, and each following spectrum has an increasing distance of 0.625 mm. Structures at positions longer than that due to the single pass peak is due to the reflection within the sample container.

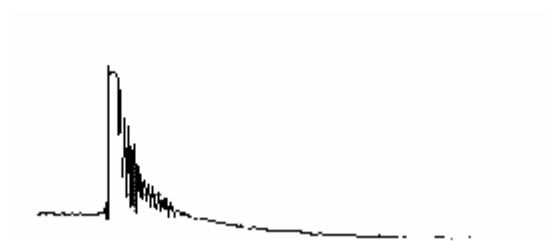


Figure 6. Typical spectrum of nearly overlapping detection He:Ne and sound generating Nd:YAG beams.

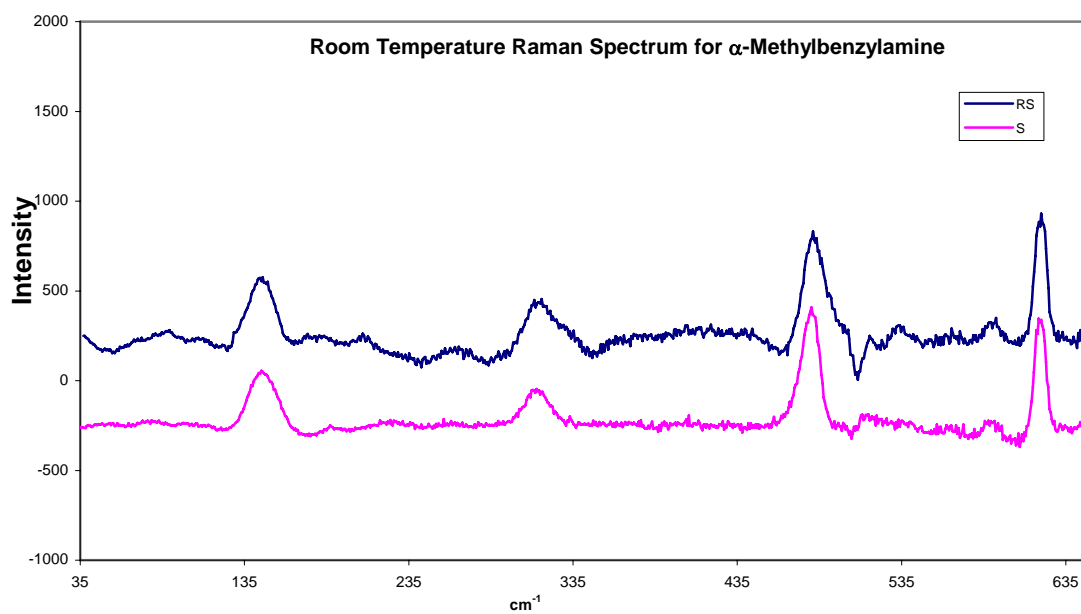


Figure 7. Room temperature low frequency Raman spectrum of (*S*)- and racemic MBA. The peaks at $\sim 143 \text{ cm}^{-1}$ are not separated enough for comparison purposes.

Equation 5 to solve for the compressibility of the samples, the compressibility is calculated to be $1.611 \times 10^{-10} \frac{m^2}{N}$, which is quite different from the measured compressibilities. The deviation from the experimental compressibility values derives from the method of calculation. Most applications of Eq. 5 utilize the structural radius of the molecule, given by the expression¹⁰²

$$\frac{4}{3} \pi N r^3 = k \quad \text{Eq. 8}$$

where N is the number of molecules per unit volume, r is the structural radius, and k is the packing factor of molecules in the liquid (normally assumed¹⁰³ to be 0.7). Perova⁹⁰ indicates that the effective interaction radius in systems interacting with hydrogen bonds is somewhat smaller than the structural radius of the molecule.

Using the experimentally measured compressibilities from speed of sound experiments with Eq. 5, the interaction radius of the (*S*)-(-)- α -methylbenzylamine, r_{SS} , is 1.91 \AA , and the interaction radius of the molecules in racemic MBA, r_{RS} , is 1.93 \AA . These interaction radii are almost half of the radius, 3.3 \AA , if Eq. 8 is used, but the experimental values of 1.91 and 1.93 \AA are comparable to the interaction radius reported for water⁸⁵: 1.3 \AA . The standard deviation of the measured compressibility values is roughly 0.3% of the value, which is smaller than the estimated difference, $\sim 1\%$, between the r_{SS} and r_{RS} compressibilities.

From the above argument with r_{SS} and r_{RS} differences, one would assume that the density of the samples, ρ_{RS} vs. ρ_{SS} , would be different; though this may be true, the effective interaction radius corresponds to the distance at which the potential energy of two neighboring molecules corresponds to the thermal energy, $k_B T$, of the system. The effective interaction distance relates to the distance at which the two molecules begin to interact with one another, thereby not necessarily correlating to the structural radius of the molecule if hydrogen bonding is occurring.

Using the analogy of each of the molecules being a hand, either right-handed or left-handed depending upon the enantiomer, the ability of a molecule to interact with a

neighboring molecule may depend upon their relative handedness without necessarily significantly changing the density of the system. While maintaining the same net density, the left-left interaction may be closer due to electronic interactions via the π cloud overlap from the benzene ring. Zingg et al.⁹⁸, through the consideration of MBA and mandelic acid systems, showed that the systems with the same handedness tend to coordinate to one another more effectively, thus having a smaller radius of interaction. Referring back to Figure 3, the overlap between the two benzene rings in the (R)/(R) system was closer, which might be applicable to the interpretation of the MBA system results. To completely determine the average configurations in solution, molecular dynamic simulations and scattering experiments would be necessary.

Rodnikova et al.¹⁰⁴ give an interesting argument for the existence of a three dimensional hydrogen bonding network in various liquids based upon the magnitudes of isothermal compressibilities. Using a direct compression instrument, Rodnikova¹⁰⁵ measured the isothermal compressibilities of alkanes, alcohols, diamines, diols, aminoalcohols, and water. The results indicate that the species without a three dimensional hydrogen bonding network have higher compressibilities. For example, the compressibility of *n*-C₈H₁₄ is $16.45 \times 10^{-10} \frac{m^2}{N}$ while the compressibility of water is $4.599 \times 10^{-10} \frac{m^2}{N}$ where hydrogen bonding is known to play an important role in the liquid structure. Comparing the experimental compressibility for the RS and SS systems to water ($\beta = 4.473 \times 10^{-10} \frac{m^2}{N}$), there is only a slight difference, seeming to indicate that a three dimensional network of hydrogen bonding exists in MBA systems. Rodnikova¹⁰⁶ postulates that a system must possess two proton donor sites and two proton acceptor sites. The amine group of MBA contains the two proton donor and one proton acceptor site, with the other proton acceptor site being a little ambiguous, though it is believed that the other acceptor site is the benzene ring. Previous publications¹⁰⁷⁻¹¹² indicate that N-H π hydrogen bonding occurs in many diverse systems and is a weaker form of the more

common O-H hydrogen bonding systems. The typical energy of the N-H π interaction is ~ 1.2 kcal/mol¹⁰⁷.

Conclusion

The speed of sound in racemic and enantiomeric MBA has been measured to be 1503.7 ± 3.97 and 1489.3 ± 3.65 m/s respectively using a novel speed of sound technique. The magnitude of the compressibility for the MBA systems is confirmed with low frequency Raman measurements, but discrimination between the racemic and enantiomeric system is not possible because of the limit of the resolution. Using Eq. 5, the effective interaction radius between the two systems is expected to differ by only 0.02°\AA ; this difference is too small to be confirmed with the previous experiments, though in principle, the results do agree in general with the results by Zingg et al⁹⁸. Future measurements using different methods (2D NMR, X-ray and neutron scattering) may confirm these measurements.

Chapter VII.

Solvent Effects on the Optical Rotation of (*S*)- α -Methylbenzylamine

Introduction

Solvation is a phenomenon that is apparent in everyday life, but many facets are not well understood. Molecules in the gas phase are typically considered isolated, and thus the electronic distribution within the molecule reflects the isolated nature, but upon introduction of a solvent, many varying effects occur. Cyclohexane is typically considered to be an inert solvent, but the change of the electronic density from the gas phase to the solvated phase, exclusively a result of the dielectric constant of cyclohexane, can be profound. Most solvents are not considered to be inert, but rather have direct interactions with the solute via hydrogen bonding or other association phenomena.

A majority of known chemical phenomena occur in solution. Consequently, many studies have focused on environmental effects upon chemical reactions, which revolve around the role of the solvent and its interaction with the solute. A growing number of studies have considered the effects of the solvent upon reaction rates¹¹³, NMR^{114, 115}, UV-Vis¹¹⁶, vibrational spectroscopy^{117, 118}, CD^{119, 120, 121}, and ORD^{122, 123}. Generally, attempts are made to correlate properties of the solvent (dielectric constant, acidity, dipole moment, polarizability, etc.) to the trend in experimental observations. This study will focus on the influence of solvents upon the optical rotation of (*S*)-(-)- α -methylbenzylamine (MBA).

(*S*)-(-)- α -Methylbenzylamine (S-MBA), shown in Figure 1, belongs to a class of medically and biochemically important amines. Several papers^{124, 125} have used various theoretical methods to examine phenylethylamines' conformational behavior in solution. For example, Kumbar¹²⁵ has investigated the effects of the dielectric constant of the solvent upon the conformational behavior of phenylethylamines using an empirical method. Kumbar assumes that the molecular energy is given by

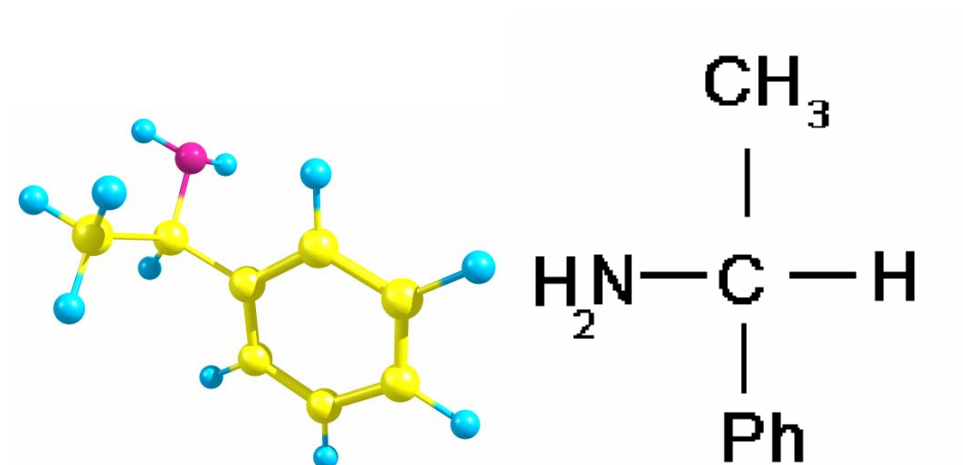


Figure 1. Structure of (*R*)-(+)-α-methylbenzylamine and (*S*)-(-)-α-methylbenzylamine respectively .

$$E(\theta, \psi) = E_{\text{nonbonded}} + E_{\text{torsional}} + E_{\text{electrostatic}} + E_{\text{H-bond}} \quad \text{Eq. 1}$$

where θ and ψ are dihedral angles between the phenyl and methine carbon and the angle between the two methine carbons, respectively. Kumbar's results indicate that the main factors controlling the orientation of the phenylethylamine are the nature of the solvent, substitutions, and the orientation of the substituents. The most drastic differences appear when the dielectric constant of the medium is less than 30.

An understanding of the chiroptical properties of MBA in pharmaceutical environments is of paramount importance. The circular dichroism of MBA and its derivatives has been well studied¹²⁶⁻¹³⁰. (S)-MBA exhibits a UV-Vis spectrum that is typical of a species containing a benzene substituent; the band at $\lambda=203.5$ nm is a $\pi \rightarrow \pi^*$ transition to the $^1B_{1u}$ state, and the band at $\lambda=254$ nm is also a $\pi \rightarrow \pi^*$ transition to the $^3B_{2u}$ state¹²⁹ of benzene. The $^3B_{2u}$ progression shows vibrational structure by adding totally symmetric vibrational quanta to the originating transition, but it should be noted that the $^3B_{2u}$ transition is forbidden and will only occur through such vibronic coupling. MacLeod et al.¹³⁰ combine calculations using Gaussian03 with experimental data to examine the differences between hydrated clusters in the gas phase with an experimentally hydrated system. MacLeod's results support the assumption of a correlation between the molecular gas phase structure and electronic circular dichroism measurements. Calculations of the rotatory strength, R_{01} , as a function of the rotation of the chiral side chain were performed in the gas phase or hydrated gas phase clusters, but only explicit addition of solvent molecules to the system can begin to mimic the intermolecular effects that occur.

Likewise, the optical rotatory dispersion of MBA has also been widely examined¹³¹⁻¹³⁶. These studies have focused mainly upon substitutional and Cotton effects; however, none of these studies considered how solvents interact with MBA and their effect upon optical rotation. A study by Smith and Willis¹³⁷ examined the effects of protonation of (S)-MBA by addition of hydrochloric acid. The results of this study gave $[\psi]_D = -9.800^\circ$, which equates to $[\alpha]_D = -8.090^\circ$ given¹³⁸

$$[\phi] = \frac{\alpha M}{100} \quad \text{Eq. 2}$$

with 2.0 grams (*R*)- α -Phenylethylamine hydrochloride in 100 mL of water, where α is the specific rotation and *M* is the molecular weight of the solute. Upon protonation of the amine, the rotation is seen to fall from its previous value of $[\alpha]_D = -39.91^\circ$ to -25.02° .

A wide variety of intrinsic and empirical solvent parameters exist, ranging from the dielectric constant, polarizability, acceptor and donor numbers, $E_T(30)$, to the Kamlet-Taft parameters α , β , and π^* ¹³⁹. The acceptor number¹⁴⁰ is an empirical quantity describing the electrophilic character of a solvent, and the donor number is a synonymous term that portrays the nucleophilicity of the solvent. The $E_T(30)$ solvent parameter¹⁴¹ is a scale of solvent polarity based upon the transition energy for the longest wavelength absorption band of a pyridinium-*N*-phenoxide betaine dye. The terms α , β , and π^* represent a solvent's acidity, basicity, and polarity/polarizability, respectively. Specifically, each term is based upon spectral shifts from a large catalog of UV/Vis data for solvatochromic compounds.

The Kamlet-Taft parameters have been successfully applied to the description of numerous spectroscopic phenomena: NMR¹⁴², UV-Vis¹⁴³, and IR¹⁴⁴. For this study, α , β , and π^* were utilized as the solvent parameters to describe optical rotation. The use of the Kamlet-Taft parameters is appropriate for the description of MBA because of MBA's ability to accept a hydrogen bond and give two hydrogen bonds simultaneously. In this study, the specific rotation was fit using the solvent parameters as

$$[\alpha]_{\lambda}^T = a\alpha + b\beta + c\pi^* + [\alpha]_{0,\lambda}^T \quad \text{Eq. 3}$$

where α , β , and π^* are the Kamlet-Taft solvent parameters, $[\alpha]_{\lambda}^T$ is the observed specific rotation, and $[\alpha]_{0,\lambda}^T$ is the optical rotation in a non-interacting solvent at wavelength λ and temperature *T*.

Solvation models are typically derived from the work of Born¹⁴⁵, Kirkwood¹⁴⁶, and Onsager¹⁴⁷. Several key features are used to differentiate types of solvation models, namely treatment of electrostatic interactions, the shape of the cavity, and the treatment of non-electrostatic interactions. Electrostatic interactions are the result of the placement of the solute's charge distribution leading to a solvent reaction potential; examples of treatment of the electrostatic interactions are the use of the molecular dipole¹⁴⁷, a

multipole charge distribution in a self-consistent reaction field (SCRF)¹⁴⁸, or variations of the multipole charge distribution¹⁴⁹ where the charge distribution is centered on atoms and bonds. The shape of the cavity for the solute molecule has evolved from being a simple spherical cavity to either a cavity defined by interlocking van der Waals spheres or ellipsoidal shapes. The non-electrostatic terms describe the other effects that are not electrostatic in nature (dispersion, repulsion, and cavitation energies).

The polarizable continuum model¹⁵⁰, PCM, places the solute with a charge distribution $\rho(\mathbf{r})$ in a cavity which is inside of an infinitely large polarizable dielectric medium having permittivity ϵ . The molecular charge induces a reaction potential in the solvent (dielectric continuum), which in turn acts on the solute and changes the initial charge distribution, $\rho(\mathbf{r})^0$. The cavity in turn has a surface charge with a charge density, $\sigma(s)$, which can be calculated via¹⁵⁰

$$\sigma(s) = \frac{\epsilon - 1}{4\pi\epsilon} E(s)_{n-} \quad \text{Eq. 4}$$

where $E(s)_{n-}$ is the electric field. The calculation of $\sigma(s)$ is an iterative process that is typically divided into 4 steps: determination of the unperturbed surface charge density, introduction of mutual polarization charges with unperturbed solute charge density $\rho(\mathbf{r})^0$, calculate new solute charge density $\rho(\mathbf{r})^1$, and repetition of cavity and solute charge density fields until self-consistency is reached.

The PCM methodology has been successfully applied to many different problems (see Tomasi¹⁵¹ for a review), and among those are the geometries and energetics of hydrogen bonded systems. Recent studies^{152, 153, 154} have surveyed many chemical systems and concluded that the B3LYP density functional with either the 6-311++G(2d,2p) or aug-cc-pVDZ basis set is an economic and efficient means to calculate the specific rotation with reasonable accuracy. This computational approach was used to compare with experimental optical rotations for MBA in a wide variety of solvents with known hydrogen bonding capabilities.

Experimental

(*S*)-(-)- α -Methylbenzylamine was obtained from Aldrich (>98%) and used without further purification. Solutions of (*S*)-(-)- α -methylbenzylamine and various solvents were prepared at specific concentrations of 0.25, 0.50, 1.00, 2.00, and 3.00 M. None of the solvents utilized in this study was purified further. Appropriate volumes of *S*-MBA were combined with each of the solvents to give a total volume of 2.0 mL at a specific molarity (M). All data points utilized represent the average of 3 or more measurements for each specific concentration. Optical rotations of the prepared solutions were measured on a Perkin Elmer 241 polarimeter at 25 °C at 589, 578, 546, 436, and 365 nm in a 1 cm cell. The experimental values for each concentration were fit to a quadratic curve as suggested by Landolt¹⁵⁵ and Eliel¹⁵⁶ and the intrinsic rotation was extrapolated as the optical rotation at zero concentration. The intrinsic rotation is defined as the specific rotation in an infinitely dilute solution thus avoiding solute-solute interactions. All optical rotation calculations were performed using the Gaussian03 program¹⁵⁷ with the B3LYP functional using an aug-cc-pVDZ basis set and PCM method of solvation. All necessary solvent parameters (dielectric constant, solvent radius, density, n_D^2 for dielectric constant at infinite frequency) necessary for calculations were taken from Marcus'¹⁵⁸ tabulation of solvent properties. Geometries of each system were optimized prior to the calculation of the optical rotation. Another series of calculations examined the method and basis set dependence for calculation of the optical rotation at 589 nm using PCM solvation in acetonitrile.

A simple multiple variable linear regression analysis was utilized for data analysis. Determination of outlier data points was based upon the standardized residual of each individual data point, and the line of best fit was continually refined until no outlier points remained. This method of refinement was used for the experimental and computational analysis.

Solvents were excluded from the analysis based upon statistical arguments. Specifically, the standardized residual for each data point that was rejected showed each data point to be more than twice the standard residual away from the predicted data point.

Table 1 shows the complete list of solvents that were seen as outliers for the data analysis; there is no consistent chemical phenomenon that is common to each of the excluded solvents. The exclusion of outlier data points does not affect the significance of the observation that systems with the ability to accept and donate hydrogen bonds must be described with multiple variables to accurately describe the specific rotation in solution.

Results and Discussion

The results for the calculations with varying methods and basis sets are shown in Table 2; the experimental intrinsic rotation at 589 nm for MBA in acetonitrile is -33.38° . As mentioned previously, several studies^{152, 153, 154} reported that the B3LYP functional with an aug-cc-pVDZ basis set gave the most economical and accurate results for the calculation of specific rotation. The results from Table 2 confirm that the B3LYP functional with an aug-cc-pVDZ basis set give better results than any basis set combined with Hartree-Fock theory.

The experimental intrinsic rotation and calculated specific rotations are shown in Table 3 and Table 4. Inclusion of solvent effects via PCM calculations is unable to account for concentration dependent effects, thus the concentration dependent optical rotation is fit to an appropriate form, as suggested by Landolt¹⁵⁵ and Eliel¹⁵⁶, and the specific rotation at infinite dilution, intrinsic rotation, is used. Transformation of the experimental data to the intrinsic rotation, $[\alpha]_{\text{Int.}}$, allows for a comparison with calculations, which assume an isolated molecule. The results of fitting the experimental intrinsic rotation at 589 nm to various standard correlations (Onsager function¹⁴⁷, dipole moment, $E_T(30)$ values, polarizabilities) for MBA can be seen in Figure 2-5. The correlation between the specific rotation and the Onsager function ($\frac{\epsilon - 1}{2\epsilon + 1}$) is rather weak with an R^2 value of 0.172, where R^2 defines the degree of correlation. There is also no correlation between the specific rotation and the dipole moment, D , with an R^2 value of 0.057. $[\alpha]_{\text{Int.}}$ is seen to decrease with increasing $E_T(30)$ with an R^2 value of 0.313. No

Table 1. List of excluded solvents during statistical analysis for each experimental wavelength and calculated values.

589 nm	Excluded Solvents
[α]_{Int.}	Carbon Tetrachloride, Nitrobenzene, Acetone, Diethyl Ether 1-Octanol, Pyridine, Triethylamine
[α]_{Calc.}	1,4 Dioxane, Bromobenzene, Benzene, Diethyl Ether, Toluene, 2-Phenylethanol THF, THP, Acetone, Di- <i>n</i> -butyl Ether, Acetonitrile, Benzyl Ether

578 nm	Excluded Solvents
[α]_{Int.}	Carbon Tetrachloride, Nitrobenzene, 1-Octanol, Acetone, Diethyl Ether Pyridine, 1-Propanol, 2-Phenylethanol, 1-Pentanol, Di- <i>n</i> -butyl Ether, Chloroform

546 nm	Excluded Solvents
[α]_{Int.}	Carbon Tetrachloride, Nitrobenzene, 1-Octanol, Acetone, Diethyl Ether Pyridine, 1-Propanol, 2-Phenylethanol, 1-Pentanol

436 nm	Excluded Solvents
[α]_{Int.}	Carbon Tetrachloride, Nitrobenzene, 1-Octanol, Acetone, Diethyl Ether Pyridine, 1-Propanol, 1-Pentanol, 2-Phenylethanol, N,N-Dimethylaniline Di- <i>n</i> -butyl Ether, Acetonitrile, THF, N-Methylaniline, <i>n</i> -Pentane

365 nm	Excluded Solvents
[α]_{Int.}	Carbon Tetrachloride, 1-Octanol, Acetone, Diethyl Ether, 1-Propanol, Pyridine 1-Pentanol, Di- <i>n</i> -butyl Ether, Acetonitrile, Benzyl Ether, THF

Table 2. Results of calculation of specific rotation at 589 nm with PCM solvation in acetonitrile with various methods and basis sets.

	STO-3G	3-21G	6-31G	6-31G*	cc-pVDZ	aug-cc-pVDZ
HF	-58.87	-63.91	-43.41	-54.61	-50.12	-28.87
B3LYP	-108.90	-91.93	-70.67	-85.48	-64.88	-33.63

Table 3. Tabulated infinite dilution optical rotations for all wavelengths. Some solvents absorbed 365 nm light too strongly to give an specific rotation at 365 nm.

Solvent	$[\alpha]_{589, 0}$	$[\alpha]_{578, 0}$	$[\alpha]_{546, 0}$	$[\alpha]_{436, 0}$	$[\alpha]_{365, 0}$
Isopropanol	-30.81	-32.13	-36.92	-64.93	-101.41
Toluene	-31.34	-32.71	-36.74	-61.94	-91.72
Ethanol	-28.99	-29.99	-37.39	-59.96	-93.31
1-Butanol	-29.96	-31.27	-35.53	-62.07	-96.98
Methanol	-26.38	-27.39	-31.16	-55.12	-86.33
Cyclohexane	-40.62	-42.55	-48.29	-81.46	-121.00
Methylene Chloride	-28.29	-29.60	-33.87	-57.97	-88.44
1,4 dioxane	-34.17	-35.47	-40.72	-69.37	-105.79
Dimethyl Sulfoxide	-26.25	-27.53	-31.27	-53.95	-83.83
Benzene	-31.86	-33.05	-37.97	-63.58	-92.18
Morpholine	-28.49	-29.63	-33.47	-57.83	-87.25
Bromobenzene	-29.78	-31.13	-34.70	-58.58	-87.29
Iodobenzene	-29.53	-30.89	-35.07	-58.24	-83.74
Dibromomethane	-26.13	-27.06	-30.83	-53.09	-81.86
Isobutanol	-27.58	-29.96	-34.77	-63.15	-103.12
Anisole	-32.45	-33.83	-38.50	-63.43	-93.74
Benzonitrile	-29.14	-30.12	-34.23	-59.17	-91.13
Chlorobenzene	-29.66	-30.64	-35.20	-59.10	-88.02
THP	-32.74	-34.02	-38.91	-66.23	-99.29
Triethylamine	-29.62	-41.88	-48.31	-81.66	-122.36
Chloroform	-28.05	-29.09	-33.34	-58.74	-91.94
<i>n</i> -Pentane	-38.29	-39.67	-44.05	-74.77	-112.16
Hexamethyl Triphosphoramide	-28.60	-29.84	-33.93	-58.38	-----
Nitromethane	-29.34	-30.69	-34.92	-60.19	-----
Nitrobenzene	-41.97	-44.09	-49.69	-84.41	-----

Table 3. Continued

2-Phenylethanol	-19.53	-20.41	-23.51	-41.01	-----
<i>N,N</i> -dimethylaniline	-29.11	-30.35	-34.14	-52.28	-----
<i>N</i> -methylaniline	-30.65	-31.59	-36.23	-63.63	-----
Carbon Tetrachloride	-52.29	-55.33	-61.22	-106.04	-162.30
1-Octanol	-18.20	-19.13	-21.56	-37.11	-57.38
Acetone	-39.10	-41.12	-47.24	-82.06	-126.36
Ether	-44.04	-46.07	-52.41	-88.90	-132.73
1-Propanol	-21.89	-22.85	-25.52	-44.84	-69.81
Pyridine	-36.09	-37.78	-42.62	-73.48	-112.43
1-Pentanol	-23.75	-24.80	-28.28	-49.30	-77.27
di- <i>n</i> -Butyl ether	-33.23	-34.48	-39.15	-66.27	-98.86
Acetonitrile	-33.38	-34.43	-39.37	-68.32	-104.92
Benzyl ether	-26.88	-28.83	-33.31	-55.00	-80.16
THF	-35.89	-37.51	-42.86	-73.26	-110.40

Table 4. Results for calculated specific rotation at 589 nm (B3LYP aug-cc-pVDZ PCM calculation) for all solvents. Kamlet-Taft solvent parameters for each solvent are listed.

Solvent	$[\alpha]_{\text{Calc.}}$	β	α	π^*
Isopropanol	-34.38	0.84	0.76	0.48
Toluene	-46.05	0.11	0.00	0.49
Ethanol	-33.24	0.75	0.86	0.54
1-Butanol	-34.65	0.84	0.84	0.47
Methanol	-32.71	0.66	0.98	0.60
Cyclohexane	-50.46	0.00	0.00	0.00
Methylene Chloride	-33.74	0.10	0.13	0.82
1,4 dioxane	-48.16	0.37	0.00	0.49
Dimethyl Sulfoxide	-34.62	0.76	0.00	1.00
Benzene	-46.75	0.10	0.00	0.55
Morpholine	-35.26	0.06	0.00	0.77
Bromobenzene	-44.56	0.70	0.29	0.74
Iodobenzene	-37.97	0.05	0.00	0.84
Dibromomethane	-35.07	0.00	0.00	0.92
Isobutanol	-34.97	0.84	0.79	0.40
Anisole	-38.17	0.32	0.00	0.70
Benzonitrile	-35.05	0.37	0.00	0.88
Chlorobenzene	-36.28	0.07	0.00	0.68
THP	-36.12	0.54	0.00	0.48
Triethylamine	-46.66	0.71	0.00	0.09
Chloroform	-36.88	0.20	0.10	0.58
<i>n</i> -Pentane	-52.66	0.00	0.00	-0.15
Hexamethyl Triphosphoramidate	-35.37	1.00	0.00	0.87
Nitromethane	-34.24	0.06	0.22	0.75

Table 4. Continued.

Nitrobenzene	-35.12	0.30	0.00	0.86
2-Phenylethanol	-35.11	0.61	0.64	0.88
<i>N,N</i> -dimethylaniline	-37.07	0.43	0.00	0.76
<i>N</i> -methylaniline	-35.73	0.47	0.17	0.82
Carbon Tetrachloride	-48.12	0.10	0.00	0.21
1-Octanol	-34.92	0.81	0.77	0.40
Acetone	-33.57	0.48	0.08	0.62
Ether	-37.85	0.47	0.00	0.24
1-Propanol	-33.71	0.90	0.84	0.52
Pyridine	-34.26	0.64	0.00	0.87
1-Pentanol	-34.43	0.86	0.84	0.40
di- <i>n</i> -Butyl ether	-41.80	0.46	0.00	0.18
Acetonitrile	-33.63	0.40	0.19	0.66
Benzyl ether	-39.49	0.41	0.00	0.80
THF	-34.52	0.55	0.00	0.55

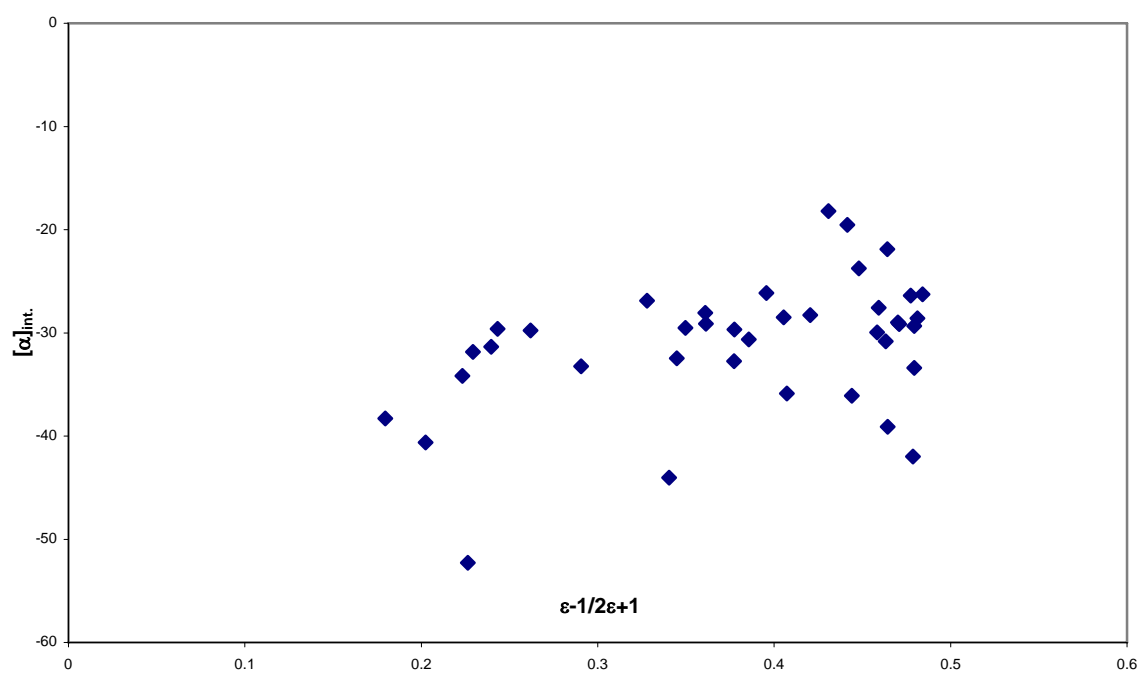


Figure 2. Plot of intrinsic rotation at 589 nm vs. Onsager function.

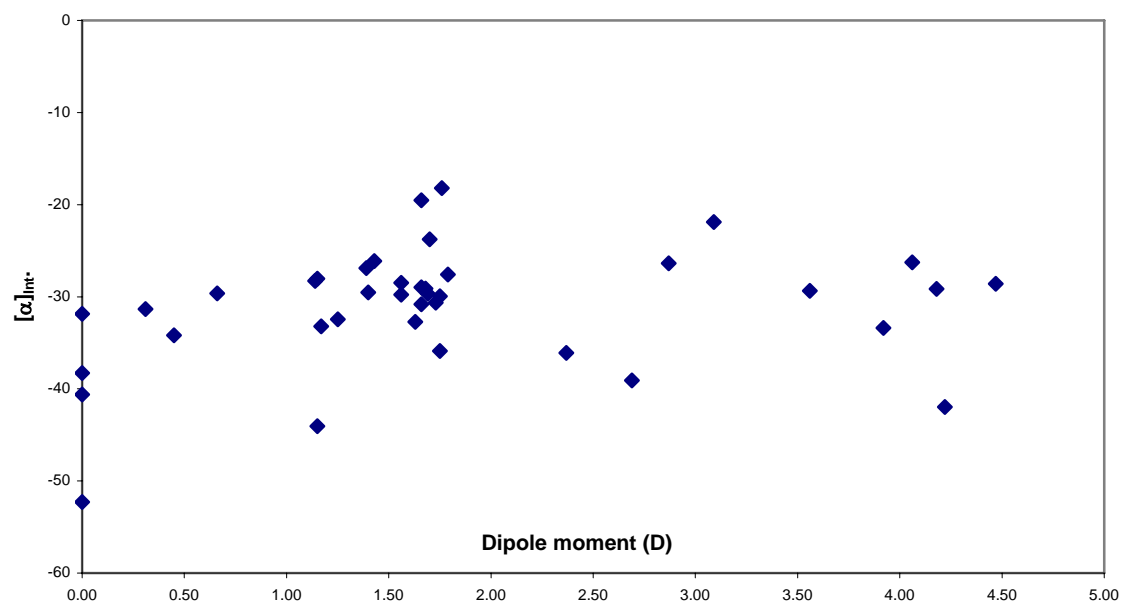


Figure 3. Plot of intrinsic rotation at 589 nm vs. dipole moment.

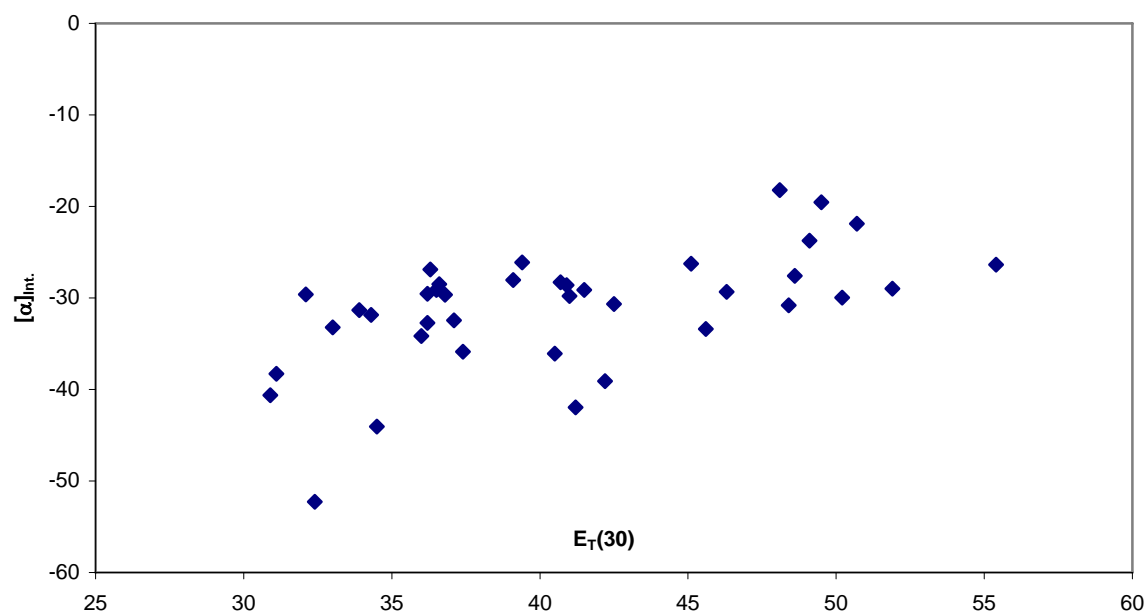


Figure 4. Plot of intrinsic rotation at 589 nm vs. $E_T(30)$ values.

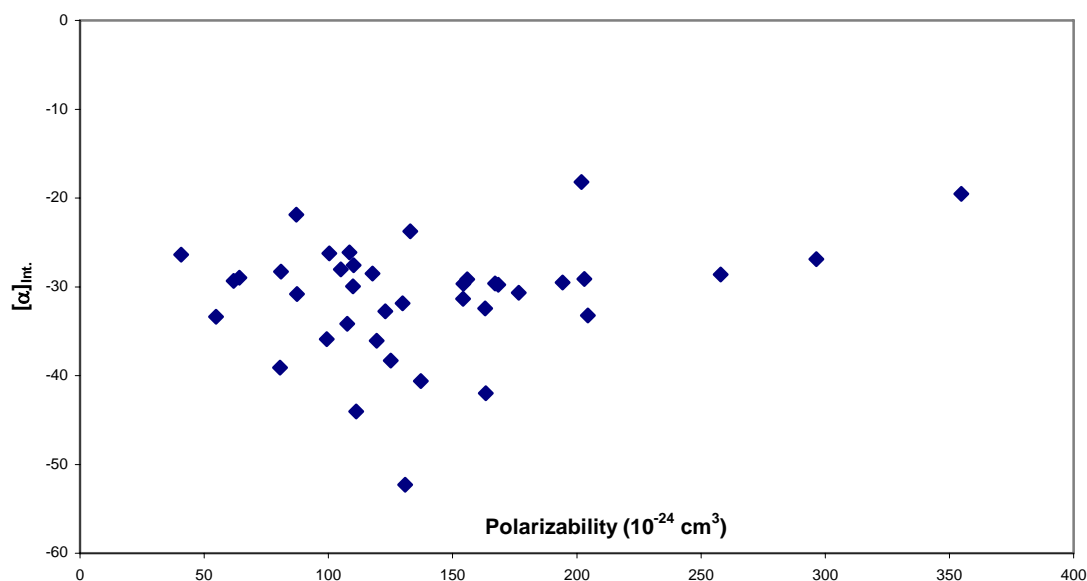


Figure 5. Plot of intrinsic rotation at 589 nm vs. polarizability as calculated from Classius-Mossoti equation.

correlation was found with $[\alpha]_{\text{int.}}$ and polarizability with an R^2 value of 0.058.

Polarizabilities were calculated using the Clausius-Mosotti equation¹⁵⁹

$$\alpha(\nu) = \left(\frac{3M}{N_A \rho} \right) \left(\frac{n_r^2 - 1}{n_r^2 + 2} \right) \quad \text{Eq. 5}$$

where M is the molar mass, N_A is Avagadro's number, ρ is the density, and n_r is the refractive index at the same frequency.

Previous research has successfully utilized the Onsager function, dipole moment, and $E_T(30)$ to correlate observed specific rotations. Rule and McLean¹⁶⁰ have extensively examined the effects of polar solvents on optical rotation for various chiral solutes. In this series of papers, they were able to make generalizations to the effects of highly polar solvents and associated solvents upon the optical rotation but did not consider other chemical effects. Mukhedkar¹²² investigated the effects of the dipole moment of the solvent on the optical rotation of camphor and α -bromocamphor; a nearly linear relationship was found between the apparent dipole moment and a rotational parameter. Kumata et al.¹²³ attempted to correlate the rotivity, Ω , given by

$$3\Omega = \frac{3[\alpha]}{n^2 + 2} \quad \text{Eq. 6}$$

where $[\alpha]$ is the specific rotation and n is the index of refraction of the solvent, to the chiroptical properties of propylene oxide with the Onsager function and $E_T(30)$ values. In both cases, a poor linear relationship was found. Mennucci et al.¹⁵² correlated the optical rotations of rigid chiral organic molecules with $E_T(30)$ values and noted a modest correlation. On the other hand, Wiberg¹⁶¹ found a correlation of the Onsager function with the optical rotation of 2-chloropropionitrile which was extrapolated to a predicted gas phase optical rotation. For these examined sets of molecules, hydrogen bonding can occur through either donation or acceptance of the hydrogen, but both processes do not occur in each of the molecules. (S)-(-)- α -Methylbenzylamine can donate to or accept a hydrogen bond from the solvent; clearly a more complete means of describing the optical rotation of MBA in solution is necessary.

Table 5 shows the results for the experimental and calculated multiple variable regression analysis for each wavelength and the calculated rotation at 589 nm. The

Table 5. Results for coefficients for each experimental wavelength and calculated rotation at 589 nm. The standard error for each wavelength are as follows: 589 nm- $\alpha \pm 1.75$, $\beta \pm 1.93$, $\pi^* \pm 1.81$, $[\alpha]_0 \pm 1.28$; 578 nm- $\alpha \pm 1.20$, $\beta \pm 1.23$, $\pi^* \pm 1.19$, $[\alpha]_0 \pm 0.86$; 546 nm- $\alpha \pm 1.67$, $\beta \pm 1.70$, $\pi^* \pm 1.60$, $[\alpha]_0 \pm 1.16$; 436 nm- $\alpha \pm 1.80$, $\beta \pm 1.83$, $\pi^* \pm 2.10$, $[\alpha]_0 \pm 1.57$; 365 nm- $\alpha \pm 3.56$, $\beta \pm 3.90$, $\pi^* \pm 3.12$, $[\alpha]_0 \pm 2.23$.

589 nm	α	β	π^*	$[\alpha]_0$	R value
$[\alpha]_{\text{Int.}}$	7.36	-0.54	11.18	-38.10	0.827
$[\alpha]_{\text{Calc.}}$	8.85	0.21	16.42	-49.52	0.974

578 nm	α	β	π^*	$[\alpha]_0$	R value
$[\alpha]_{\text{Int.}}$	6.07	-2.03	13.05	-40.50	0.921

546 nm	α	β	π^*	$[\alpha]_0$	R value
$[\alpha]_{\text{Int.}}$	5.48	-2.38	13.61	-44.90	0.866

436 nm	α	β	π^*	$[\alpha]_0$	R value
$[\alpha]_{\text{Int.}}$	8.70	-3.51	28.42	-79.85	0.951

365 nm	α	β	π^*	$[\alpha]_0$	R value
$[\alpha]_{\text{Int.}}$	11.33	-12.42	36.17	-113.63	0.941

importance of the π^* term is immediately recognizable from its magnitude to the contribution to the optical rotation. The experimental results show the dominant contributor to the optical rotation to be the π^* term, though the acidity of the solvent, α , is comparable in value to the importance of the polarity/polarizability term. The effect of the MBA to accept a hydrogen bond from the solvent is shown in the magnitude of β coefficient; for the experimental values, the sign of the β term is negative and opposite that of the α term. A B3LYP PCM calculation of the impact of the protonation of the amine (MBA⁺) with an aug-cc-pVDZ basis set in methanol gave a specific rotation of -7.37° , whereas a neutral molecule calculation in methanol gave a specific rotation of -32.71° . This calculation confirms the experimental model where protonation of the amine is expected to lower the specific rotation (looking at the sign of the α term).

It might be expected that the ratio between α and β and α and π^* would be consistent over all of the wavelengths, but that is not observed. At 589 nm, the ratio of α to β is 13.70, and at 365 nm, the ratio of α to β changes to 0.91. For each of the wavelengths, the ratio of α to π^* only varies from 0.66 (at 589 nm) to 0.31 (at 365 nm). A possible explanation of the changing of the ratio of α to β is that optical rotation receives a contribution from every wavelength, but the closer the experimental wavelength is to an allowed electronic transition, the relative importance of that transition increases, as shown by Equation 10 in chapter 5. The α and β terms reflect either the protonation of the amine or the donation of a hydrogen from the amine, and as the experimental wavelength approaches a UV-Vis absorption, the differences between the two processes will become more profound.

The results of the analysis for the calculated values show the π^* term to be most important in describing the optical rotation, and this result is expected since only the dielectric constant of the solvent is directly interacting with MBA in the PCM methodology. To demonstrate the impact of hydrogen bonding on optical rotation, an optimized B3LYP aug-cc-pVDZ PCM calculation in methanol of the fully protonated MBA (MBA⁺) gave a specific rotation of -7.37° , whereas the optimized neutral geometry in methanol gave a specific rotation of -32.71° . The experimental intrinsic rotation of

MBA in methanol is -26.38° , and neglecting the effects of MBA hydrogen bonding to the methanol molecule, the percentage of hydrogen bonded MBA molecules can be calculated via

$$[\alpha] = k[\alpha]_{MBA} + (1 - k)[\alpha]_{MBA^+} \quad \text{Eq. 7}$$

where $[\alpha]$ is the experimental intrinsic rotation in methanol, $[\alpha]_{MBA}$ is the calculated specific rotation in methanol of the neutral molecule, $[\alpha]_{MBA^+}$ is the calculated specific rotation of the cationic MBA in methanol, and k is the fraction of molecules that are not hydrogen bonded to methanol. Solving for k yields a value of $\sim 75.0\%$ MBA molecules not hydrogen bonded to methanol at infinite dilution. The amount of hydrogen bonded MBA at infinite dilution in methanol is probably larger than 25.0% ; the deviation is probably a reflection of the inaccuracy of assuming complete protonation of MBA. It should be noted that the calculated specific rotation of the protonated MBA, MBA^+ , is consistent with the prediction shown by the experimental values. The experimental intrinsic data analysis predicts that the specific rotation should be less negative upon protonation of MBA, as indicated from the α term, and this is observed qualitatively in the calculations. The experimental specific rotation at 589 of an equimolar mixture of MBA and HCl is -25.02° , thus the calculations and linear regression analysis are qualitatively consistent with the prediction of the protonated MBA specific rotation. Comparison of the experimental and calculated optical rotations at 589 nm can be extended to the optimized values for $[\alpha]_0$, where MBA is not directly interacting with the solvent or itself. The $[\alpha]_0$ from the experimental best fit is -38.10° whereas the calculated best fit for $[\alpha]_0$ is -49.52° , a glaring difference in the two methodologies. This distinct difference between methodologies does not restrict itself exclusively to cyclohexane; Table 6 shows a comparison of intrinsic and calculated specific rotations with solvents with small dielectric constants ($\epsilon < 3$) and small dipole moments ($\mu < 1$ Debye). Several of the solvents in Table 6 have the capability to form or accept hydrogen bonds, which are not included in the calculation. Table 6 shows that calculated specific rotations for solvents with low dipole moments differ significantly from the experimentally observed rotations. Wiberg et al.⁴⁹ suggest that solvents with zero dipole

Table 6. Experimental intrinsic and calculated specific rotations at 589 nm for solvents with $\epsilon < 3$ and dipole moment, μ (D), < 1 . Quadrupole moments, Q , are also listed.

Solvent	$[\alpha]_{\text{Int.}}$	$[\alpha]_{\text{Calc.}}$	ϵ	μ (D)	$Q * 10^{26} \text{ esu cm}^2$
Carbon Tetrachloride	-52.29	-48.12	2.24	0.00	0.00
Toluene	-31.34	-46.05	2.38	0.31	-8.00
Cyclohexane	-40.62	-50.46	2.02	0.00	13.60
Triethylamine	-29.62	-46.66	2.42	0.66	
1,4 Dioxane	-34.17	-48.16	2.21	0.45	-18.20
Benzene	-31.86	-46.75	2.27	0.00	-8.69
n-Pentane	-38.29	-52.66	1.84	0.00	

moment but large polarizabilities and quadrupole moments give larger than expected solvent effects; this may explain the deviation that is seen between the experimentally observed intrinsic rotations, $[\alpha]_{\text{Int.}}$, and the calculated specific rotations, $[\alpha]_{\text{Calc.}}$, shown in Table 6.

Conclusion

The specific rotation of (*S*)-(-)- α -methylbenzylamine has been measured in a wide range of solvents in a set of concentrations such that the intrinsic rotation, $[\alpha]_{\text{Int.}}$, can be determined and then correlated with the Kamlet and Taft solvent parameters α , β , and π^* . This first correlation of specific rotation to the Kamlet and Taft solvent parameters is found to be good. The data clearly show that direct interactions from hydrogen bonding are needed for a complete description of MBA in solution. The analysis shows that the solvent protonating MBA at infinite dilution is nearly equally important as the effects of the polarity/polarizability of the solvent. Analysis of the calculated specific rotations shows that the effect of polarity/polarizability of the solvent on specific rotation is exaggerated, and the contribution of β to the specific rotation is essentially neglected. To accurately determine the specific rotation of a system that can accept and donate hydrogen bonds, both chemical phenomena must be accounted for in determining the specific rotation. In accord with recent observations of Wiberg et al.¹⁶¹, solvents with small dipole moments ($\mu < 1$) but large polarizabilities and quadrupole moments give larger than expected solvent effects on optical phenomena.

Chapter VIII.

Mole Fraction Studies of α -Methylbenzylamine using FTIR and NMR with Applications to Optical Rotation Results

Introduction

The role of solvation is profound in chemical reactions. As illustrated in the preceding chapter, direct interactions between the solvent and solute can drastically alter the physical and chemical properties of a molecule. Visualizing a solvent as an infinite continuum defined by physical quantities (dielectric constant, density, etc.) is an incomplete description of the effects of solvents on a chemical system. Two experimental techniques that are commonly used to investigate solute-solvent interactions are vibrational and NMR spectroscopy; the frequency shift resulting from the presence of a solvent is defined as a solvatochromic shift. FTIR and NMR spectroscopy are appropriate techniques applied to the study of solvation because of the relative timescales that are measured. FTIR vibrational measurements acquire information that occurs at $\sim 10^{13}$ Hz, while NMR spectroscopy investigates phenomena on the timescale of $\sim 10^6$ Hz. By using both techniques together, a snapshot of a chemical phenomenon is seen with FTIR, while NMR gives time averaged signals that appropriately describe the equilibrium of the system.

Solvation energy is quantitatively defined as the interaction energy between solute and solvent molecules; specific and non-specific interactions contribute to the total interaction energy. The non-specific interactions are easily classifiable into five distinct groups: multipole-multipole, multipole (solute)-induced dipole (solvent), multipole (solvent)-induced dipole (solute), dispersion, and transition dipole moment (solute)-polarizability (solvent) interactions. The multipole-multipole and multipole-induced dipole interactions are the result of electronic interactions of molecules in solutions. The theories developed by Born¹⁴⁵, Kirkwood¹⁴⁶, and Onsager¹⁴⁷ attempted to describe these

interactions via the use of dipole moments of the solute and dielectric constants of the solvent. Dispersion interactions are the result of fluctuating dipole moments on an atom or molecule and lead to forces between atoms or molecules, and the transition dipole interaction assumes that the polarizable solvent affects the near instantaneous shift in electron distribution. Specific interaction contributions to the interaction energy are the result of association of solute and solvent molecules.

The result of the interaction energy is to shift absorption bands to either higher or lower energies, thus the solvatochromic shift. The shift of an absorption band to a higher energy is defined as a hypsochromic shift; conversely, the shift of absorption to a lower energy is a bathochromic shift. These shifts are typically referred to as blue and red shifts, respectively. With an understanding of a solvent (i.e. acidity, polarity, etc.), one can relate the results of shifts of specific absorption bands to the specific interactions that occur in solution. Likewise, the improvement of modern calculations has made it possible to conveniently compute the electronic effects of solvation. In the following paragraphs, a brief review will be given of relevant literature to the effects of solvation on infra-red and NMR spectra.

An early mathematical expression attempting to describe solvent effects on IR spectra was the KBM relationship^{55, 162}. The relationship related the strength of the dielectric constant to a shift, but was of little practical use. A few empirical or ab initio models have been able to correlate solvatochromic shifts in IR spectra mainly because of specific interactions. In 1962, Heald and Thompson¹⁶³ measured the frequency shift of carbonyl groups in varying solvents, and their results indicate that a simple dielectric model is unsatisfactory and that specific intermolecular forces are the impetus for the solvent shift. Specifically, they suggested that aggregations occur via $\text{C}=\text{O} \cdots \text{X}-\text{C}$, where X is a halogen. This study proceeded to investigate the solvent shifts over the entire mole fraction range for various carbonyls and observed red shifts on the order of 45 cm^{-1} .

Werner et al.¹⁶⁴ later extended the study of intermolecular interactions in solution by focusing on the association of proton donors and acceptors. The frequency region of amine ($3800\text{-}3100 \text{ cm}^{-1}$, N-H stretch) and carbonyl ($1700\text{-}1600 \text{ cm}^{-1}$, C=O stretch) vibrations were specifically monitored. Using the frequency measurements and a simple

model of equilibrium, equilibrium constants for self association of acetophenone and solvent molecules was established. The results of this study suggested that a clustering of solvent molecules around a solute molecule is the cause for solvent shifts. Numerous publications^{165, 166} have considered the effects of solvation on carbonyl stretch, and modest attention has been paid to N-H stretches^{167, 168}.

Wolff and Gamer¹⁶⁷ used IR in the fundamental and first overtone region of the NH stretches of dimethylamine to study the effects of concentration and temperature in various solvents. In non-associating solvents such as *n*-hexane and carbon tetrachloride, the position of the first overtone for NH stretches decreased as the mole fraction of amine decreased, revealing that at higher concentrations of amine association between the solute (amine) molecules occur.

The effects of specific interactions are not restricted solely to OH or NH stretches. Li et al.¹⁶⁹ recently examined the contributions that methyl groups make to stabilizing hydrogen bonds between dimethyl sulfoxide and methanol. Attenuated total reflectance FTIR measurements of methyl stretches in DMSO and methanol were recorded through the entire mole fraction range. Steady solvent shifts were observed from both the methyl peaks from the methanol and DMSO. Likewise, ¹H NMR spectra of the samples showed that low field and high field shifting occurred for the DMSO and methanol methyl protons, respectively. Coupled with calculations of methanol-DMSO complexes, Li et al. concluded that a charge transfer from the oxygen in DMSO to the OH in methanol resulted in an increase in electron density in methanol and decrease of electron density in DMSO, respectively. The changes in charge distribution were stabilized by the methyl groups on both DMSO and methanol, proving that hydrogen bonding affects the electronic density of groups beyond the direct centers involved. Figure 1 graphically shows the interpretation of Li et al.¹⁶⁹.

Solvent effects in NMR spectroscopy have also been well studied^{170, 171}. The bulk magnetic susceptibility and intermolecular interactions are the two main factors that contribute to solvent effects in NMR spectroscopy, but the bulk magnetic susceptibility is dependent upon the shape of the sample and the use of internal standards is a typical method to compensate for differing bulk susceptibilities. The

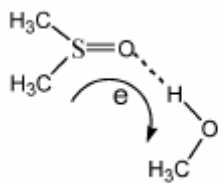


Figure 1. Illustration of electron movement from methyl groups of DMSO to stabilize hydrogen bond with methanol. Diagram from Li et al.¹⁶⁹.

chemical shift of a nucleus is determined partly by the shielding of the nucleus and any direct interactions in which the nucleus participates. In the study by Li et al.¹⁶⁹ the change in the chemical shifts for the methyl groups was a result of the change of charge distribution, resulting in a change in the shielding of the nuclei. The effect of hydrogen bonding on ^1H NMR is a well studied phenomenon^{172, 173}, and generally results in large chemical shifts from non-bonded values.

In a series of papers^{174, 175, 176}, chemists looked at chain association equilibria of solutes using NMR measurements; they derived a series of expressions that took into account the effects of the solvent on chemical shift. The derived expressions related the observed chemical shift to the interaction of oligomers and the solute to the solvent. Equilibrium constants were obtained from a least squares fit to the derived expressions for an inert and strongly hydrogen bonding solvent. The experiments for these studies used cyclohexane and carbon tetrachloride as inert solvents, and the results bear relevance to the present study. The chemical shifts for amide protons in cyclohexane and carbon tetrachloride were not different from the chemical shifts for the pure liquid until the mole fraction of the solvent was nearly 0.9, and then the chemical shifts of the amide protons deviated in a highly non-linear fashion. The conclusion of the studies with reference to the inert solvent results was the strong hydrogen bonding attractions between amide molecules to form oligomers. Figure 2 shows the chemical shifts for NH protons from LaPlanche et al.¹⁷⁴ in inert solvents. A similar analysis was utilized by Johnston et al.¹⁷⁷ with the analysis of the effects of hydrogen bonding, charge-transfer, and dipolar solutes in varying solvents.

The present study utilized mole fraction concentration ranges of MBA in FTIR and ^1H NMR experiments to investigate the structural and electronic changes in MBA in cyclohexane, toluene, nitrobenzene, DMSO, and methanol. Cyclohexane was chosen to represent an inert solvent to isolate the intermolecular effects from MBA. Toluene and nitrobenzene were selected since both possess a π electron cloud, but have very different polarities. Likewise, toluene has a similar molecular cavity to MBA with the methyl substituent instead of solely benzene. DMSO and methanol represent solvents that can accept hydrogen bonds ($\text{NH}\cdots\text{OS}$) or give hydrogen bonds, respectively. The results from

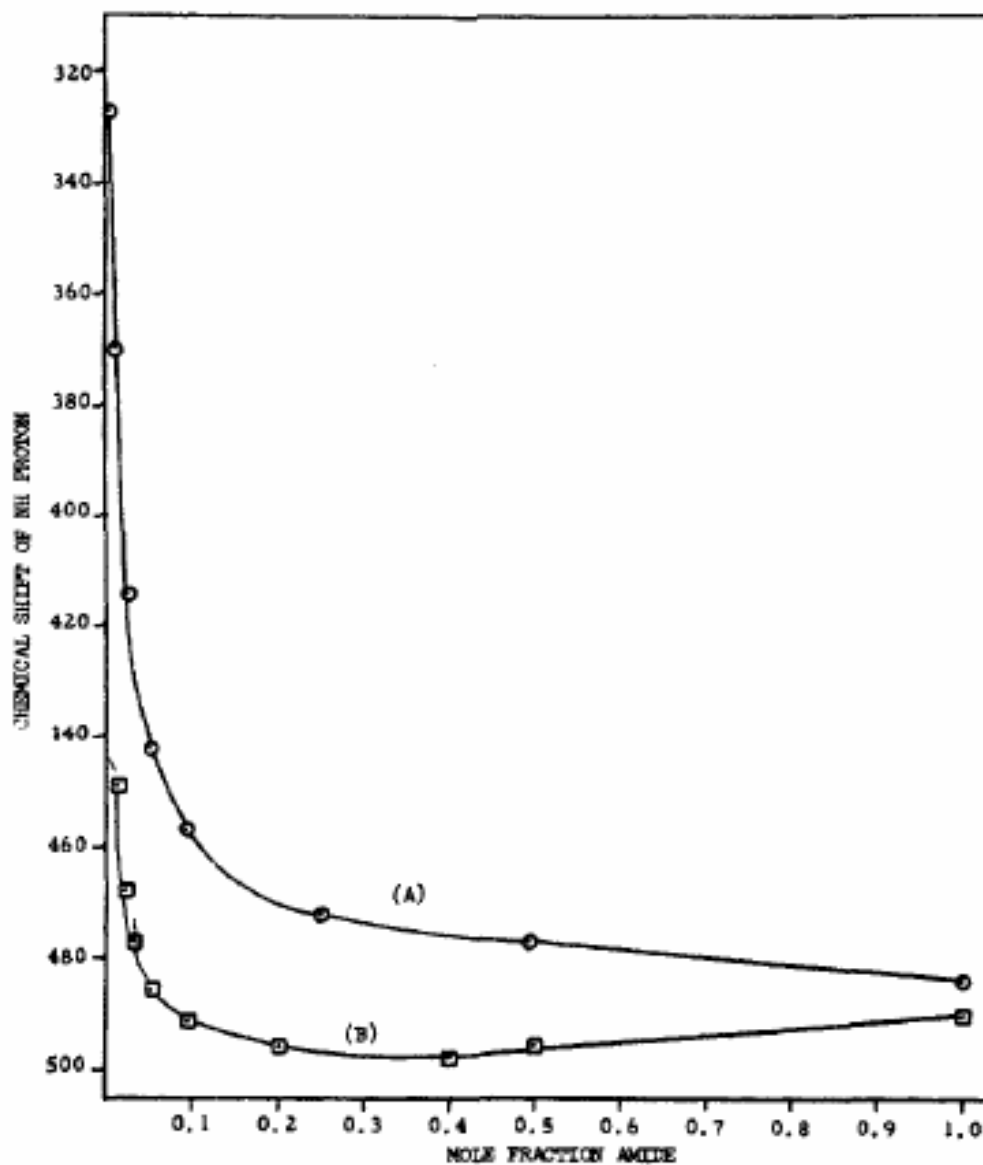


Figure 2. Results from LaPlanche et al.¹⁷⁴ for NH proton of *N*-isopropylacetamide in inert solvents. Line (a) is carbon tetrachloride, and line (b) is cyclohexane.

each solvent will be analyzed to make general conclusions on the effects that varying solvents have on MBA, and the general conclusions will be utilized to better understand what effects are most important contributors to the optical rotation.

Experimental

Samples of α -methylbenzylamine (MBA) were obtained from Sigma-Aldrich (>98%). Solutions were prepared by adding appropriate fractional volumes of MBA and solvent measured with a pipette with μL precision. Methanol was HPLC grade (99.9%), cyclohexane was obtained from Aldrich (99.5%), DMSO was obtained from Fisher Scientific (99.9%), nitrobenzene was obtained from Fluka (99.5%), and toluene was HPLC grade (99.9%). Solution concentrations were varied from pure solute ($\chi_{\text{MBA}}=1.0$) to pure solvent ($\chi_{\text{MBA}}=0.0$).

Infra-red spectra were recorded on a Bomem DA8 FTIR spectrometer. Small volumes of sample (~ 1 mL) were compressed between two MgF_2 plates. The IR source was a Globar, and 40 scans were recorded with a resolution of 0.25 cm^{-1} . A spectrum of the atmosphere and MgF_2 plates was recorded for each solvent and utilized as the background when converting to absorbance spectra. Infra-red spectra of all solvated systems (PCM solvation) were calculated with Gaussian03¹⁵⁷ using the B3LYP density functional with an aug-cc-pVDZ basis set. NMR spectra were recorded on a Varian 300 MHz spectrometer for protons. For all samples, a two chambered NMR tube was used to hold the sample and reference. Deuterium oxide (Cambridge Isotopes 99.9%) was the reference for all samples and was isolated from the samples to prevent interfering solvent effects. Optical rotations of the prepared solutions were measured on a Perkin Elmer 241 polarimeter at 25°C at 589, 578, 546, 436, and 365 nm in a 1 cm cell. All reported optical rotations are the average of 3 or more data points for each concentration. The volumes of MBA with each of the solvents was found to be additive through the addition of known volumes using μL pipette.

Results and Discussion

A concise summary of the results for all solvents is given in Table 1; all reported values have been extrapolated to infinite dilution. The asymmetric NH stretch was confirmed via calculation to be the higher frequency vibration in the NH stretching region. Asymmetric stretch frequencies were recorded as a function of χ_{MBA} and extrapolated to infinite dilution before comparison to theory. Results for the FTIR experiments and calculations are seen in Table 2; infinite dilution values for the asymmetric stretch were obtained by fitting the experimental data to a fifth order polynomial, except in the case of methanol which when corrected gave an unreasonably high value to correct for the suspect data point at $\chi_{\text{MBA}}=0.5$. For methanol, a fourth order polynomial was found not to give the upward deviation as χ_{MBA} approached zero. Calculated values for the asymmetric stretch with a PCM system were obtained with the B3LYP functional and aug-cc-pVDZ basis set. Precision of the experimental measurements is expected to be $\sim 0.25 \text{ cm}^{-1}$.

Results for the NMR experiments carried out in the same five solvents can be seen in Figures 3 through 7. Some data points at lower concentrations were not visible in the spectrum, and are thus not included. For each of the solvents, infinite dilution chemical shifts for the amine protons were extrapolated by fitting the data to polynomials. Methanol and cyclohexane were fit using a cubic polynomial because higher order polynomials gave values that were unreasonable (~ 10.500 and -1.254 ppm, respectively). Fifth order polynomials were utilized for all other solvents. The accuracy of the ^1H NMR peaks is expected to be on the order of 0.010 ppm.

The optical rotation data can be presented in several formats due to the additive volumes for the selected solvents (mole fraction, molarity, molality, etc.), but Figures 8 and 9 show the results for observed optical rotation at 436 nm and specific rotation at 436 nm versus mole fraction, respectively. Each of the measurements is the result of 3 separate measurements averaged together; standard errors of measurements were higher at lower concentrations and were the result of difficulty in reproducing exact concentrations. At $\chi_{\text{MBA}} = 0.1$, the average standard error is $\sim 5\%$. Infinite dilution

Table 1. Summary of results for asymmetric NH stretch, $\delta(\text{NH}_2)$, and optical rotation at 436 nm for all solvents. All results presented are for infinite dilution.

	ν_0	$\nu_{\text{Calc.}}$	$\delta^0(\text{NH}_2)$	$[\alpha]_{436, 0}$
Cyclohexane	3583.6	3531	1.545	-74.99
Toluene	3382.2	3522	0.666	-80.40
Nitrobenzene	3380.6	3459	2.040	-77.28
DMSO	3349.2	3454	3.406	-66.87
Methanol	3345.6	3457	6.390	-58.75

Table 2. Results for FTIR experiments and calculations of MBA. The ν_{asy}^0 and $\nu_{asy}^{Calc.}$ refer to the extrapolated infinite dilution value and calculated value for the asymmetric stretch. Calculations utilized the B3LYP functional with aug-cc-pVDZ basis set PCM methodology.

	Cyclohexane	Toluene	Nitrobenzene	Methanol	DMSO
χ_{MBA}	$\nu_{asy} \text{ (cm}^{-1}\text{)}$	$\nu_{asy} \text{ (cm}^{-1}\text{)}$	$\nu_{asy} \text{ (cm}^{-1}\text{)}$	$\nu_{asy} \text{ (cm}^{-1}\text{)}$	$\nu_{asy} \text{ (cm}^{-1}\text{)}$
1.0	3366.5	3366.5	3366.5	3366.5	3366.5
0.9	3366.8	3368.1	3367.1	3364.3	3363.9
0.8	3367.7	3369.5	3369.3	3361.6	3365.4
0.7	3367.9	3370.3	3371.2	3357.1	3361.4
0.6	3369.3	3371.5	3372.8	3353.2	3359.9
0.5	3370.3	3373.4	3374.5	3357.2	3359.2
0.4	3370.4	3375.8	3376.7	3349.3	3358.7
0.3	3372.3	3377.4	3378.2	3346.9	3356.9
0.2	3380.7	3379.9	3379.6	3343.8	3356.8
0.1	3439.4	3381.5	3380.9	3344.0	3353.8
ν_{asy}^0	3583.6	3382.2	3380.6	3345.6	3349.2
$\nu_{asy}^{Calc.}$	3531	3522	3459	3457	3454

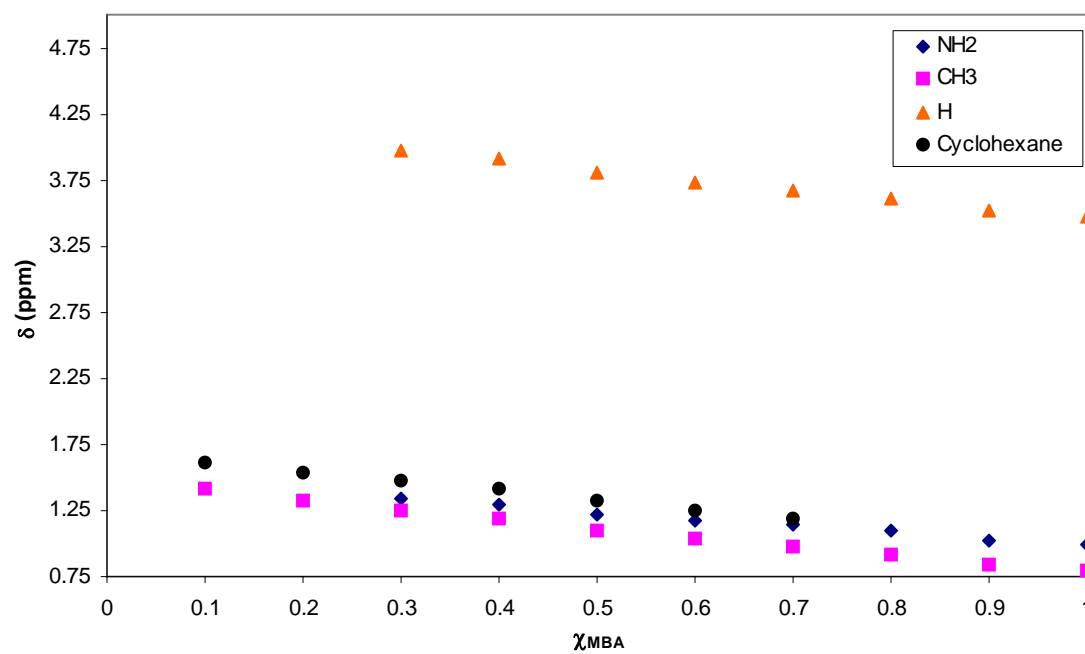


Figure 3. Results for the ^1H NMR experiments for MBA and cyclohexane.

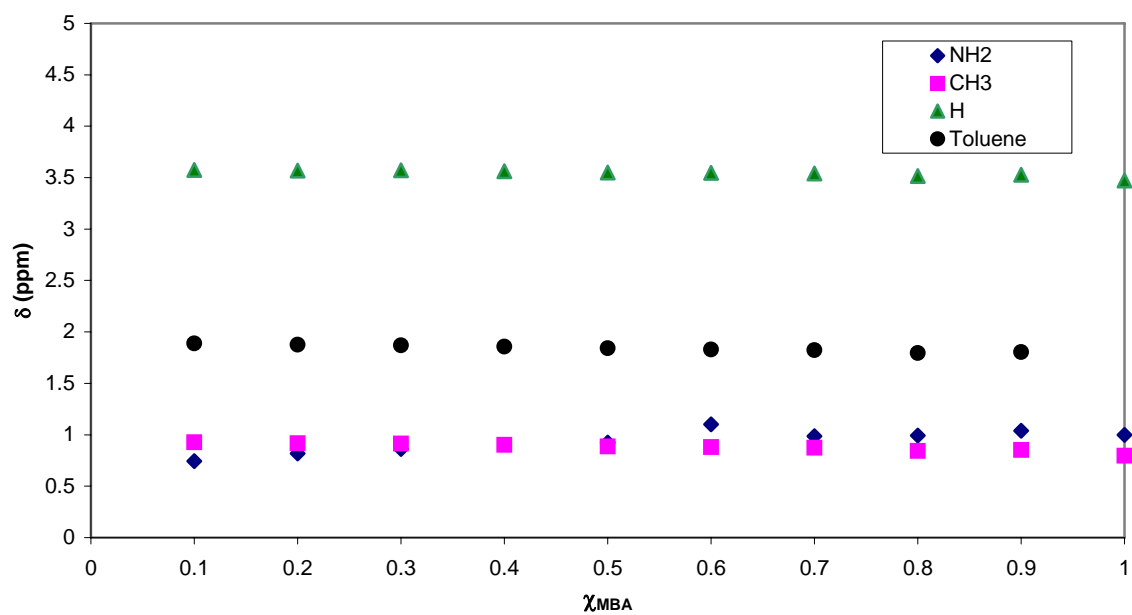


Figure 4. Results for the ^1H NMR experiments for MBA and toluene.

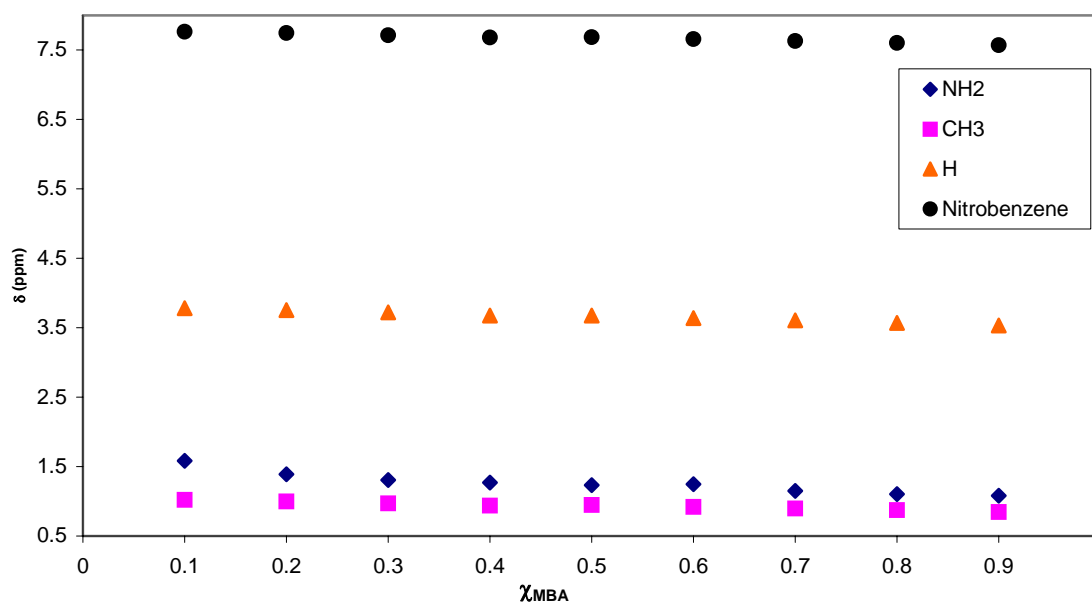


Figure 5. Results for the ^1H NMR experiments for MBA and nitrobenzene.

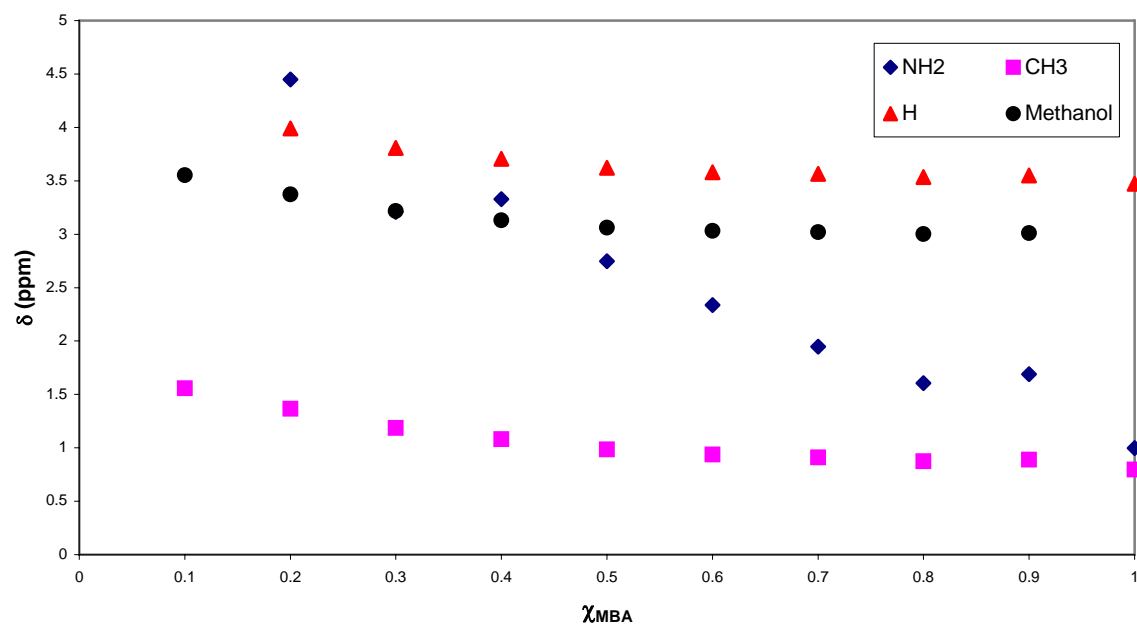


Figure 6. Results for the ^1H NMR experiments for MBA and methanol.

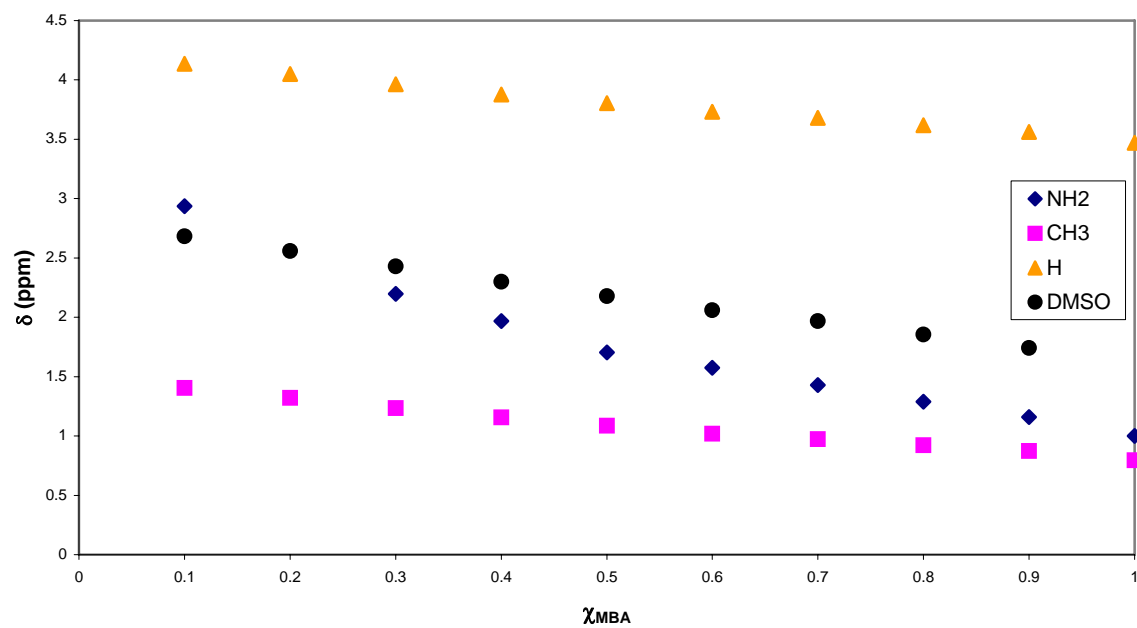


Figure 7. Results for the ^1H NMR experiments for MBA and DMSO.

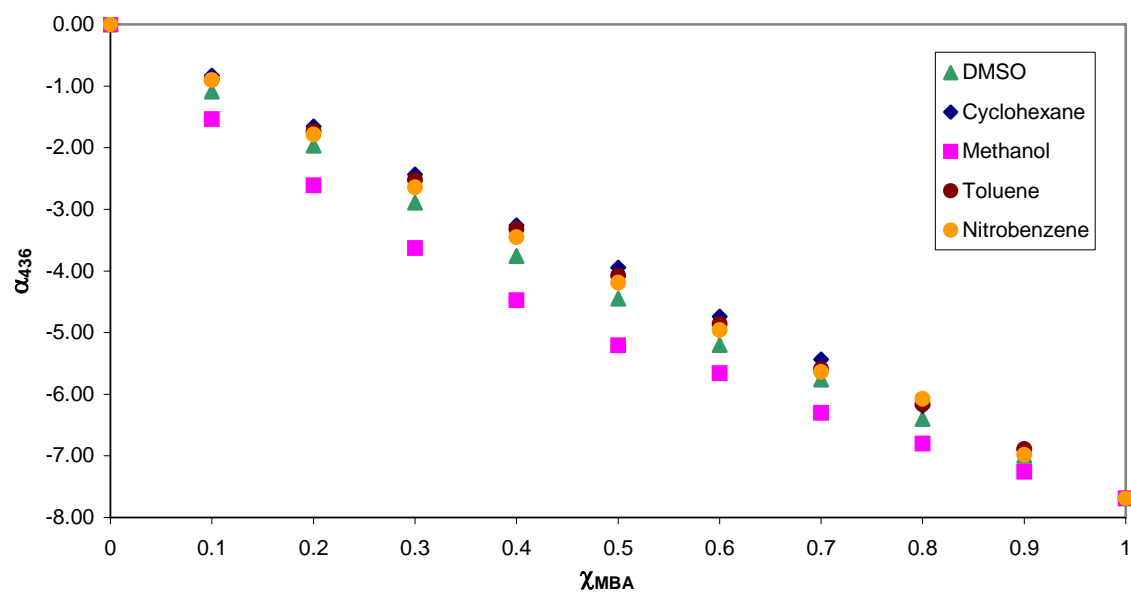


Figure 8. Observed optical rotation at 436 nm with respect to mole fraction MBA for various solvents.

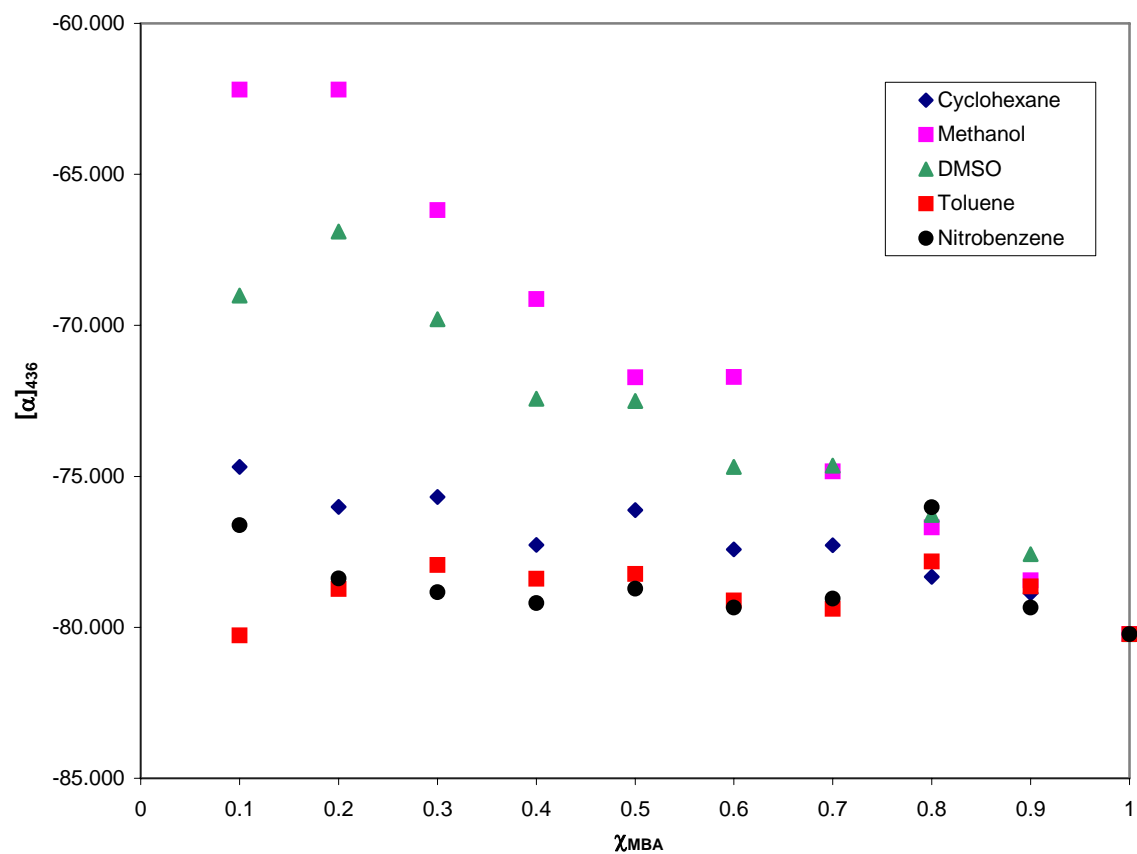


Figure 9. Specific rotation at 436 nm for MBA with respect to mole fraction for various solvents.

analysis with respect to optical rotation was discussed in the previous chapter and will be excluded from present discussions.

The results for each of the solvent experiments will be discussed separately before pulling all of the results together for a conclusion on the overall solvent effects. For MBA in cyclohexane, it is assumed that MBA does not directly interact with cyclohexane; thus, the only direct interactions that are occurring in solution are the MBA-MBA interactions. At some low χ_{MBA} , it is expected that the interactions between MBA will weaken and eventually cease to exist. The asymmetric N-H stretch in cyclohexane maintains a fairly constant frequency until $\chi_{\text{MBA}} \sim 0.2$ and then jumps drastically at $\chi_{\text{MBA}} = 0.1$. The explanation of the drastic change in the frequency for the asymmetric stretch at low χ_{MBA} is consistent with LaPlanche et al.¹⁷⁴; at a low enough concentration, the interactions between the NH groups are weakened, leading to a drastic shift. Fitting the data to a fifth order polynomial, the extrapolated zero concentration (infinite dilution) N-H stretch is at 3583.6 cm^{-1} , which compares fairly favorably with the calculated 3531 cm^{-1} asymmetric N-H stretch in cyclohexane. With no direct interactions with cyclohexane at infinite dilution, the change in the frequency of the asymmetric stretch is a result of pure solvation effects resulting from the dielectric constant of cyclohexane. Furthermore, the accuracy of the calculation, $\sim 1.5\%$, gives a good approximation of the accuracy of the non-direct solvation effects for other solvent calculations. No experimental data are available for the gas phase asymmetric N-H stretch frequency for comparison to the cyclohexane data.

The NMR data for MBA in cyclohexane show that all of the solute and solvent protons move to lower chemical shifts as the concentration of MBA increases. As the IR data indicates, results at $\chi_{\text{MBA}} = 0.1$ are more indicative of the non-hydrogen bonded species, therefore relationships of the NMR data will always be in reference to the lower concentration data. From the results of the calculated optimized structures in the gas and solution phases, Mulliken charges were obtained. Table 3 shows the Mulliken charges of MBA protons and other atomic centers for the gas phase geometry and the solvated geometries (not all atomic centers are shown, but summation of all centers gives a charge of zero). In the gas phase, the Mulliken charge on the amino protons is -0.12 , but in

Table 3. Tabulated results for Mulliken charges in solvated systems. The methanol inc. column refers to calculation with methanol molecule included in calculated system, as shown in Figure 13.

	Gas phase	Cyclohexane	Toluene	Nitrobenzene	DMSO	Methanol	Methanol Inc.
Nitrogen	0.07	0.03	0.02	-0.05	-0.07	-0.06	-0.51
Chiral Carbon	0.29	0.32	0.35	0.37	0.40	0.39	0.37
Methyl Carbon	1.03	1.02	1.00	1.01	0.99	0.99	1.13
CH	-0.61	-0.60	-0.61	-0.59	-0.60	-0.60	-0.66
CH ₃	-0.28	-0.28	-0.28	-0.28	-0.28	-0.28	-0.30
NH ₂	-0.11	-0.09	-0.09	-0.06	-0.07	-0.07	-0.13

cyclohexane, the Mulliken charge on the amino protons is -0.10 therefore, less electron density is present, shifting the protons to a higher chemical shift, and as is seen from the NMR experiments, the amino protons are at a higher chemical shift at low concentration. Interestingly, nonlinear behavior of the chemical shift for the amino protons at low MBA mole fraction is not seen, which may indicate that even lower mole fraction measurements are needed to observe nonlinearity. Neither the CH nor the CH₃ protons show a change in the Mulliken charges from calculations, but the chiral carbon and methyl carbon do show slight changes in solvation, which may account for the experimentally observed changes for the methyl and chiral carbon proton move to higher chemical shift at low MBA concentration.

A linear relationship for the observed optical rotation with χ_{MBA} indicates that cyclohexane is an inert solvent for MBA. From calculations and experiment, hydrogen bonding is shown to decrease the absolute value of the optical rotation, and the extrapolated optical rotation in cyclohexane at zero concentration will be considered the intrinsic optical rotation, which is estimated to be -74.99° at 436 nm (obtained by using a quadratic fit to experimental mole fraction data). For future solvent considerations, deviations from -74.99° for the specific rotation at 436 nm will be a reflection of either hydrogen bonding or electronic effects from the solvent.

When considering toluene, interactions between MBA-MBA are assumed to be present, and interactions between toluene's π cloud and MBA are expected. Specifically, the main effects that may be exhibited would be those from the π cloud in toluene attracting the hydrogen from the amino group. The π -H₂N interaction is not different than the interaction that would be expected from the intermolecular MBA-MBA from the benzene chromophore to the amino group, but in the interaction of toluene with MBA, toluene cannot donate a hydrogen bond to amino group, thus the effects of the benzene group on the amino protons have been isolated. The FTIR results for toluene obey a linear relationship, showing increasing frequency for the asymmetric N-H stretch with decreasing mole fraction, and when fit to a fifth order polynomial, the infinite dilution peak for the asymmetric NH stretch is 3382.2 cm^{-1} as opposed to 3382.4 cm^{-1} when using a linear approximation. Similar to cyclohexane, the lower frequency results indicate an

attraction of the amine lone pair electrons toward another species, which in turn results in a lowering of the bond strength between N-H when the nitrogen compensates for the charge shift by pulling more charge from the other protons. None of the experimental concentrations display behavior similar to the cyclohexane FTIR spectra where at $\chi_{\text{MBA}}=0.1$ the amine hydrogen bonding is broken down. The π -H₂N is not expected to be very strong, so it is suggested that the observed deviation from linearity would occur slightly below the lowest experimental concentration of $\chi_{\text{MBA}}=0.1$. The calculated asymmetric N-H stretch is at 3522 cm⁻¹, differing by ~4.1% from the experimental value. The deviation of the calculated value is probably a reflection of both the linearity, where non-linearity is expected at lower concentrations, and the mild π -H₂N attraction.

The NMR experiments for MBA in toluene show interesting results; the only protons with shifting positions are those of the amine protons, and they show increasing chemical shift with increasing mole fraction of MBA. The Mulliken charges on the amine protons in toluene are expected to be lower, therefore, it would be expected that at lower concentration of MBA, the chemical shift of the amine protons would be higher, but that is not observed experimentally. The suspected cause for this effect is the result of toluene's π cloud; evidence for this explanation is that no other protons seem to be affected by the mole fraction of MBA, and the main chemical difference from cyclohexane to toluene is toluene's π cloud.

MBA shows a nearly linear relationship with observed rotation in toluene at 436 nm, and the specific rotation at 436 nm does not change, when accounting for standard deviations, with respect to concentration. The extrapolated specific rotation at infinite dilution for 436 nm in toluene is -80.40°, slightly different from the specific rotation in cyclohexane after accounting for ~5% deviation. Coupled with the information from FTIR and NMR experiments, this suggests that the NH₂- π interaction is weak and bears little effect to the optical rotation.

Nitrobenzene and toluene are alike in some respects and different in others. Nitrobenzene has a π cloud as does toluene. However, rather than a non-interacting methyl substituent on the benzene ring, it has a highly polar nitro group which gives rise to new molecular interactions. The FTIR experiments in nitrobenzene gave results that

were very similar to those in toluene; the asymmetric NH stretch in both toluene and nitrobenzene shows decreasing frequency with increasing MBA mole fraction, indicative of the breakdown of the intermolecular MBA hydrogen bonding. Similar to toluene, the data for nitrobenzene are nearly linear; when the data are fit with a fifth order polynomial or linear function, the infinite dilution extrapolations are 3383.0 and 3380.6 cm^{-1} , respectively. The extrapolation of the infinite dilution N-H asymmetric stretch is slightly lower in frequency than toluene, so even with the highly polar nitro group, not many interactions, other than through the π cloud, are seen. This is significant in that the polarity of the group off of the benzene ring does not drastically affect the position of the asymmetric stretch. The calculated asymmetric stretch in nitrobenzene is 3459 cm^{-1} , a difference of only 2.3% from the observed frequency.

Similar to what was seen in toluene, the amine protons in nitrobenzene experience different chemical shifts as a result of the change in mole fraction of MBA, but rather than increase chemical shift with increasing mole fraction, a decrease in the chemical shift for the amine protons is observed. An analysis of the calculated Mulliken charges in nitrobenzene reveals that the amine protons have more partial charge when in nitrobenzene than either the gas phase or in cyclohexane, which can be interpreted to mean that less electron density is on the amine protons, in turn shifting the peak positions to higher chemical shifts. This shift is observed experimentally, and when extrapolating the amine protons to infinite dilution in nitrobenzene, the chemical shift is higher than in cyclohexane's infinite dilution chemical shift, 2.040 vs. 1.545 ppm respectively. Chemically, the main difference between nitrobenzene and toluene is the highly polar group attached to the benzene ring, thus it is expected that the highly polar group is able to 'pull' the electrons away from the amine group. Interestingly, none of the other protons feel this 'pull', and thus are not affected in the NMR measurements.

The observed optical rotation at 436 nm shows a nearly linear response, similar to toluene and cyclohexane, and the specific rotation at 436 nm in nitrobenzene extrapolates to a value of -77.28° when fit to a quadratic curve. The extrapolated specific rotation is within 5% of the experimentally determined specific rotation of MBA in cyclohexane.

Including the conclusions from the FTIR and NMR experiments, it appears that the polarity of the nitro group does not significantly affect the optical rotation. Likewise, the effects of the benzene chromophore, and its particular orientation, do not appear to be a significant contributor to the optical rotation.

The last two solvents to be considered, dimethyl sulfoxide and methanol, show very different behavior than the previously discussed solvents. Of these two solvents, DMSO is a more straight forward interpretation and will be considered first. Looking at the results of the FTIR experiments, the frequency of the asymmetric N-H stretch increases with increasing mole fraction of MBA, which suggests that MBA is donating the lone pair of electrons from the nitrogen to DMSO, thereby explaining the lowering of the asymmetric frequency as the concentration of DMSO increased; the proposed scheme is shown in Figure 10. Donating the lone pair electrons to sulfur in DMSO would give a positive charge on the nitrogen of MBA, but the electrons in the double bond from sulfur to oxygen would be pushed to give a single bond from sulfur to oxygen and an excess electron on oxygen, and therefore a negative charge. The electrostatic attraction of MBA to DMSO through the amino nitrogen is not a permanent bonding scenario, but is stabilized by the pushing of electrons to oxygen. In a simpler sense, the MBA molecule is acting as a Lewis base and DMSO as a Lewis acid. The extrapolated asymmetric N-H stretch at infinite dilution is 3349.2 cm^{-1} , which is slightly lower than either of the previously examined solvents. The calculated frequency for the asymmetric stretch is 3454 cm^{-1} , different by 3.1% from the experimental value. A majority of this slight deviation is due to the direct interactions that occur between MBA and DMSO, as illustrated in the different behavior when DMSO is the solvent.

The chemical shifts for all protons in MBA/DMSO increase with more DMSO present (i.e. lower χ_{MBA}). At $\chi_{\text{MBA}}=0.2$, there is some ambiguity as to the position of the amino proton peak as both the DMSO methyl and amino proton peaks overlap. The hypothesis of electron exchange occurring at the MBA nitrogen to the DMSO sulfur is supported by the apparent effects of all protons near the vicinity of said 'bonding'. The greatest chemical shift changes are seen in the amino protons, and that is not unexpected as it is the center of the bonding process. If indeed a temporary partial charge is found on

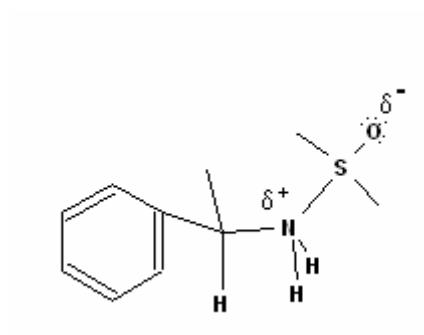


Figure 10. Scheme of the proposed electrostatic interaction between MBA and DMSO.

the nitrogen, electron density from surrounding groups would be ‘pulled’ toward the positive charge, and the groups that are closer would feel the greatest effects. The protons that are closest to the partial bond formation are the methyl groups of DMSO; it is observed that their chemical shift change is greater than all other protons except for the amino protons. The CH and CH₃ protons on MBA both experience ~0.7 ppm chemical shift changes from pure MBA to $\chi_{\text{MBA}}=0.1$ indicating that both groups experience a charge redistribution as a response to the ‘bond’ formation between MBA and DMSO. The Mulliken charge analysis in DMSO indicates that the amino protons have slightly higher charges when compared to cyclohexane, though the charge analysis for the CH and CH₃ protons show no respective changes in charges for solvation in DMSO, indicating that their chemical shift responses to DMSO are probably a response to the direct interactions between MBA and DMSO.

The observed optical rotations at 436 nm in DMSO as a function of mole fraction deviate slightly from linearity; Figure 8 shows that all of the data points for DMSO are lower in value than those in cyclohexane, toluene, and nitrobenzene, with the largest deviation at $\chi_{\text{MBA}}=0.5$. The specific rotation in DMSO at 436 nm decreases with mole fraction of MBA and is consistent with calculations that the specific rotation increases with a positive charge on the nitrogen; it should be noted that these calculations were performed for a hydrogen bonded to the nitrogen, not a sulfur atom. Fitting the optical rotation data to a quadratic function gives a specific rotation of -66.87° at infinite dilution, substantially lower than the value obtained in cyclohexane.

In methanol, the asymmetric N-H stretch behaves similarly to that in DMSO, but the frequency in methanol changes much more drastically than is observed in DMSO. In methanol, the frequency at infinite dilution is 3345.6 cm^{-1} , a shift of $\sim 21\text{ cm}^{-1}$ from the pure MBA to infinitely solvated MBA. Similar to what is seen in DMSO, the decrease of the vibrational frequency in methanol at infinite dilution is consistent with an expected hydrogen bond being present between methanol and MBA. Several other scenarios for bonding were investigated using calculations; Figure 11 shows an optimized structure for MBA^+ in methanol calculated with an aug-cc-pVDZ basis set, and Figure 12 shows an optimized geometry for an MBA dimer in methanol calculated with a cc-pVDZ basis set.

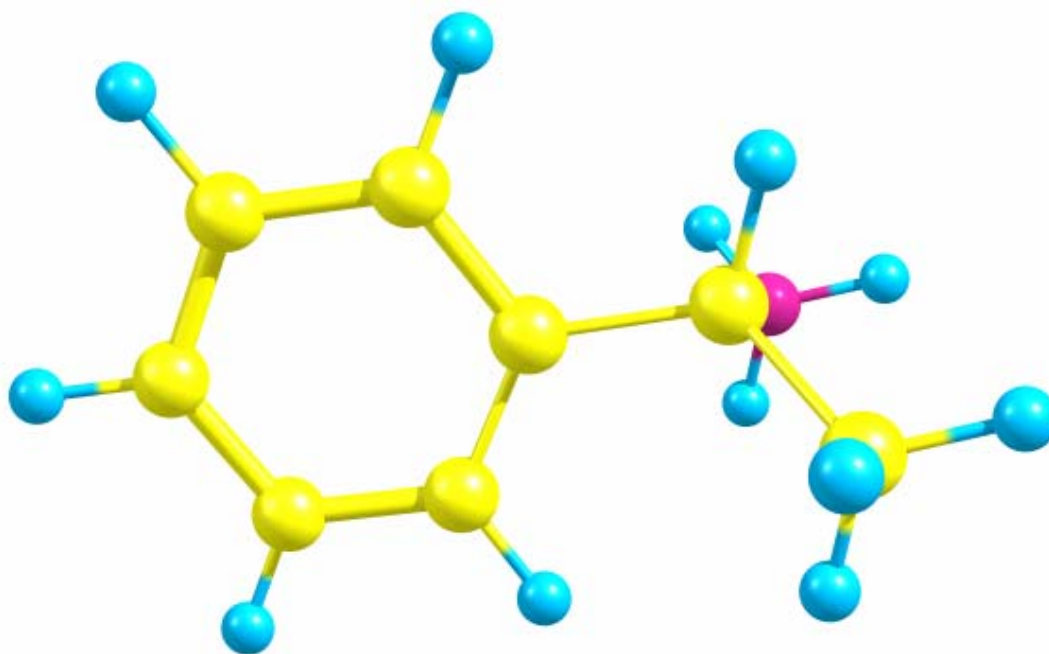


Figure 11. Optimized structure for MBA^+ in methanol. Calculated with PCM B3LYP theory with aug-cc-pVDZ basis set.

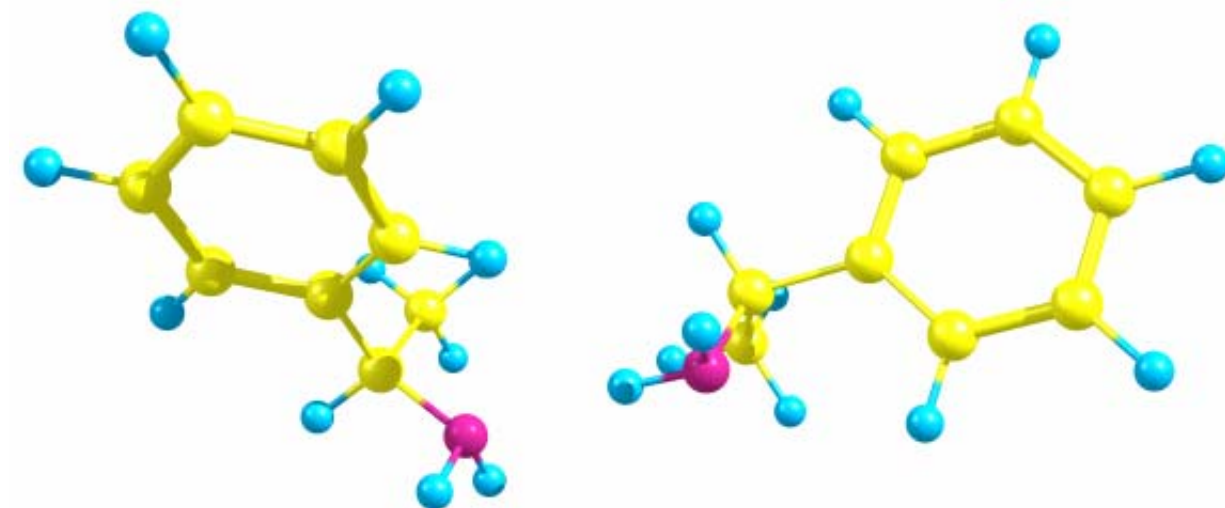


Figure 12. Optimized structure for MBA dimer in methanol. Calculated with PCM B3LYP methodology with cc-pVDZ basis set.

For the completely protonated MBA in methanol, the asymmetric N-H stretch was found to be 3319 and 3313 cm^{-1} (the presence of a third proton gave rise to another possible asymmetric stretch). For the MBA dimer, the calculated asymmetric stretch was at 3425 cm^{-1} . Several conclusions can be reached from the results of these two calculations. First, the MBA dimer calculation shows that even if the amine is not completely hydrogen bonded, the presence of another molecule attracting the lone pair electron density of the nitrogen will lower the effective frequency of the N-H asymmetric stretch. Assuming that the frequency of the asymmetric stretch could be calculated perfectly via Gaussian03, the MBA dimer calculation shows that the species that are surrounding the MBA molecules at infinite dilution are attracting the lone pair electrons more strongly than the MBA molecule does. The results of the MBA^+ in methanol calculations agree fairly well with experiment; again assuming that Gaussian is able to accurately calculate the exact asymmetric vibrational frequency, a majority of the MBA molecules are protonated via an abstraction of a proton from methanol. Complete abstraction as pictured in this calculation is unlikely, but the calculations do confirm that the experimental observations are the results of MBA interacting with methanol, and not other MBA molecules, and that a temporary hydrogen bond is formed between the two species.

The results of the NMR experiments in methanol are similar to those in DMSO in that all of the recorded protons have a larger chemical shift at high solvent concentration than in the neat form. Chemical shifts of the amine protons were difficult to determine exactly because the expected amino proton signal combined with the alcohol proton signal, therefore, the formation of a temporary hydrogen bond between the two species is further confirmed. Similar to what was seen in DMSO, the CH and CH_3 peaks, along with the alcohol methyl group, all have higher chemical shifts at higher methanol concentration, suggesting a shift of electron density to stabilize the hydrogen bonding. The Mulliken charge analysis of the amino protons in methanol confirms that they possess a higher charge than they do in cyclohexane, and therefore appear at a higher chemical shift. Figure 13 shows the optimization of a methanol molecule positioned such

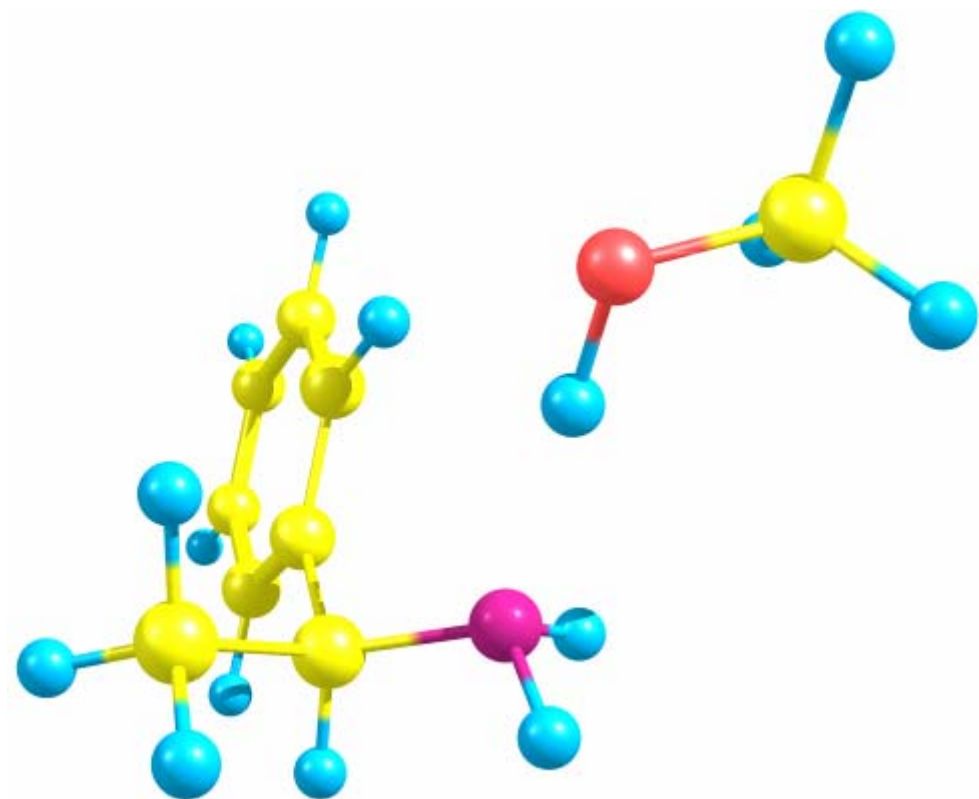


Figure 13. Optimized MBA and methanol in methanol. Calculated with PCM B3LYP functional and aug-cc-pVDZ basis set.

as to allow for amino-hydrogen interaction. These results are from a PCM B3LYP aug-cc-pVDZ calculation. The inclusion of an actual methanol molecule in the optimization of MBA in methanol significantly affects the Mulliken charges on several protons. The amino protons are expected to have a charge 0.10 greater than their charge in cyclohexane, affirming the suspicion that the electron density would move to the nitrogen center to accommodate the positive charge from the hydrogen bond. The Mulliken charges for the methanol included system on the methyl carbons of MBA show a similar partial charge to the cyclohexane system, but the methyl carbon shows an increase in charge, maybe accounting for the slight increase in chemical shift for the methyl protons. Likewise, the proton off of the chiral carbon actually is expected to have a lower partial charge than what is expected referenced to cyclohexane, but the chiral carbon itself has an increased partial charge, thereby possibly giving rise to a similarly small chemical shift for the CH proton.

The observed optical rotation of MBA in methanol at 436 nm shows the greatest deviation from linearity, with the largest effect at $\chi_{\text{MBA}}=0.5$, and the specific rotation at 436 nm shows a similar effect to that observed in DMSO. However, a more pronounced effect is seen in methanol. The extrapolated specific rotation at infinite dilution is -58.75° when using a quadratic fit. The specific rotation at infinite dilution in methanol is the largest rotation for any of the solvents utilized and is explained by the formation of a hydrogen bond between MBA and methanol. A calculation of the optical rotation for the geometry in Figure 13 (MBA with methanol included in the calculation) at the sodium D line gave a rotation of $+38.10^\circ$; the experimental rotation at infinite dilution for 589 nm is -28.10° . The geometry of the MBA in Figure 10 corresponds to (*S*)-MBA, but results for the calculation in the system give a specific rotation that is opposite in sign from the experimentally observed specific rotation at 589 nm. At present it is concluded that the effect of a methanol was overestimated in the calculation.

Similar to the analysis in the previous chapter, a multiple variable regression analysis of the infinite dilution results for the FTIR and NMR experiments should support the experimental observations. The infinite dilution results are presented in Table 4, and the results of the analysis are presented in Table 5. For FTIR experiments, it has been

Table 4. Results of the infinite dilution analysis for FTIR and NMR experiments.

	ν (NH ₂)	δ (ppm) NH ₂	α	β	π^*
Cyclohexane	3583.6	1.545	0.00	0.00	0.00
Toluene	3382.2	0.666	0.00	0.11	0.49
Nitrobenzene	3380.6	2.040	0.00	0.30	0.86
DMSO	3349.2	3.406	0.00	0.76	1.00
Methanol	3345.6	6.390	0.98	0.66	0.60

Table 5. Results of the multiple variable regression analysis for infinite dilution values for FTIR and NMR experiments. C_0 is the inherent spectroscopic value for either FTIR or NMR. The errors for each coefficient are: FTIR – $\alpha \pm 108.25$, $\beta \pm 215.40$, $\pi^* \pm 161.67$, $c_0 \pm 61.70$ NMR: $\alpha \pm 1.23$, $\beta \pm 2.45$, $\pi^* \pm 1.84$, $c_0 \pm 0.70$.

	α	β	π^*	c_0	R value
FTIR analysis	-120.03	117.090	-296.11	3563.62	0.945
NMR analysis	2.93	4.41	-1.18	1.32	0.986

shown that the donation of a hydrogen to the amine, or the α term in Kamlet-Taft parameters, will lower the overall observed frequency for the asymmetric N-H stretch, and the projected model agrees with those observations. From the experimental data, it was not determined what effect the donation of a hydrogen bond from MBA, the β term, would have on the observed N-H frequency, nor were the effects of a polar solvent isolated. Regarding the NMR regression analysis, the effect of the solvent protonating MBA, the α term, is seen to give a higher chemical shift of the amine protons, but the effects of the π cloud on the chemical shift (the results from the toluene experiments) are not necessarily confirmed by this analysis. More solvents would need to be included in this study in order to give more confidence to this method of analysis.

With the results for each solvent having been discussed and explained, a general picture for the effects of various solvents on the spectroscopic properties of MBA can be established. Foremost, the formation of a hydrogen bond or other form of temporary attraction from the lone pair of electrons on the nitrogen to another species is profound; this chemical effect is synonymous to a Lewis base-Lewis acid pseudoreaction. In cyclohexane, toluene, and nitrobenzene, MBA serves as the Lewis base and Lewis acid at modest concentrations of MBA, while in DMSO and methanol, the solvents serve as stronger Lewis acids than the solute MBA. In ORD experiments, the differences between cyclohexane and toluene are slight, and only the presence of the π electron cloud at infinite dilution chemically separate the two solvents. Thus it is concluded that the π electron cloud provides a minor contributor to the optical rotation of MBA. This is not to suggest that the π electron cloud does not affect other spectroscopic observables. The amine protons' chemical shifts change in a manner that is completely opposite to any other utilized solvent, but this effect does not alter the measured specific rotation. The ORD data for nitrobenzene further confirms the secondary nature of the π cloud effects on the optical rotation. Rather, the electron density and charge (if one is present) on the nitrogen appear to be the main factors affecting the optical rotation, as confirmed by the data from DMSO and methanol experiments.

Conclusion

Experiments covering the mole fraction concentration range elucidate hydrogen bonding and other electronic effects of solvation for MBA. The formation of a temporary hydrogen bond with the amine on MBA is shown to lower the frequency of the asymmetric N-H stretch, and dependent upon the solvent, MBA will hydrogen bond to either itself or the solvent, typical of Lewis base-acid behavior. ^1H NMR measurements show that several other protons are affected by the redistribution of electron density in the formation of the hydrogen bond, and the chemical shifts reflect the electron distribution. With regards to the optical rotation, only the chemical nature of the nitrogen appears to affect the magnitude of the optical rotation since neither toluene or nitrobenzene affect the optical rotation significantly differently than cyclohexane. This result indicates that the position and electronic effects of the π cloud do not contribute to the specific rotation of MBA.

Chapter IX.

Conclusions

The experiments presented in this thesis have illuminated specific aspects of molecular chirality. The scope of the studies ranged from inducing chirality in crystalline systems to probing the chiroptical properties of the crystalline systems to investigating the mitigating factors influencing optical rotation in the liquid phase for a neat organic system (and solutions of the same system). All of the experiments provided results that broadened our current understanding of chirality.

The nonphotochemical laser induced nucleation phenomenon (NPLIN) was investigated in an organic system, glycine, and the inorganic system, sodium bromate (NaBrO_3). The results from the glycine system partially confirmed the previously reported NPLIN phenomenon, and a different geometry was investigated by focusing the laser into the supersaturated solution. The results of the differing geometry suggest that NPLIN may still be occurring, but at the present time, no conclusive statements can be made due to the number of macroscopic variables describing a microscopic event. Likewise, the results for the crystallization experiments of NaBrO_3 suggest that NPLIN may occur, but polarization of the incident radiation is not a variable that can affect the chirality of the formed crystal. Interestingly, intense pulsed sound waves produced by focused laser beams into the solution or on metal interface with the solution produced many crystals with microscopic sizes that were of good quality almost instantaneously. This particular observation may be of utility in various crystallization applications.

The optical rotatory dispersion, ORD, curve was measured for sodium chlorate, NaClO_3 , and sodium bromate, NaBrO_3 , and the results agree with previous measurements. Higher laser intensity produces non-linear effects (NL-ORD) contributing to the optical rotation. The results indicate that a dominant contribution to the optical rotation is from ν_1 , but at higher intensities, $2\nu_1$ (or $n\nu_1$) can contribute to the

optical rotation. Previous theoretical consideration of NL-ORD does provide confirmation of experimental results.

The speed of sound in racemic and enantiomerically pure α -methylbenzylamine (MBA) was measured with a modified laser generated sound wave approach. The compressibility of the enantiomerically pure MBA is slightly higher than the racemic system. The magnitude of the compressibility was confirmed with measurements of the low frequency intermolecular vibrations via Raman spectroscopy measurements. The effective interaction radii for the two systems were found to differ by $\sim 0.02 \text{ \AA}$, with the racemic MBA having a slightly larger effective interaction radius; which agrees in principle with the results of Zingg et al.⁹⁸

A qualitative study of the optical rotation of (*S*)-MBA in various solvents showed that calculations using the polarizable continuum model (PCM) were incomplete in describing the solvent effects on the optical rotation. An analysis of the optical rotations with the Kamlet-Taft solvent parameters (α , β , and π^*) gave a better description with the predicted model as evidenced by their agreement with experimental observations. Likewise, solvents with no dipole moment and high quadrupole moments (or higher order) were seen to give larger than expected solvent effects, which is in accord with previous results from Wiberg et al.¹⁶¹

Studying the spectroscopic behavior of MBA with FTIR and NMR through the entire mole fraction concentration range in five distinct solvents provided useful information that could be applied to interpreting the factors important in determining the optical rotation. Results indicated that only changing the amine site on MBA significantly affected the optical rotation, and that the orientation of the benzene chromophore and effects from a π cloud were not significant effects. FTIR experiments show that MBA self-associates until a low concentration ($\sim \chi_{\text{MBA}}=0.1$ in cyclohexane). NMR experiments show that many protons (CH and CH₃ for example) are affected differently dependent upon the solvent, but those effects do not translate over to affecting the ORD of MBA.

In conclusion, chiral systems have been studied in the crystalline and liquid phases. Chirality is a phenomenon that is not completely understood, but the present studies have added to the current body of knowledge with specific emphasis on sodium chlorate and sodium bromate crystalline state and α -methylbenzylamine in solution. Further, optical spectroscopy and other methodologies have been successfully utilized in studying chirality. NPLIN was confirmed in several systems. In addition, it was found that sound pulses can induce crystal growth. Non-linear optical rotatory dispersion was demonstrated in sodium chlorate and sodium bromate crystals. Chiral discrimination was observed in racemic and enantiomeric α -methylbenzylamine, and the underlying contributor to the optical rotation of MBA was isolated. The present studies have added significant contributions to the ongoing study of chirality.

References

1. Mason, S. F. *Ann. Rep. Prog. Chem. Section A* **1976**, 73, 53
2. Newcomb, M.; Helgeson, R. C.; Cram, D. J. *J. Am. Chem. Soc.* **1974**, 96, 7367
3. Fischer, E. *Chem. Ber.* **1899**, 32, 3617
4. Young, S. *J. Am. Chem. Soc.* **1911**, 33, 148
5. Berkeley, E. *Phil. Mag.* **1912**, 24, 254
6. Khamskii, E. *Crystallization from Solutions*, Consultants Bureau: New York, 1969
7. Christian, J. The Theory of Transformations in Metals and Alloys. Pergamon Press: Oxford, 1965
8. Kelton, K. Solid State Physics Vol. 45. Eds. Ehrenreich, H.; Turnbull, D. Academic Press: New York, 1991
9. Hoare, M.; McInnes, J. *Discussions of the Faraday Society* **1976**, 61, 24
10. Gibbs, J. Collected Works, Vol. 1, Thermodynamics. Yale University Press: New Haven, 1948
11. Volmer, M. Kinetic der Phasenbildung. Steinkopff: Leipzig, 1939
12. Becker, R.; Doring, W. *Annalen der Physik* **1935**, 24, 719
13. Nielsen, A. Kinetics of Precipitation. Pergamon: Oxford, 1964
14. Strickland-Constable, R. Kinetics and Mechanism of Crystallization. Academic Press: New York, 1968
15. Sohnle, O.; Garside, J. Precipitation: Basic Principles and Industrial Applications. Butterworth-Heinemann: Oxford, 1992
16. Kaschiev, D. Nucleation. Butterworth-Heinemann: Oxford, 2000
17. Mullin, J. W. Crystallization Fourth Edition. Butterworth Heinemann: Oxford, 2001
18. Botsaris, G.; Denk, E.; Ersan, G. *Ind. Eng. Chem.* **1969**, 61, 86
19. Qian, R.; Botsaris, G. *Chem. Eng. Sci.* **1997**, 52, 3429
20. Botsaris, G.; Denk, E. *Annu. Rev. Ind. Eng. Chem.* **1972**, 1970, 493
21. Randolph, A.; Larson, M. Theory of Particulate Processes. Academic Press: New York, 1971
22. Qian, R.; Botsaris, D. *Chem. Eng. Sci.* **1998**, 53, 1745
23. Denk, E.; Botsaris, G. *J. Crystal Growth* **1972**, 13/14, 493

24. Yokota, M.; Oguchi, T.; Arai, K.; Toyokura, K. Inoue, C.; Naijyo, H. *Crystallization as a Separations Process (ACS Symposium No. 438)*, Eds. A. Myerson and K. Toyokura , 1992, 271
25. Davey, R.; Black, S.; William, L.; McEwan, D.; Sadler, D. *J. Crystal Growth* **1990**, *102*, 97
26. Kondepudi, D.; Kaufmann, R.; Singh, N. *Science* **1990**, *250*, 975
27. Saratovkin, D. Dendritic Crystallization. Consultants Bureau: New York, 1959
28. Ostwald, W. Lehrbuch der Allgemeinen Chemie. Englemann: Leipzig, 1896
29. Ostwald, W. *Zeitschrift fur Physikalische Chemie* **1897**, *22* 289
30. Dufor, L.; Defay, R. Thermodynamics of Clouds. Academic Press: New York, 1963
31. Cardew, P.; Davey, R. *Symposium on the Tailoring of Crystal Growth*, Institution of Chemical Engineers, London, 1.1-1.9, 1982
32. Albrecht, G.; Corey, R. B. *J. Am. Chem. Soc.* **1939**, *61*, 1087
33. Iitaka, Y. *Acta Cryst.* **1958**, *11*, 225
34. Iitaka, Y. *Acta Cryst.* **1961**, *14*, 1
35. Bhat, M. N.; Dharmaparakash, S. M. *J. Cryst. Growth* **2002**, *236*, 376
36. Yu, L.; Ng, K. *J. Pharm. Sciences* **2002**, *91*, 2367
37. Gidalevitz, D.; Feidenhans'l, R.; Matlis, S.; Smilgies, D.; Christensen, M. J.; Leiserowitz, L. *Angew Chem. Int.* **1997**, *36*, 955
38. Potrzebowksi, M. J.; Tekely, P.; Dusausoy, Y. *Sol. State Nuc. Mag. Res.* **1998**, *11*, 253
39. Krishnan, R. S.; Balasubramanian, K. *Proc. Ind. Acad. Sci. A* **1958**, *48A*, 55
40. Balasubramanian, K.; Krishnan, R. S.; Iitaka, Y. *Bul. Chem. Soc. Japan* **1962**, *35*, 1303
41. Garetz, B. A.; Aber, J.; Goddard, N. L.; Young, R. G.; Myerson, A. S. *Phys. Rev. Letters* **1996**, *77*, 3475
42. Reintjes, J. F. Nonlinear Optical Parametric Process in Liquids and Gases. Springer, Berlin 1991
43. Zaccaro, J.; Matic, J.; Myserson, A.; Garetz, B. *Cryst. Grwth. & Design* **2001**, *1*, 5
44. Myerson, A. S.; Lo, P. Y. *J. Cryst. Growth* **1990**, *99*, 1048

45. Garetz, B. A.; Matic, J.; Myerson, A. *Phys. Rev. Lett.* **2002**, 89, 175501-1
46. Chen, C.; McCann, M. *Chem. Phys. Lett.* **1988**, 143, 338
47. Sun, X.; Garetz, B. *Crst. Grwth. & Design* **2006**, 0, 1
48. Beurskens-Kerssen, G.; Kroon, J.; Endeman, H. J.; Van Laar, J.; Bijovoet, J. M. Crystallography and Crystal Perfection. Ramachandran, G. N. Ed., Academic Press: London, 1963, 225-236
49. Abrahams, S.; Bernstein, J. *Acta Cryst.* **1977**, B33, 3601
50. Drude, P. Theory of Optics. Longmans: London, 1902
51. Oseen, C. *Ann. Phys. (Leipzig)* **1915**, 48, 1
52. Born, M. *Z. Phys.* **1922**, 8, 390
53. Kuhn, W. *Z. Phys. Chem. (Leipzig)* **1929**, B4, 14
54. Gray, F. *Phys. Rev.* **1916**, 7, 472
55. Kirkwood, J. *J. Chem. Phys.* **1937**, 5, 479
56. Ramachandran, G. *Proc. Indian Acad. Sci.* **1951**, 33, 217
57. Ramachandran, G. *Proc. Indian Acad. Sci.* **1951**, 33, 309
58. Ramachandran, G. *Proc. Indian Acad. Sci.* **1951**, 34, 127
59. Chandrasekhar, S.; Madhava, M. *Acta Cryst.* **1967**, 23, 911
60. Madhava, M. *Proc. Indian Acad. Sci.* **1973**, 72, 67
61. Fisher, V. Investigations of Supersaturated Salt Solutions. Pergamon Press: Riga, 1913
62. Noboru, F. *J. Sci. Hiroshima Univ.* **1961**, A2, 25
63. Kasatkin, A. *Sov. Phys. Crystl.* **1966**, 11, 295
64. Kipping, F.; Pope, W. *J. Chem. Soc.* **1898**, 12, 606
65. Kondepudi, D.; Bullock, K.; Digits, J.; Hall, J.; Miller, J. *J. Am. Chem. Soc.* 1993, 115, 10211
66. Szurgot, M.; Szurgot, J. *Cryst. Res. Technol.* **1995**, 30, 949
67. Viedma, C. *J. Cryst. Growth* **2004**, 261, 118
68. Kauzmann, W. J.; Walter, J. E.; Eyring, H. *Chem. Rev.* **1940**, 26, 339
69. Rosenfeld, V. L. *Z. Physik.* **1928**, 52, 161
70. Condon, E. V. *Rev. Modern Phys.* **1937**, 9, 432

71. Born, M. *Ann. Physik.* **1918**, 55, 177
72. Lowry, T. M.; Allsopp, C. B. *Proc. Roy. Soc. (London)* **1934**, 146, 313
73. Condon, E. V.; Altar, W.; Eyring, H. *J. Chem. Phys.* **1937**, 5, 753
74. Andrews, D. L. *Chem. Physics* **1976**, 16, 419
75. Power, E. A. *J. Chem. Phys.* **1975**, 63, 1348
76. Tinoco Jr., I. *J. Chem. Phys.* **1975**, 62, 1006
77. Evans, M. W. *J. Mod. Optics* **1990**, 37, 1655
78. Peticolas, W. L. *Ann. Rev. Phys. Chem.* **1967**, 18, 233
79. Gedanken, A.; Tamir, M. *Rev. Sci. Instruments* **1987**, 58, 950
80. Cameron, R.; Tabisz, G. C. *Mol. Physics* **1997**, 90, 159
81. Nishimura, T.; Shimizu, B.; Iwai, I. *Biochimica et Biophysica Acta, Nucleic Acids and Protein Synthesis* **1968**, 157, 221
82. Einhorn, A. J.; Pao, Y. H.; Phelps, F. W. *Spec. Letters* **1980**, 13, 227
83. Kizel, V. A.; Krasilov, Y. I.; Shamraev, V. N. *Optics and Spectrosc.* **1964**, 17, 470
84. Papadakis, E. P. *J. Acoust. Soc. Am.* **1967**, 42, 1045
85. Papadakis, E. P. *Rev. Sci. Instrum.* **1976**, 47, 806.
86. Tardajos, G.; Pena, M. D.; Aicart, E. *J. Chem. Thermodynamics* **1986**, 18, 683
87. Povey, M.; Hindle, S.; Kennedy, J.; Stec, Z.; Taylor, R. *Phys. Chem. Chem. Phys.* **2003**, 5, 73
88. Schaafs, W. Landolt-Bornstein New Series 2, ed. Hellwege, K. –H. and Hellwege, A. M. Springer-Verlag, New York, 1967, 79
89. Zak, A.; Dzida, M.; Zorebski, M.; Ernst, S. *Rev. Sci. Instrum.* **2000**, 71, 1756
90. Perova, Tatiana S. *Advances in Chemical Physics* **1994**, 87, 427-82
91. Gorodyskii, V.; Kardashina, L.; Bakhshiev, N. *Zh. Fiz. Khim.* **1975**, 49, 1089
92. Lepori, L.; Mengheri, M.; Mollica, V. *J. Phys. Chem.* **1983**, 87, 3520
93. Atik, Z.; Ewing, M.; McGlashan, M. *J. Chem. Thermodynamics* **1983**, 15, 159
94. Atik, Z.; Saito, Y.; Kusano, K. *J. Chem. Thermodynamics* **1987**, 19, 99
95. Craig, D.; Mellor, D. *Top. Curr. Chem.* **1976**, 63, 1
96. Atik, Z.; Ewing, M.; McGlashan, M. *J. Phys. Chem.* **1981**, 85, 3300
97. Jorgensen, W.; Bigot, B. *J. Phys. Chem.* **1982**, 86, 2867

98. Zingg, S.; Arnett, E.; McPhail, A.; Bothner-By, A.; Gilkerson, W. *J. Am. Chem. Soc.* **1988**, *110*, 1565
99. Kasoev, S.; Lyamshev, L. *Sov. Phys. Acoust.* **1977**, *23*, 510
100. Egerev, S.; Esipov, I.; Lyamshev, L.; Naugol'nykh, K. *Sov. Phys. Acoust.* **1979**, *25*, 119
101. Fischer, Andrew T.; Compton, Robert N. *Rev. Sci. Instr.* **2003**, *74*, 3730
102. Bakhshiev, N. G. Spectroscopy of Intermolecular Interactions. 1972,
103. Kostov, I. *Crystallography Izd. Mir* **1965**, Moscow
104. Rodnikova, M. N.; Val'kovskaya, T. M.; Kartez, V. N.; Kayumova, D. B. *Journal of Molecular Liquids* **2003**, *106*, 219
105. Kartsev, V. N.; Rodnikova, M. N.; Tsepulin, V. V.; Dudnikova, K. T.; Markova, V. G. *Zhurnal Strukturnoi Khimii* **1986**, *27*, 187
106. Rodnikova, M. N. *Zhurnal Fizicheskoi Khimii* **1993**, *67*, 275
107. Munoz, Maria A.; Sama, Octavio; Galan, Manuel; Guardado, Pilar; Carmona, Carmen; Balon, Manuel. *Journal of Physical Chemistry B* **1999**, *103*, 8794
108. Palit, S. R.; Mukherjee, S.; De, Sadhan K. *Journal of Physical Chemistry* **1971**, *75*, 2404
109. Nikolic, Aleksandar D.; Kobilarov, Nestor L.; Brzic, Aleksandar N. *Journal of Molecular Structure* **1983**, *99*, 179
110. Balon M; Guardado P; Munoz M A; Carmona C *Biospectroscopy* **1998**, *4*, 185
111. Stefov, Viktor; Pejov, Ljupco; Soptrajanov, Bojan. *Journal of Molecular Structure* **2003**, *649*, 231
112. Nikolic, A.; Petrovic, S.; Antonovic, D.; Gobor, L. *Journal of Molecular Structure* **1997**, *408*, 355
113. Coetzee, J. F. Solute-Solvent Interactions. Coetzee, J. F., Ritchie, C. D., Ed.; M. Dekker: New York, 1969
114. Foreman, M. I. *Nuclear Magnetic Resonance* **1976**, *5*, 292
115. Jameson, Cynthia J. *Bulletin of Magnetic Resonance* **1980**, *3*, 3
116. Santo, M.; Cattana, R.; Silber, J. J. *Spectrochimica Acta, Part A: Molecular and Biomolecular Spectroscopy* **2001**, *57A*, 1541

117. Buckingham, A. D. *Transactions of the Faraday Society* **1960**, 56, 753
118. Lappi, Simon E.; Franzen, Stefan. *Spectrochimica Acta, Part A: Molecular and Biomolecular Spectroscopy* **2004**, 60A(1-2), 357
119. Coulombeau, Christian; Rassat, Andre. *Bulletin de la Societe Chimique de France* **1963**, 11, 2673
120. Gekko, Kunihiro. *Agricultural and Biological Chemistry* **1980**, 44, 1183
121. Chen, Y.; Wallace, B. A. *Biophysical Chemistry* **1997**, 65, 65
122. Mukhedkar, A. J. *Journal of Chemical Physics* **1961**, 35, 2133
123. Kumata, Yoshiyuki; Furukawa, Junji; Fueno, Takayuki. *Bulletin of the Chemical Society of Japan* **1970**, 43, 3920
124. Green, J. P.; Johnson, C. L.; Kang, S. *Annu. Rev. Pharmacol.* **1974**, 14, 319
125. Kumbar, M. *Journal of Medicinal Chemistry* **1976**, 19, 1232
126. Gottarelli, G.; Samori, S. *J. Chem. Soc. B* **1971**, 12, 2418
127. Bosnich, B.; Moskovits, M.; Ozin, G. A. *J. Am. Chem. Soc.* **1972**, 94, 4750
128. Smith, H.; Neergaard, J.; Paulis, T.; Chen, F. *J. Am. Chem. Soc.* **1983**, 105, 1578
129. Johnson, W. C.; Fontana, L.; Smith, H. *J. Am. Chem. Soc.* **1987**, 109, 3361
130. Macleod, N.; Butz, P.; Simons, J.; Grant, G.; Baker, C.; Tanter, G. *Phys. Chem. Chem. Phys.* **2005**, 7, 1432
131. Young, L.; Porter, C. *J. Am. Chem. Soc.* **1937**, 59, 1437
132. Lyle, Gloria G. *Journal of Organic Chemistry* **1960**, 25, 1779
133. Brewster, James H.; Buta, George J. *J. Am. Chem. Soc.* **1966**, 88, 2233
134. Cymerman Craig, John; Chan, Rosalind P. K.; Roy, Sushil Kumar. *Tetrahedron* **1967**, 23, 3573
135. Smith, Howard E.; Warren, Mitchum E., Jr.; Katzin, Leonard I. *Tetrahedron* **1968**, 24, 1327
136. Angeloni, Annino S.; Cagna, Domenico; Gottarelli, Giovanni. *Ricerca Scientifica* **1969**, 39, 35
137. Smith, Howard E.; Willis, T. C. *J. Am. Chem. Soc.* **1971**, 93, 2282
138. Polavarapu, P. *Chirality* **2002**, 14, 768
139. Kamlet, M. J.; Taft, R. W. *J. Am. Chem. Soc.* **1977**, 99, 6027

140. Gutmann, V. *The Donor-Acceptor Approach to Molecular Interactions*; Plenum Press: New York, 1978
141. Dimroth, K.; Reichardt, C.; Siepmann, T.; Bohlmann, F. *Liebigs Ann. Chem.* **1963**, *1*, 661
142. Kamlet, M. J.; Taft, R. W. *J. Am. Chem. Soc.* **1976**, *98*, 377
143. Kamlet, M. J.; Jones, M. e.; Taft, R. W.; Abboud, J. –L. M. *J. Chem. Soc., Perkin Trans. 2* **1979**, *3*, 342
144. Kamlet, M. J.; Taft, R. W. *J. Chem. Soc., Perkin Trans. 2* **1979**, *3*, 337
145. Born, M. *Z. Phys.* **1920**, *1*, 45
146. Kirkwood, J. G. *J. Chem. Phys.* **1934**, *2*, 351
147. Onsager, L. *J. Am. Chem. Soc.* **1936**, *58*, 1486
148. Rivail, J-L., Rinaldi, D. *Chem. Phys.* **1976**, *18*, 233
149. Langlet, J., Claverie, P., Caillet, J., Pullman, A. *J. Phys. Chem.* **1988**, *92*, 1617
150. Miertus, S., Scrocco, E., Tomasi, J. *Chem. Phys.* **1981**, *55*, 117
151. Tomasi, J. *Theor. Chem. Acc.* **2004**, *112*, 184
152. Mennucci, B., Tomasi, J., Cammi, R., Cheeseman, J., Frisch, M., Devlin, F., Gabriel, S., Stephens, P. *J. Phys. Chem. A* **2002**, *106*, 6102
153. Stephens, P., Devlin, F., Cheeseman, J., Frisch, M., Mennucci, B., Tomasi, J., *Tetrahedron: Asymmetry* **2000**, *11*, 2443
154. Stephens, P., Devlin, F., Cheeseman, J., Frisch, M. *J. Phys. Chem. A* **2001**, *105*, 5356
155. Landolt, H. The Optical Rotating Power of Organic Substances and its Applications. Chemical Publishing Co.: Easton, PA, 1902
156. Eliel, E.; Wilen, S.; Doyle, M. Basic Organic Stereochemistry. Wilery-Interscience: New York, 2001
157. Gaussian 03, Revision **C.02**, M. J. Frisch, G. W. Trucks, H. B. Schlegel, G. E. Scuseria, M. A. Robb, J. R. Cheeseman, J. A. Montgomery, Jr., T. Vreven, K. N. Kudin, J. C. Burant, J. M. Millam, S. S. Iyengar, J. Tomasi, V. Barone, B. Mennucci, M. Cossi, G. Scalmani, N. Rega, G. A. Petersson, H. Nakatsuji, M. Hada, M. Ehara, K. Toyota, R. Fukuda, J. Hasegawa, M. Ishida, T. Nakajima, Y. Honda, O. Kitao, H. Nakai, M. Klene,

- X. Li, J. E. Knox, H. P. Hratchian, J. B. Cross, V. Bakken, C. Adamo, J. Jaramillo, R. Gomperts, R. E. Stratmann, O. Yazyev, A. J. Austin, R. Cammi, C. Pomelli, J. W. Ochterski, P. Y. Ayala, K. Morokuma, G. A. Voth, P. Salvador, J. J. Dannenberg, V. G. Zakrzewski, S. Dapprich, A. D. Daniels, M. C. Strain, O. Farkas, D. K. Malick, A. D. Rabuck, K. Raghavachari, J. B. Foresman, J. V. Ortiz, Q. Cui, A. G. Baboul, S. Clifford, J. Cioslowski, B. B. Stefanov, G. Liu, A. Liashenko, P. Piskorz, I. Komaromi, R. L. Martin, D. J. Fox, T. Keith, M. A. Al-Laham, C. Y. Peng, A. Nanayakkara, M. Challacombe, P. M. W. Gill, B. Johnson, W. Chen, M. W. Wong, C. Gonzalez, and J. A. Pople, Gaussian, Inc., Wallingford CT, 2004.
158. Marcus, Y. Properties of Solvents. Wiley: Chichester, New York, 1998
159. Atkins, P. W. Physical Chemistry. W. H. Freeman and Company: San Francisco, California, 1978
160. Rule, G., McLean, A. *Journal of the Chemical Society, Abstracts* **1931**, 674
161. Wiberg, K., Wang, Y., Wilson, M., Vaccaro, P., Cheeseman, J. *J. Phys. Chem. A* **2005**, *109*, 3448
162. Bauer, E.; Magat, M. *J. Phys. Radium* **1938**, *9*, 319
163. Heald, C.; Thompson, H. W. *Proc. Roy. Soc. A* **1962**, *268*, 89
164. Werner, R. L.; Quinn, J.; Haken, J. *Spectrochimica Acta* **1982**, *38A*, 887
165. Kagiya, T.; Suida, Y.; Inoue, T. *Bull. Chem. Soc. Jap.* **1968**, *41*, 767
166. Bellamy, L. J.; Rogasch, P. E. *Spectrochimica Acta* **1960**, *16*, 30
167. Gamer, G.; Wolff, H. *J. Phys. Chem.* **1972**, *76*, 871
168. Ishimoto, B.; Tonan, K.; Ikawa, S. *Spectrochimica Acta* **1999**, *55A*, 2321
169. Li, Q.; Wu, G.; Yu, Z. *J. Am. Chem. Soc.* **2006**, *128*, 1438
170. Yamaguchi, I. *Kogyo Kagaku Zasshi* **1965**, *68*, 1328
171. Bishop, E. O. *Ann. Rep. Progr. Chem.* **1962**, *58*, 71
172. Davis, J. C.; Deb, K. K. Advances in Magnetic Resonance Equilibria. Waugh, J. S. Ed. Academic Press, New York (1970)
173. Lippert, E. *Ber. Bunsenges. Phys. Chem.* **1963**, *67*, 267
174. LaPlanche, L.; Thompson, H.; Rogers, M. *J. Phys. Chem.* **1965**, *9*, 1482
175. Graham, L.; Chang, C. *J. Phys. Chem.* **1971**, *75*, 776

176. Graham, L.; Chang, C. *J. Phys. Chem.* **1971**, 75, 784
177. Johnston, M.; Gasparro, F.; Kuntz Jr., I. *J. Am. Chem. Soc.* **1969**, 19, 5715

Vita

Andrew Thomas Fischer was born in Knoxville, Tennessee on March 19, 1980. He attended public schooling before graduating from Karns High School in May 1998. He enrolled in the University of Tennessee at Knoxville in August 1998 and received his Bachelor of Science degree in Chemistry in May 2002. After receiving his Bachelor degree, he entered into graduate school at the University of Tennessee at Knoxville, where his advising professor was Dr. Robert Compton in the Chemical Physics program.